NTNU – Trondheim
Norwegian University of
Science and Technology

A Numerical Study of Transient Friction and Transient Friction Modelling in Ramp-up and Ramp-down Flow Conditions Similar to Pump Ramp-up and Valve Closure in Gas Transport Pipelines

Sigmund Andreas Birkeland

Physics
Submission date: October 2014
Supervisor: Alex Hansen, IFY
Co-supervisor: Tor Ytrehus, EPT

Norwegian University of Science and Technology
Department of Physics

A Numerical Study of Transient Friction and Transient Friction Modelling in Ramp-up and Ramp-down Flow Conditions Similar to Pump Ramp-up and Valve Closure in Gas Transport Pipelines

Sigmund A. Birkeland.

Problem Description

Background and Objective

In transport of natural gas through long export lines, typically 400-600km on the bed of the North Sea, it is of utmost importance to have accurate computational models to predict the hydraulic capacity of the line, both under steady state and at transient flow conditions. Due to the extreme length of the pipe lines, only one-dimensional models are applicable, and these require inputs like friction factor and heat transfer coefficients. Such parameters are usually results of steady state correlations, and there are doubts about their validity under transient flow conditions. The objective of this work is to compare results from 1D-computations and friction factor with detailed 2D-numerical solutions for transient periods in short pipes such that conventional CFD-simulations are feasible.

Following tasks are to be considered:

1. To find out about the current status in theoretical and computational gas transport, with special focus on transient flow conditions.
2. To set up a computational case for turbulent pipe flow at high Reynolds number, and to use a commercial CFD-solver with turbulence models included to predict mean flow characteristics transient cases.
3. To pay special attention to treatment of boundary conditions for velocity and turbulence properties, and to have a fine resolution of the fields close to the solid walls; also in cases of finite roughness of the surface.
4. To extract friction factor and pressure drop from the computed results and compare with standard results from 1D-analysis.

Preface

This thesis is the result of the work done during the last year of the Master of Physics programme at NTNU. The thesis was done at the department of energy- and process engineering.

In gas transport models it is common to use a stationarily developed friction factor. The purpose of this thesis was to investigate the importance that transient dynamics have on the friction factor as opposed to a stationary friction factor.

This task has been undertaken earlier by Torbjørn Lyssand in his Master Thesis of 2011[16]. Here few comparative results were achieved due to large uncertainties in the 2D model.

The task of simulating flow with the CFD packet Fluent has been a difficult journey, The ANSYS Academic centre was undergoing upgrading at the time, and the beginner tutorials that I found were rarely relevant and often included difficult geometries. Salvation came with the help of SINTEF employee Christian Etienne who pointed me to the Cornell University FLUENT learning module, which had tutorials on pipe-flow, turbulence and periodically boundary conditions.

Abstract

When gas is transported in long pipelines, computational models are used as tools to plan and to optimize hydraulic capacities. Because of the length of the pipelines the models are mostly one-dimensional (1D) which in turn requires input parameters like a friction factor and heat transfer coefficients. These parameters are usually the result of steady state correlations. There are doubts about the validity of using steady state correlation in transient periods.

The objective of this thesis was to simulate transient periods with an one-dimensional (1D) model and a more detailed two-dimensional (2D) model from a commercial CFD package, extracting the friction factor and then comparing the resulting friction factors from the two models.

The RANS k-ω model was chosen from a set of criteria. To limit the computational demand, periodic boundary conditions were used at the inlet and the outlet of the pipe-segment and the flow was simplified to be isothermal, incompressible, and with constant viscosity. Furthermore, an 1D model was derived and three different friction models were implemented, namely the quasi-steady friction model, the Instantaneous Acceleration Based (IAB) Daily et al. model, and the Vardy et al. friction model. Transient periods, defined as ramp-up and ramp-down flows, were simulated by the models. Ramp-up and ramp-down transients are seen as a sudden increase or decrease in pressure difference, resembling a valve opening or closing. The pressure difference, bulk velocity, and wall shear stress was extracted from the 1D and 2D simulations. In addition, velocity profiles and turbulence profiles were extracted from the 2D simulations.

There were significantly larger differences between quasi-steady friction factor and transient friction factor in ramp-up flows than in ramp-down flow. In ramp-up simulations the transient friction went from overshooting the steady friction factor by 152% to undershooting it by 55%; all within the first 1/10 of the transient. In the corresponding ramp-down simulation the maximum difference was only 1.45%. However, the error between the 1D velocity and the 2D bulk velocity in the ramp-up cases was below the 2D model's velocity uncertainty. Moreover, the opposite was seen in the ramp-down cases, where the error between the 1D and 2D velocity was upwards of 20%

In the ramp-up cases four turning points of the transient component of the wall shear stress were identified, and of those, two were directly coupled to the turbulence diffusion time and the turbulence production delay.

From the results it was found that the use of quasi-steady friction modelling in transient models gave a fairly good approximation of the wall shear stress in decelerating transients; however, the predicted velocity significantly undershot the 2D velocity. In the ramp up simulations the 1D models did not capture the highly varying 2D wall shear stress at the initial stage of the transients, but the 1D models predicted the velocity with reasonable accuracy. Neither of the implemented 1D

transient friction models yielded satisfactory wall shear stress prediction. Overall, the results suggest that better friction models are needed, and that such models can significantly improve the accuracy of transient gas transport models.

Sammendrag

Modeller brukt til å planlegge og optimalisere gasstransport er oftest endimensjonale (1D) og trenger derfor koeffisienter som friksjonsfaktor og varmeoverføringskoeffisient. Disse koeffisientene er ofte basert på stasjonære relasjoner, og det er derfor tvil om deres validitet under transiente perioder.

Målet med denne oppgaven var å simulere transienter med en endimensjonal modell og med en mer detaljert todimensjonal (2D) modell fra en kommersiell CFD pakke. Hvor friksjonsfaktoren og trykkgradienten ekstraheres fra simuleringene, og resultatene fra modellene sammenlignes med hverandre.

En passende todimensjonal turbulent modell fra CFD-pakken ANSYS Fluent ble valgt fra et sett av krav. Valget falt på RANS k-ω modellen. For å begrense kompleksiteten av modelleringen, ble røret modellert med periodiske grensebetingelser, samt at strømningen ble forenklet til å være inkompressibel, isotermisk og med konstant viskositet. Den endimensjonale modellen, hvor tre friksjonsmodeller ble implementert, ble så utviklet. Disse tre friksjonsmodellene er (1) en kvasistasjonær, (2) en øyeblikkelig akselerasjonsbasert modell og (3) en friksjonsmodell som tar hensyn til hastighetshistorien i transienten. Transiente perioder, som er definert som såkalte "opprampinger" og "nedrampinger", ble så simulert med modellene; hvor oppramping og nedramping er en plutselig økning eller senkning av trykkgradienten fra en konstant verdi til en annen. Trykkgradienten, tverrsnittgjennomsnittshastigheten (bulkhastigheten) og veggskjærspenningen ble så ekstrahert fra simuleringene, samt hastighets- og turbulens-profiler fra de todimensjonale simuleringene.

Det ble observert signifikante større forskjeller mellom den kvasistasjonære friksjonsfaktoren og den transiente friksjonsfaktoren i opprampingssimuleringer enn i tilsvarende nedrampingssimuleringer med reverserte Reynolds tall. I opprampingssimuleringer varierte avviket mellom kvasistasjonær og transient friksjon fra 152% til -55% innen den første 1/10 av den transiente perioden. I lignende nedrampingssimulering var maksimum avvik på 1.45%. Likevel var avviket mellom den endimensjonal og den todimensjonale bulkhastigheten i opprampingstransientene på under den todimensjonale modellens usikkerhet i tverrsnitthastighet. Det motsatte ble observert i nedrampingstransientene, hvor relativt liten forskjell i veggskjærspenning skapte stor differanse i hastighetsavviket, opp til 20%, mellom de endimensjonale modellene og den todimensjonale modellen.

Det ble observert fire vendepunkter i utviklingen av den ustasjonære komponenten av veggskjærspenningen i opprampingssimuleringene, hvorav to kan beregnes av den turbulente diffusive tiden og den turbulente produksjonsforsinkelsen.

Ut ifra resultatene, ble det funnet at bruken av kvasistasjonær friksjonsmodellering i transiente modeller ga en forholdsvis bra tilnærming til veggskjærspenningen i deselererende transienter, men den resulterende hastighetsprediksjonen bommet grovt midtveis i transientene. I opprampingssimuleringene modellerte de endimensjonale friksjonsmodellene veggskjærspenningen utilfredsstillende, men hastighet-

sprediksjonen stemte godt overens med de todimensjonale resultatene. Ingen av de implementerte endimensjonale friksjonsmodellene ga en spesielt nøyaktig modellering veggsskjærspenningen. Resultatetene indikerer derfor at bedre transiente friksjonsmodeller behøves og at de kan signifikant øke presisjonen til endimensjonale transiente gasstransportmodeller.

Contents

List of Figures

List of Tables

Nomenclature

δ_{ij}	Kronecker delta
$\epsilon = k/D$	relative roughness height
μ	dynamic viscosity
$\mu\phi$	dissipation function
$\nu = \frac{\mu}{\rho}$	kinematic viscosity
ψ	Non-dimensional time defined in equation (2.52)
ρ	density
σ_{ij}	stress tensor
τ_w	wall shear stress
τ_{ws}	steady wall shear stress
τ_{wu}	unsteady component of wall shear stress
$\theta = T - t$	Backwards measuring time
A	cross section area
C_f	Fanning friction factor
D	pipe diameter
E	total energy
e	internal energy
f	Darcy friction factor
h	enthalpy

k roughness height

k^+ dimensionless roughness coefficient

k_1 Unsteady friction coefficient

k_3 Brunone unsteady friction coefficient

p pressure

Q heat

R pipe radius

R specific gas constant

$Re_D = \frac{\rho U D}{\mu}$ Reynolds number

T Time since flow was stationary

T temperature

$t^* = \frac{tU}{D}$ Dimensionless time

T_d Turbulence diffusion time, defined in equation (7.3).

U Cross sectional average velocity in a pipe.

$u^+ = \frac{\overline{u}}{u_\tau}$ dimensionless velocity

$u_\tau = \sqrt{\frac{\tau_w}{\rho}}$ friction velocity

u_i component velocity u, v, and w

W work

$y^+ = \frac{\rho u_\tau y}{\mu}$ dimensionless length scale

1D One-dimensional

2D Two-dimensional

CFD Computational Fluid Dynamics

DNS Direct numerical simulation

LNG Liquid natural gas

Chapter 1

Introduction

Natural gas is an important energy source supplying over 20% of the world's energy consumption in 2010. Furthermore, the production has grown with over 35% from 2000 to 2011, and in Norway it has more than doubled in the same time period[7]. Prognoses for Norwegian production indicate further increases in the years to come as oil production is anticipated to fall[22].

In Norway the produced gas is transported through pipes from offshore fields to processing refineries on land. In the refineries the gas is separated into natural gas and liquefied natural gas (LNG). LNG production makes up for less than 5% of the total Norwegian gas production and is mainly transported with ships to its destination, which is usually Europe and North America. The total Norwegian natural gas production in 2012 was 114.9 billion cubic meters, and of this 92.8% was exported through pipes to the UK and the continental Europe[7].

With increasing production and exportation of natural gas, exploiting the full potential of the existing pipelines is important. To optimize gas transport planning and to maintain correct deliveries to customers, one relies upon good computational models. These models are derived from the basic equations of fluid dynamics. Due to the length of the pipes, the models are mostly one-dimensional. In addition to the one-dimensional simplification, the wall shear stress is replaced with an expression including the Darcy friction factor, mean velocity and density. To calculate the friction factor the empirical Colebrook-White equation is often used. This data is derived from steady state experiments, making the models quasi-steady. The accuracy of using quasi-steady friction factor in transient flows is not clear. As pointed out later in the text, the stationary assumption is not correct; it is just an approximation.

To investigate the accuracy of the use of quasi-steady modelling, an one-dimensional quasi-steady model is compared with a more detailed fully transient two-dimensional model. The commercial CFD package ANSYS Fluent will be used to simulate the two-dimensional flow. There are several models to choose from, although the choices are restricted by the high Reynolds number flow and the requirement of a

good resolution in the near wall velocity field. In addition to the 1D quasi-steady model, two transient friction models are compared to the 2D results, this to evaluate existing transient friction models which can readily be applied in gas transport models.

The simulated transients are so-called ramp-up and ramp-down flows. In these transients, a step-up or step-down pressure difference is applied to a stationary fully developed flow, and the transients are modelled until a new stationary solution is obtained. A ramp-up simulation is often from a zero velocity to a bulk velocity U_1, and a ramp-down simulation is from a bulk velocity U_0 to zero. In this thesis the transients are kept within either the laminar region or the turbulent region, so a ramp-up and -down goes from U_0 to U_1, where both U_0 and U_1 are in the same flow region.

The commercial pipelines have a wall roughness which in most cases significantly affects the flow. Therefore flow in pipes with simulated wall roughness is also considered. Difficulties involving the roughness height versus near wall resolution were encountered, thus transient results with roughness are limited.

In the simulations the fluid has the characteristics of water and it is incompressible and the viscosity is constant. The long pipeline is simulated with a short pipe using a translational periodic boundary condition to be able to simulate transient without enormous computational domain.

After this introduction, Chapter 2 follows with an introduction into basic fluid dynamics, flow regime, turbulence, friction factor, wall shear stress, and turbulence velocity profile. A short introduction to a typical transient gas transport model is presented in Chapter 3. A turbulent quasi-steady one-dimensional model along with two transient friction models are derived in Chapter 4. In Chapter 5 the necessary properties of the two-dimensional model are identified and a model choice is made with respect to this. Then the selected model (the k-ω model) is described. The 2D model's validity and uncertainties, applied to the problem at hand, are discussed in Chapter 6. Results from the simulations are presented and discussed in Chapter 7 and a conclusion with suggestions to future work is found in Chapter 8.

Chapter 2

Theoretical Background

The theory of gas transport stems from the science of fluid dynamics, which is the main subcategory of fluid mechanics. Fluid dynamics treats liquids and gases in motion. The fluid is treated as a continuous media. In the next sections, the basic governing equations for Newtonian viscous flow and fundamentals of gas pipeline transport theory, will be treated.

2.1 Governing Equations for Pipe Flow

In order to solve gas transport problems, a set of governing differential equations must be identified. The equations follow from the conservation laws for physical systems:

- Conservation of mass.
- Conservation of momentum (Newton's second law).
- Conservation of energy (the first law of thermodynamics).

The conservation laws are formulated for particle systems. In fluid dynamics it is more suitable to see the fluid as a continuum and study the velocity field as a function of time and space, also known as the Eulerian frame of reference. When transforming the velocity field from the particle reference system (Lagrangian) to the Eulerian, the substantial derivative appears. For any fluid property Q, the time derivative becomes [33]

$$\rho\frac{dQ}{dt} = \frac{\partial Q}{\partial t} + u\frac{\partial Q}{\partial x} + v\frac{\partial Q}{\partial y} + w\frac{\partial Q}{\partial z}, \tag{2.1}$$

where the left hand side is normally written as

$$\frac{dQ}{dt} = \frac{DQ}{Dt}.$$

2.1.1 The Equation of Continuity

This equation is a result from the conservation of mass law. The conservation of mass law, states that mass cannot be created or destroyed in a closed system, i.e. the mass differential in a closed system is zero. In fluid dynamics mass is replaced with density times a differential and is transformed to the Eulerian frame of reference using the substantial derivative (2.1). The equation in its most general form reads[34]:

$$\frac{\partial \rho}{\partial t} + \frac{\partial}{\partial x_j}(\rho u_j) = 0, \tag{2.2}$$

here Einstein notation is used where summation over repeated indexes are assumed, where u_i is the component velocities u, v and w and ρ is the density. If it is simplified by assuming incompressible flow, the density will not change with time or space and the resulting equation on component form is

$$\frac{\partial u_j}{\partial x_j} = 0. \tag{2.3}$$

2.1.2 The Momentum Equation

This is Newton's second law applied to fluids, it expresses mass times acceleration being equal to forces on a fluid element. In its general form it is written as

$$\rho \frac{\mathrm{D}u_i}{\mathrm{D}t} = -\frac{\partial \sigma_{ij}}{\partial x_j} + \rho f_i, \tag{2.4}$$

where σ_{ij} is the stress tensor and f_i is an external force, like the gravity. For a Newtonian fluid the stress tensor is defined as

$$\sigma_{ij} = -p\delta_{ij} + \mu\left(\frac{\partial u_i}{\partial x_j} + \frac{\partial u_j}{\partial x_i} - \frac{2}{3}\delta_{ij}\frac{\partial u_k}{\partial x_k}\right), \tag{2.5}$$

where p is the pressure, μ is the dynamic viscosity and δ_{ij} is the Kronecker delta, defined to be unity when indexes are equal. Inserting Equation (2.5) into Equation (2.4) yields the famous Navier-Stokes equations:

$$\rho \frac{\mathrm{D}u_i}{\mathrm{D}t} = -\frac{\partial p}{\partial x_i} + \frac{\partial}{\partial x_j}\left[\mu\left(\frac{\partial u_i}{\partial x_j} + \frac{\partial u_j}{\partial x_i} - \frac{2}{3}\delta_{ij}\frac{\partial u_k}{\partial x_k}\right)\right] + \rho f_i \tag{2.6}$$

The Navier-Stokes equations in its full form are quasi-linear equations. Mathematically it has not yet been proven that there exist a smooth solution, or that if a solution exist it will have bounded velocity[27]. It counts three scalar component equations for the five variables ρ, p and u_i and it has to be supplied with the continuity and the energy equations for a closure. Most analytical solutions that exist are for incompressible non-turbulent flow.

2.1.3 The Energy Equation

Conservation of energy, or the first law of thermodynamics states that the increase of total energy is equal to the sum of the increase of heat and work added to the system.

$$dE = dQ + dW \tag{2.7}$$

The general expression for internal energy is derived from (2.7) and (2.4), the result is (see e.g.[37])

$$\rho \frac{De}{Dt} + p \frac{\partial u_j}{\partial x_j} = \mu\phi + \frac{\partial}{\partial x_j}\left(k \frac{\partial T}{\partial x_j}\right), \tag{2.8}$$

where T is the temperature, e is the internal energy and k is the conductivity. The three primary unknowns that are simultaneously obtained from solving these equations are velocity u_i, pressure p and temperature T. In addition to the five primary variables, the density is related to p and T through an equation of state, and viscosity μ and thermal conductivity k must be given from physical data.

2.1.4 Equation of State

For a compressible fluid a fourth equation to relate pressure, density, and temperature is needed. This is known as the equation of state. In many cases the ideal gas law can be applied:

$$p = \rho R_g T \tag{2.9}$$

where R_g is the ideal gas constant. For non-ideal gases or conditions, a non-dimensional compressibility factor can be introduced to achieve better approximations of real gases

$$pV = \rho Z R_g T. \tag{2.10}$$

There exists other ways to model a more accurate equation of states which will be mentioned later in the text. In all, a three-dimensional compressible fluid flow is described by five differential equations, equation of continuity (2.2), x, y and z component of the momentum equation (2.6) and the energy equation (2.8).

2.2 Flow Regimes

There is no general analytical solution and no general existence or uniqueness theorem to the Navier-Stokes equations. There exist a number of simplifications that will give an exact solution, most of them are for incompressible flow with a simple geometry[33]. So to solve the equations for compressible viscous pipe flow, which appear in gas transport, numerical methods must be utilized. When solving the equations it is important to identify which flow regime is present. There are three flow regimes, namely laminar, transitional, and turbulent flow. In laminar flow the fluid flows in parallel layers; there is no movement perpendicular to the flow direction. Furthermore, laminar flow in pipes is characterized by a parabolic velocity profile, see Figure 2.1, where a laminar and a turbulence velocity profile are shown. Turbulent flow is chaotic, with perpendicular movement, swirls and random

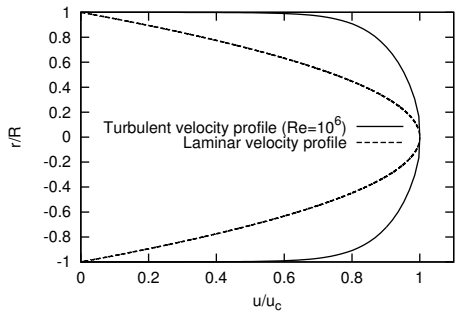

Figure 2.1: A laminar and a turbulent velocity profile.

fluctuations. Between laminar and turbulent regime is the transitional regime. The flow fluctuates at some time interval and is orderly at others. Distinguishing between the flow regimes is done by looking at the ratio between inertial effect and viscous drag, known as the dimensionless Reynolds number Re. The Reynolds number is defined as

$$\mathrm{Re} = \frac{\rho U D}{\mu}, \tag{2.11}$$

where U is the average cross section fluid velocity, D is the diameter, and μ is the fluids dynamic viscosity. A flow will have same flow properties if the Reynolds number is the same. In smooth pipes the flow is laminar for $Re_{\mathrm{crit}} < 2300$, fully turbulent for $Re > 4000$ and transitional in between. These numbers are not exact but common for commercial pipes [34].

2.3 Turbulence

The flow in gas transport pipes during normal daily operation will be well within the turbulent flow regime, so the transport models must solve for a turbulent case. Turbulence has, and will in the foreseeable future be a subject of much research. The first effort of understanding turbulence was done by Osbourne Reynolds, hence the name of the Reynolds number [24]. Turbulence appears when viscous drag no longer can damp fluid property fluctuations induced by inertial effects and wall roughness (if a wall is present) [10].

Turbulence can be characterized by several flow properties: Seemingly random fluctuations in velocity, pressure, temperature and other fluid properties in all directions; although the fluctuation seems random, the fluid properties have specific energy spectrums. The flow is very sensitive to initial conditions and is therefore not repeatable. There is an extreme range of time and length scales, however, the smallest scales are sufficiently large to satisfy the continuum assumption of fluid dynamics. The large rotational motions, known as eddies, will have smaller eddies "feeding" energy from them, the smallest eddies are eventually killed by viscous

dissipation. The turbulent motion is self-sustaining; producing new eddies when other vanish due to viscous dissipation.

All this fluctuation result in greater mixing, heat exchange and friction [33], as compared to the viscous molecular effects.

Due to all the complex behaviour, describing turbulent flow mathematically is difficult. It is assumed that the Navier-Stokes equations are valid for turbulent flow down to the smallest scales, and solutions are obtainable using finite differences or finite elements method. This method is called direct numerical simulations, DNS, and is very computationally costly, restricted to simple geometry and Reynolds number below 10^4. To simulate pipe gas transport with DNS is unrealistic, and even if it were possible, it is not necessary since one will end up with much more information than needed. Less demanding methods are sufficient.

2.3.1 Reynolds Time Averaging

To avoid accounting for all the small-scale fluctuations, one can use Reynolds time averaging. The idea is to separate the main value from the fluctuating value. This is done by decomposing each variable into two parts, the mean and the fluctuating part; for a variable Q this becomes:

$$Q = \bar{Q} + Q',$$

where the averaging operator must satisfy the "Reynolds conditions" [17], which for two turbulent variables, f and g, are as follows:

- The average of the sum is the sum of the averages,

$$\overline{f+g} = \overline{f} + \overline{g}$$

- Constants do not affect averages,

$$\overline{af} = a\overline{f}.$$

  Because of the two first conditions, the operator must be linear.

- The operator is ergodic, meaning that time averaging is equal to space averaging. And the averaging of a derivative of a quantity is equal to the corresponding derivative of the average:

$$\overline{\left(\frac{\partial f}{\partial s}\right)} = \frac{\partial \overline{f}}{\partial s},$$

  where s can be either a time or a space coordinate.

- The average of a product is equal to the product of the averages; taking the average of an average is still just a average.

$$\overline{\overline{f}g} = \overline{f}\,\overline{g}$$

The rest of the conditions can be derived from the above conditions, and they are as follows:

- $$\overline{(\overline{f})} = \overline{f}$$
- $$\overline{f'} = 0$$
- $$\overline{(\overline{f}\overline{g})} = \overline{f}\overline{g} \tag{2.12}$$
- $$\overline{(\overline{f}g')} = 0$$
- $$\overline{\left(\frac{\partial f'}{\partial s}\right)} = 0$$

It is common to use a time dependent averaging operator, because it is difficult measuring space averages and especially so for transient conditions. The time averaging operator is for a turbulent quantity Q defined as

$$\overline{Q} = \frac{1}{T}\int_{t_0}^{t_0+T} Q(t)\,dt, \tag{2.13}$$

where the time period T must be large compared to any relevant fluctuating period for the "Reynolds conditions" to hold. The Reynolds averaging gives us then the mean values, and the result of the fluctuation caused by turbulence. In large gas transport pipe, this is satisfactory, since the interest is the total deliverance, temperature, and other mean properties.

Applying the Reynolds time averaging on the Navier-Stokes equations, we get the Reynolds Averaged Navier-Stokes (RANS). In the RANS equations one ends up with extra correlation terms i.g. $\rho\overline{u_i'u_j'}$. These are then yet other unknowns, and empirical or theoretical relations are needed to obtain a solution. A common approach in gas transport model is to insert friction factor for wall shear stress. This due to the difficulty of measuring and calculating the wall shear in transients.

2.3.2 Turbulent Velocity Profile

In turbulence theory much of the understanding has come from experiments and empirical studies. It is conventional to divide the turbulent velocity profile in to tree layers, they are:

- The inner region, close to the wall, low local Reynolds number, the viscous forces are dominant. Consist of the viscous sublayer, buffer layer, and some of the log-law region.

- the overlap layer, both viscous and turbulent shear are important. Overlaps and connects the inner and outer layer smoothly. Includes the buffer layer and the log-law layer.
- the outer layer, turbulent shear dominates. Can be described partly by the log-law layer and the wake region.

The formulas describing these layers are derived from experiments, dimensional analysis and curve fitting.

2.3.2.1 Dimensionless Parameters

Dimensional analysis is convenient in developing turbulent models, therefore dimensionless variables are introduced.

The velocity scale, also known as the friction velocity, is defined as

$$u_\tau = \sqrt{\frac{\tau_w}{\rho}}. \tag{2.14}$$

The dimensionless length scale, y^+ is defined to be

$$y^+ = \frac{y\sqrt{\tau_w}\rho}{\mu} = \frac{u_\tau y}{\nu}, \tag{2.15}$$

where y is the distance from the wall. From dimensional analysis one get that the mean flow is a function of density, wall distance, viscosity and wall shear stress. The dimensionless velocity u^+ becomes:

$$u^+ = \frac{\overline{u}}{u_\tau} = f\left(\frac{u_\tau y}{\nu}\right) \tag{2.16}$$

Inserting Equation (2.15), will show that u^+ is a function of y^+.

2.3.2.2 Viscous Sublayer

The viscous sublayer is closest to the wall in the inner layer. The local Reynolds number uses length scale based on distance y from the pipe wall $Re_y = \frac{\rho\overline{u}y}{\mu}$. This implies that the local Reynolds number goes towards zero close to the wall, meaning viscous drag must be much greater than inertial forces. The sublayer is very thin, $y^+ < 5$, so one can assume that the shear stress is equal to the wall shear stress and that the turbulent shear stress contribution $\rho\overline{u'v'}$ is zero due to the no-slip boundary condition at the wall.

$$\tau(y) = \mu\frac{\partial\overline{u}}{\partial y} \cong \tau_w \tag{2.17}$$

To get the velocity as function of y, an integration on both sides with respect to y is done

$$\int_0^y \tau_w \, dy' = \mu \int_0^y \frac{\partial\overline{u}}{\partial y'} \, dy'$$

$$\Rightarrow \frac{\tau_w y}{\mu} = \overline{u}(y)$$

Using the dimensionless variables y^+ and u^+ gives for the linear sublayer

$$u^+ = y^+, \tag{2.18}$$

also known as the law of the wall, which is valid for $y^+ < 5$.

2.3.2.3 Buffer Layer

The buffer layer lies between the viscous sublayer and the logarithmic layer. It must connect the two layers, not violating the end and start boundaries. The buffer layer is typically in the region of $5 < y^+ < 60$.

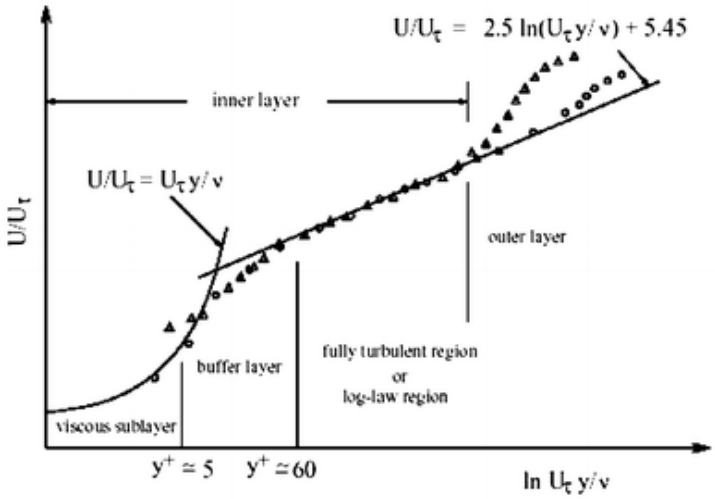

Figure 2.2: Turbulent Boundary Velocity Profile from [36]

2.3.2.4 The Logarithmic Layer

Outside both the viscous sublayer and the buffer layer is the log-law layer, typically for y^+ values between $30 - 500$. Here turbulent and viscous effects are both important. From curve fitting and dimensional analysis one gets that the logarithmic layer is defined by

$$u^+ = \frac{1}{\kappa} \ln(y^+) + B \tag{2.19}$$

This is also known as the log-law of the wall. The constants κ and B have been determined from measurements. From the pipe-flow experiment in 1930 Nikuradse suggested that $\kappa \approx 0.4$ and $B \approx 5.5$ [19]. Coles and Hirst revised these numbers in 1968 to $\kappa \approx 0.41$ and $B \approx 5.0$[33], which will be used in this work.

2.3.2.5 Wake Region

Far away from the wall, the effect from the wall is present in form of the shear stress, but not the viscosity. The suitable length scale is the boundary layer thickness δ, which is the distance from the wall where $\overline{u}(y) = 0.99\overline{u}_{max}$. This means that the dimensionless velocity can be described as function of distance over boundary layer thickness[33].

$$u^+ = f\left(\frac{y}{\delta}\right).$$

Since the local speed is 0.99 of the max flow velocity, the law of the wake is commonly written as

$$\frac{\overline{u}_{max} - \overline{u}}{u_\tau} = -\frac{1}{\kappa}\ln\left(\frac{y}{\delta}\right) + A. \tag{2.20}$$

2.3.3 Turbulent Shear Stress

Shear stress is the force per unit area working between the layers in a fluid. It can be identified in the Navier-Stokes Equations (2.4) as the stress tensor σ_{ij} without the pressure term. For a Newtonian incompressible fluid, the shear stress is given as

$$\tau_{ij} = \mu\left(\frac{\partial\overline{u_i}}{\partial x_j} + \frac{\partial\overline{u_j}}{\partial x_i}\right). \tag{2.21}$$

If the flow is turbulent and Reynolds time averaging is applied on the Navier-Stokes equations, an extra term appears $\rho\frac{\partial}{\partial x_j}\overline{u_i'u_j'}$, where $\rho\overline{u_i'u_j'}$ is a turbulent inertia tensor often referred to as the Reynolds stress tensor. This quantity is a result of momentum transport due to turbulent fluctuation an it is conveniently included as stresses in the shear stress tensor as a turbulent contribution to the shear stress, yielding

$$\tau_{ij} = \mu\left(\frac{\partial\overline{u_i}}{\partial x_j} + \frac{\partial\overline{u_j}}{\partial x_i}\right) - \rho\overline{u_i'u_j'} \tag{2.22}$$

for the total shear stress in the flow.

The shear stress at the wall determines the force acting on the wall from the fluid per unit area. At the wall turbulent fluctuations are zero due to the no-slip boundary condition, and for impermeable surfaces the normal-to-the wall velocity is zero; hence the wall shear stress is given by

$$\tau_w = \mu\left(\frac{\partial\overline{u}}{\partial y}\right)_{y=0}, \tag{2.23}$$

where y is the perpendicular distance from the wall. The wall shear stress is difficult to calculate since the detailed velocity field close to the wall must be known.

2.3.4 Friction Factors

There are two definitions for friction, namely the Darcy friction factor and the Fanning friction factor, also known as the skin friction coefficient. Both friction

factors are dimensionless, like the Reynolds number. The Darcy friction factor is based on the pressure drop and defined as[33]

$$f = \frac{-\frac{dp}{dx}D}{\frac{1}{2}\rho U^2}. \tag{2.24}$$

The Fanning friction factor is based on the wall shear stress, and the definition is[33]

$$C_f = \frac{\tau_w}{\frac{1}{2}\rho U^2}, \tag{2.25}$$

here U is the average velocity for a cross section of a pipe. Traditionally the Fanning friction factor is used in aerodynamics while the Darcy friction factor is widely used in pipe fluid flow. The Darcy friction factor can be used to determine the required pressure to obtain a wanted Reynolds number. Substituting the Reynolds number gives

$$f = \frac{-\frac{dp}{dx}D}{\frac{1}{2}\rho\left(\frac{Re\mu}{\rho D}\right)^2} \tag{2.26}$$

solving for pressure

$$\frac{dp}{dx} = -f\frac{(\mu Re)^2}{2\rho D^3} \tag{2.27}$$

This can be solved since the friction factor is a function of Reynolds number and wall roughness, see e.g. Equation (2.40).

2.3.5 Relation between Fanning and Darcy Friction Factor

To find an equivalence between the two friction factors, one can make a momentum analysis on a pipe segment for a steady case, see Figure 2.3.

Without acceleration the force balance is

$$\int_{A_1} p_1\, dA - \int_{A_2} p_2\, dA - \int_S \tau_w\, dS = 0 \tag{2.28}$$

Since R is constant, $A_1 = A_2$

$$\int_0^R (p_1 - p_2)2\pi r\, dr = \int_0^L dx \int_0^{2\pi} R\, d\theta\, \tau_w$$

$$-\Delta p \pi R^2 = 2\pi RL\tau_w \Rightarrow \tau_w = -\frac{\Delta pD}{4L} \tag{2.29}$$

using that $\Delta p/L = dp/dx$ for incompressible flow, we get

$$\tau_w = -\frac{D}{4}\frac{dp}{dx}. \tag{2.30}$$

Substituting the right hand side into Equation (2.25) and inspecting the Darcy friction factor to get that $f = 4C_f$ for steady flow.

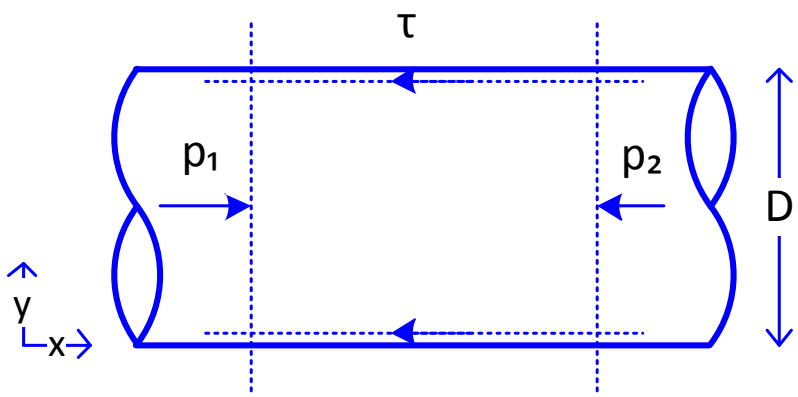

Figure 2.3: Force Balance on a Pipe Segment

2.3.6 Friction Factor in Smooth Pipes

Finding an expression for the fanning friction factor can be done with the help from the velocity profile formula. For a pipe the wake is almost non existent and the linear layer is so thin that a good approximation to the whole velocity profile is to use the logarithmic log law of the wall (2.19). Then integrating this over the area, dividing it by the cross section.

$$U = \frac{1}{\pi R^2} \int_0^R \left(\frac{u_\tau}{\kappa} \ln \left(\frac{u_\tau y}{\nu} \right) + B \right) 2\pi r \, dr \tag{2.31}$$

resulting in the following equation

$$U = u_\tau \left(\frac{1}{\kappa} \ln \left(\frac{u_\tau R}{\nu} \right) + B - \frac{3}{2\kappa} \right) \tag{2.32}$$

Then using the Fanning friction factor definition (2.25) and that $f = 4C_f$ one ends up with an implicit equation for the Darcy friction factor, derived by Prandtl in 1930.

$$\frac{1}{f^{1/2}} = 1.99 \log_{10} \left(Re_D f^{1/2} \right) - 1.02 \tag{2.33}$$

He adjusted the constants to accommodate for the wake that was neglected. The revised equation is:

$$\frac{1}{f^{1/2}} = 2 \log_{10} \left(Re_D f^{1/2} \right) - 0.8 \tag{2.34}$$

2.3.7 Finite Roughness

The above friction factors are derived for smooth pipes. If the pipe has a roughness some adjustments must be made. In the 1930is Nikuradse measured the velocity profile and pressure drop in smooth pipes[19] and later in rough pipes. All the measurements were done during steady state conditions over a wide range of Reynolds number, $4 \cdot 10^4$ to $3 \cdot 10^6$. The roughness was made by uniformly gluing sand grains on the inside of the pipe. The data-sets from different roughness factors are depicted in Figure 2.4. He found that for high Reynolds number the friction factor becomes independent of the Reynolds number.

The roughness height is taken to be the average roughness height. As is normal the roughness height can be expressed with a dimensionless number. This dimensionless number, the wall hight parameter, k^+,is defined by

$$k^+ = \frac{ku_\tau}{\nu}. \tag{2.35}$$

This can be used to classify the roughness regime of the flow[33]:

$$\begin{aligned} k^+ &< 4 \rightarrow \text{hydraulically smooth} \\ 4 < k^+ &< 60 \rightarrow \text{transitional} - \text{roughness regime} \\ k^+ &> 60 \rightarrow \text{fully rough regime.} \end{aligned}$$

The roughness greatly interferes with the viscous sublayer, making the law of the wall dependent on roughness height as well as y^+; yielding

$$u^+ = f(y^+, k^+).$$

The overlap layer is also affected, displacing the velocity profile away from the wall

$$u^+ = \frac{1}{\kappa} \ln \frac{yu_\tau}{\nu} + B - \Delta B(k^+) \tag{2.36}$$

where for sand grain the displacement curve is

$$\Delta B(k^+) \approx \frac{1}{\kappa} \ln(1 + 0.3k^+). \tag{2.37}$$

For fully rough flow $k^+ > 60$ Equation (2.36) reduces to

$$u^+ = \frac{1}{\kappa} \ln \left(\frac{y}{k} \right) + 8.5 \tag{2.38}$$

2.3.7.1 Nicuradse and Colebrook-White Friction Formulas

From the measured velocity profile in Nicuradse's experiments a friction relation for sand-grain roughness can be found

$$\frac{1}{\sqrt{f}} \approx -2.0 \log_{10} \left(\frac{Re\sqrt{f}}{1 + 0.1(k/D)Re\sqrt{f}} + \right) - 0.8. \tag{2.39}$$

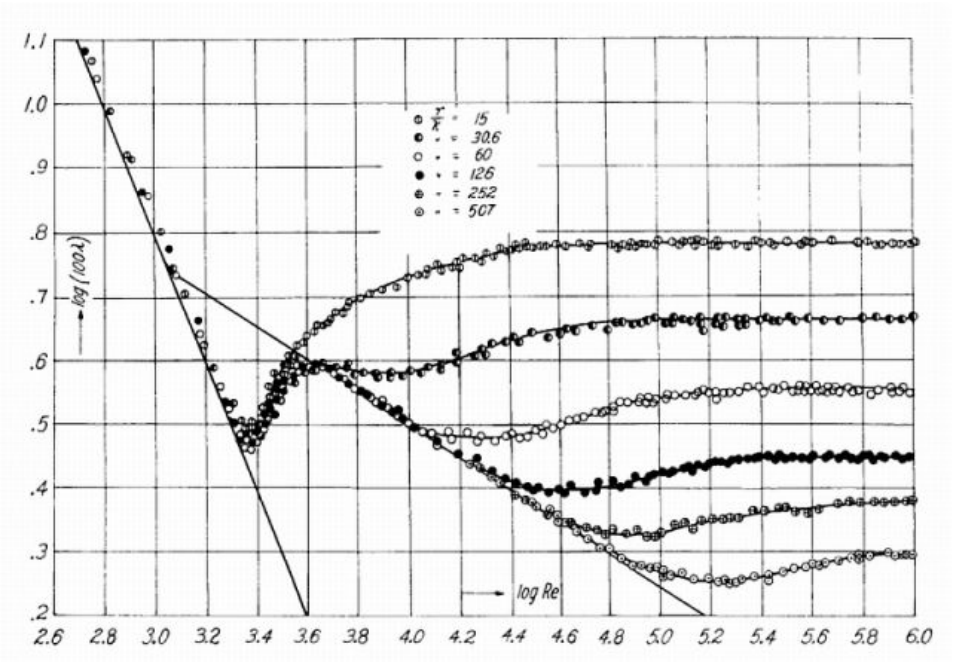

Figure 2.4: Data plot from Nikuradse's experiment

Uniform sand grain roughness is not equal to the roughness we find in commercial pipes. Colebrook did measurements on typical commercial pipes, from this he derived the Colebrook-White formula

$$\frac{1}{\sqrt{f}} \approx -2.0 \log_{10}\left(\frac{k/D}{3.7} + \frac{2.51}{Re\sqrt{f}}\right). \tag{2.40}$$

In 1944 Moody[18] plotted this equation for different roughness's as a function of logarithmic Reynolds number. The famous Moody chart is presented in Figure 2.5. It can be noted that these equations are also valid for smooth pipes without wall roughness, by letting $k/D \to 0$.

2.3.8 Transient Friction

When treating transient flow it is convenient to use the Fanning friction factor. To find an expression for the transient Fanning friction factor the transient wall shear stress must be found. During transient flows the wall shear stress is not the same as during steady flow conditions,

$$\begin{aligned} \tau_w &\neq -\frac{D}{4}\frac{\mathrm{d}p}{\mathrm{d}x} \\ \Rightarrow f &\neq 4C_f \end{aligned} \tag{2.41}$$

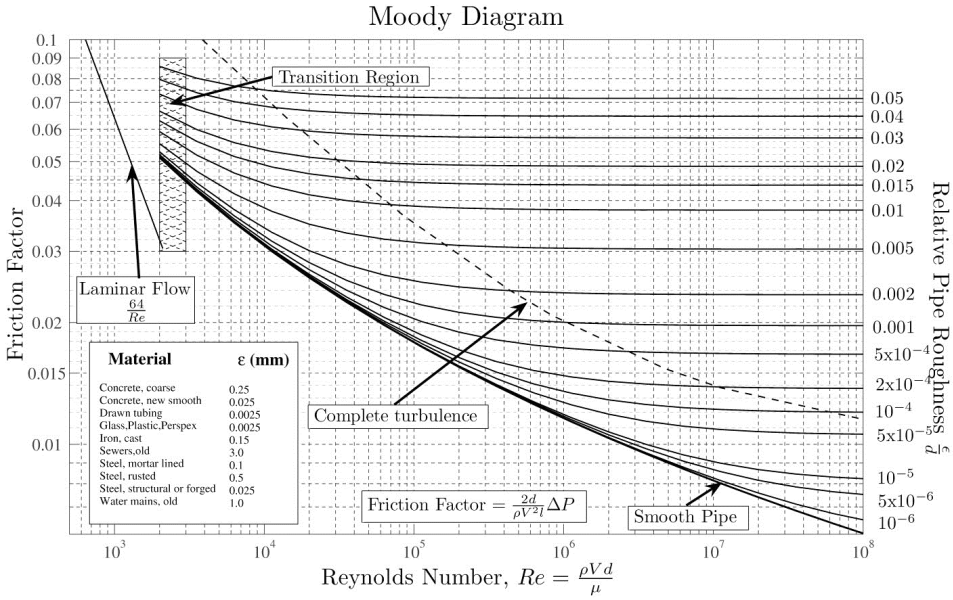

Figure 2.5: Moody chart

To show this one can once again make a force balance on a pipe segment as in Figure 2.3, but letting the unsteady term be non-zero. It is convenient to write the Navier-Stokes equation on conservation form; i.e:

$$\frac{\partial \rho u_i}{\partial t} + \frac{\partial}{\partial x_j}\left(\rho u_i u_j\right) = -\frac{\partial p}{\partial x_i} + \frac{\partial}{\partial x_j}\tau_{ij}, \tag{2.42}$$

where the general transformation

$$\rho\frac{DQ}{Dt} \rightarrow \frac{\partial}{\partial t}\left(\rho Q\right) + \frac{\partial}{\partial x_j}\left(\rho u_i Q\right) \tag{2.43}$$

has been applied. For incompressible flow the density stays constant and the viscous stress term $\frac{\partial}{\partial x_j}\left[\mu\left(\frac{\partial u_i}{\partial x_j} + \frac{\partial u_j}{\partial x_i} - \frac{2}{3}\delta_{ij}\frac{\partial u_k}{\partial x_k}\right)\right]$ simplifies as $\frac{\partial u_i}{\partial x_i} = 0$ and $\mu =$ constant.

Integrating over the control volume Adx, assuming that the flow is fully developed $\left(\frac{\partial u}{\partial x} = 0\right)$, and applying the divergence theorem yields:

$$\begin{aligned}\int_V \rho\frac{\partial u_i}{\partial t}\, dAdx &= -\oiint_A \vec{p}\cdot\vec{n}\, dsdx + \oiint_A \tau_{ij}|_{r=R}\, n_j\, dsdx \\ &= -A\, dp + 2\pi R\, \tau_{xr}|_{r=R}\, dx \\ \Rightarrow \rho\frac{\partial}{\partial t}\left(\frac{1}{A}\int_A u\, dA\right) dx &= -\, dp - \frac{2\pi R}{\pi R^2}\tau_w\, dx\,.\end{aligned} \tag{2.44}$$

Inserting cross sectional average velocity $U = \frac{1}{A}\int_A u\,dA$ and cleaning up:

$$\rho\frac{\partial U}{\partial t} = -\frac{dp}{dx} - \frac{2}{R}\tau_w. \tag{2.45}$$

Solving for the wall shear stress gives;

$$\tau_w = -\frac{D}{4}\frac{\partial p}{\partial x} - \frac{\rho D}{4}\frac{\partial U}{\partial t}. \tag{2.46}$$

This equation results from a purely one-dimensional analysis, and does not account for non-uniform acceleration of the velocity profile which will alter the near wall velocity gradients and thus the wall shear stress.

The Equation (2.46) indicates that for an incompressible flow, there is a transient contribution to the wall shear stress. The contribution is proportional to the local acceleration.

2.4 Transient Friction Modelling

In fluid mechanics it is convenient to define the total wall shear stress and the total friction factor as a sum of the steady and the unsteady components [6]:

$$\begin{aligned} \tau_w &= \tau_{ws} + \tau_{wu}, \\ C_f &= C_{fs} + C_{fu}. \end{aligned} \tag{2.47}$$

The subscripts s and u in Equation (2.49) stands for steady component and unsteady component respectively. This splitting of the transient wall shear stress and friction factor is done because the steady components are well known, and the transient contribution can be modelled separately according to fluid acceleration and other quantities.

From the equations (2.46) and (2.47) we get:

$$\tau_{wu} \propto \frac{\rho D}{4}\frac{dU}{dt}, \tag{2.48}$$

$$C_{fu} \propto \frac{D}{2U^2}\frac{dU}{dt}\,. \tag{2.49}$$

To account for additional damping of the wall shear stress found in experimental results, Daily et al. (1956) [9] proposed that $C_{fu} = k_1\frac{D}{2U^2}\frac{dU}{dt}$, where k_1 is a non-dimensional coefficient determined by theoretical or experimental work. Daily et al. proposed values for k_1 of 1.2 for accelerating flows and 0.02 for decelerating flows. Carstens et al. (1959) [8] suggested that $k_1 \approx 0.449$ for both accelerating and decelerating flow. From theoretical work Carstens et al. advocated that k_1 was dependent upon the Reynolds number.

The Brunone model [1] adds convective acceleration $\frac{\partial U}{\partial x}$ to the unsteady friction component. The model gives a good match between the computed and measured

results using an empirically predicted (by trial and error) friction coefficient k_3 (known as the Brunone unsteady friction coefficient).

In 1968 Zielke derived a transient friction model for laminar frequency dependent viscous flow [41]. The unsteady friction is related to instantaneous mean flow velocity and to weighted past velocities. In Zielkes model the unsteady component of the wall shear stress is linked to the acceleration history through a weighted integral

$$\tau_{wu} = \frac{2\rho\nu}{R} \int_0^T W\{T-\theta\} \frac{\partial U}{\partial t}\, d\theta, \tag{2.50}$$

where W is a weighting function and T is the elapsed time since the flow was stationary. The parameter t and θ are times measured forwards and backwards respectively. The model has been modified by several researches to develop weighting functions for turbulent flow.

From an idealized form of the radial viscosity distribution and assuming that changes in the viscosity distribution may be neglected during transient periods, Vardy et al. (2003 [29] and 2004 [30]) derived simplified weighting functions for turbulent smooth wall flows and turbulent fully rough flows. For smooth wall flows the simplified weighting function is

$$W_a = \frac{\sqrt{\nu_w/\nu_{lam}}\exp\left(-\psi/C^*\right)}{2\sqrt{\pi\psi}}, \tag{2.51}$$

in which ψ is the non-dimensional time and C^* is the shear decay coefficient. The non-dimensional time is defined by

$$\psi = \frac{\nu_{lam}\theta}{R^2} \tag{2.52}$$

The shear decay coefficient C^* is dependent upon the Reynolds number, from regression analysis Vardy et al. [29] expressed C^* as a function of Reynolds number;

$$C^* = \frac{12.86}{Re^{\kappa}}, \tag{2.53}$$

where

$$\kappa = \log_{10}\left(\frac{15.29}{Re^{0.0567}}\right). \tag{2.54}$$

The Equation (2.53) is valid in the range $2000 < Re < 10^8$.

For fully rough flow the simplified weighting function is [30]

$$W_{ar} = \frac{A^*\exp\left(-\psi/C_r^*\right)}{\sqrt{\psi}}, \tag{2.55}$$

where the parameters A^* and C_r^* can be approximated by

$$\begin{aligned} A^* &\approx 0.0103\sqrt{Re_\nu}\epsilon^{0.39}, \\ C_r^* &\approx \frac{1}{0.352 Re_\nu \epsilon^{0.41}} \end{aligned} \tag{2.56}$$

By considering the special case of constant accelerating transients the unsteady skin friction was derived;

$$f_u \approx 2\sqrt{C^*}\,\mathrm{erf}\left(\sqrt{\psi/C*}\right) \tag{2.57}$$

and for fully rough flow;

$$f_u \approx 4A^*\sqrt{\pi C_r^*}\,\mathrm{erf}\left(\sqrt{\psi/C*_r}\right), \tag{2.58}$$

where the error function $\mathrm{erf}(\psi = 0) = 0$ and approaches unity as $\psi \to \infty$. Vardy et al[28] linked the limiting value of the unsteady friction in equations (2.57) and (2.58) to the Brunone unsteady friction coefficient used in the Brunone et al model:

$$k_3 = 2\sqrt{C^*} \tag{2.59}$$

and for fully rough flow;

$$k_3 = 4A^*\sqrt{\pi C_r^*}. \tag{2.60}$$

If the transients accelerate approximately constant for a limiting time ψ_{TL}, then the instantaneous acceleration model is a reasonable approximation. The limiting rise time is the non-dimensional time it takes for the error function to attain a value of 0.99. For smooth flow the limiting rise time is

$$\psi_{TL} = 3.323C^*, \tag{2.61}$$

and for rough flow it is

$$\psi_{TLr} = 3.317C_r^*. \tag{2.62}$$

To summarize, there are two main approaches to model transient friction that are applicable in one-dimensional transient models. The first of these methods, models the transient friction according to instantaneous mean velocities and accelerations (e.g.[9] and [1]). The second approach models the transient friction by accounting for the velocity history of the flow via a weighting integral (e.g. [41], [39], [29] and [30]).

The first category of models needs only the local acceleration and the local velocity and are therefore numerically cheap. On the other hand, they lack the ability to capture more complex behaviour and is presumed to have lower accuracy than weighting function models. The weighting function approach have reportedly high accuracy right after the unsteadiness was initiated, the accuracy decreases as the time increases. It is also computational costly compared to instantaneous acceleration models seeing as the weighting function must be integrated at each time-step.

Chapter 3

Gas Transport Models

Application of gas transport models are numerous: In the planning and building process they can be used to calculate dimensions of the pipe-lines and the pressure required at pumping stations. To plan and maintain deliveries to the consumers with correct pressure, within the tolerance stated in the laws of gas trade. As a real time monitoring system to automatically detect leaks, unwanted slug creation, and other anomalies[40]. Optimize pipe capacity; postponing expensive infrastructural upgrades.

The pipes have flow meters, pressure transmitters and quality measurement only at inlet and outlet. So all information of the state of the gas between inlet and outlet will have to be simulated using gas transport models. Most commercial pipeline simulators for long transport pipes differ little from each other, a short introduction into a typical model is presented in the next sections.

From this point on, to simplify notation, the bar over the cross-sectional average velocity is omitted; i.e. $\overline{U} \Rightarrow U$.

3.1 One-Dimensional Equations

To model such great distances as in gas transport, the equations are usually made one-dimensional. The equations must also be valid in the turbulent flow regime, thus the equations are Reynolds time averaged. The set of equations for gas transport flow is stated as the following[15]:

Conservation Equation

$$\frac{\partial \rho}{\partial t} + \frac{\partial}{\partial x}(\rho U) \tag{3.1}$$

where the x-direction is in the pipe axial direction.

The momentum equation

$$\rho\frac{\partial U}{\partial t}+\rho U\frac{\partial U}{\partial x}=-\frac{\partial \overline{p}}{\partial x}+\rho g\sin\alpha-\frac{1}{2}\rho U\left|U\right|\frac{f}{D}. \tag{3.2}$$

where α is the incline of the pipe and g is the gravitational force. Here the Darcy friction factor f is inserted through the assumption that Equation (2.30) is a sufficiently good approximation.

The Energy Equation

$$\rho c_v\left(\frac{\partial T}{\partial t}+U\frac{\partial T}{\partial x}\right)=T\left(\frac{\partial p}{\partial T}\right)_\rho\frac{\partial U}{\partial x}+\rho\frac{f}{2D}U^3-\frac{4U_{W,tot}}{D}\left(T_{gas}-T_{env}\right), \tag{3.3}$$

where $U_{W,tot}$ is the total heat transfer coefficient between the gas and the pipe environment and is defined as

$$U_{W,tot}=\frac{Q_{tot}}{(T_{gas}-T_{env})A}.$$

The second term on the right hand side in the energy equation represent the energy dissipation due to viscosity and turbulence.

3.2 Solution Methods

From the three balances mass balance, momentum balance and energy balance, one ends up with a set of partial differential equations (PDE). Where there are two independent variables, x and t. The dependent variables can be density, mass flux and energy. There are several numerical methods that can be used to solve the equations. Among them are the finite volume method (FVM), the method of characteristics (MOC), the finite difference method (FDM) and the finite element method (FEM). The most popular of these numerical methods used in pipeline models is the finite differencing method[15], although other methods has been applied with success[20].

In the finite difference method, the pipeline is divided into equally sized segments. The connection points between these segments are called knots. The derivatives in the partial differential equations are approximated by a finite difference equation. These finite differences are algebraic and the solution is related to the knots. In Langelandsvik's PHD thesis[15] a transient gas transport model, Transient Gas Network (TGNet), which uses FDM is described. The mass and momentum equations are discretised using the box scheme[14]. For a pipe segment the equations can be written as

$$\frac{\partial u}{\partial t}+A(x,u)\frac{\partial u}{\partial x}=F(x,t,u), \tag{3.4}$$

where

$$u=\begin{bmatrix}\rho\\ \dot{m}\end{bmatrix}$$

$$A(x,u) = L^{-1}\begin{bmatrix} 0 & 1 \\ \gamma^2 - \nu^2 & 2\nu \end{bmatrix}$$

$$F(x,t,\rho,\dot{m}) = \left[0, \frac{-f\dot{m} \mid \dot{m} \mid}{2D\rho} - L^{-1}\rho g \sin\alpha\right]^T.$$

Here γ is gas sound velocity and ν is the gas velocity. The finite difference method suffers from instability if it encounters non-linear algebraic problems, and as a result $A(x,u)$ and $F(x,t,\rho,\dot{m})$ are linearised about the solution at the jth time level when solving for $j+1$ time level. After the linearisation the simulator evaluates the variables at the new and old time step from the midpoint $(x_{i+1/2}, t_{j+1/2})$. From this a complete set of difference equations are obtained

$$\begin{aligned}
U(x_{i+1/2},t_j) &= \frac{1}{2}\left(U\left(x_{i+1},t_j\right) + U\left(x_i,t_j\right)\right) \\
U(x_i,t_{j+1/2}) &= \frac{1}{2}\left(U\left(x_i,t_{j+1}\right) + U\left(x_i,t_j\right)\right) \\
\frac{\partial U}{\partial x}(x_{i+1/2},t_{j+1/2}) &= \frac{1}{\Delta t}\left(U\left(x_{i+1/2},t_{j+1}\right) - U\left(x_{i+1/2},t_j\right)\right) \\
\frac{\partial U}{\partial x}(x_{i+1/2},t_{j+1/2}) &= \frac{1}{h}\left(U\left(x_{i+1},t_{j+1/2}\right) - U\left(x_i,t_{j+1/2}\right)\right) \\
\frac{\partial U}{\partial x}(x_{i+},t_j) &= \frac{1}{h}\left(U\left(x_{i+1},t_j\right) - U\left(x_i,t_j\right)\right)
\end{aligned} \tag{3.5}$$

In Figure 3.1 the box scheme is schematically drawn up, the knots are market

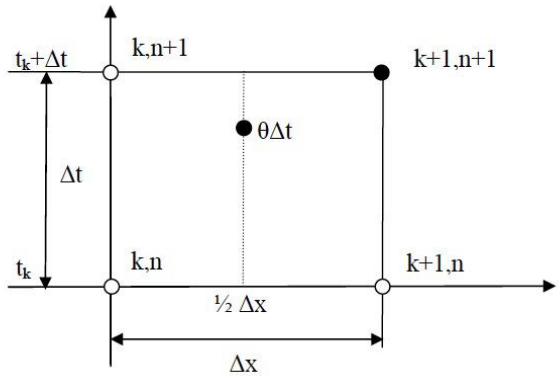

Figure 3.1: Numerical box scheme schematic[15]

by k and the time step i marked with n. In the box the unknowns are in the next time step (x_i, t_{j+1}) and (x_{i+1}, t_{j+1}). They are dependent upon the previous time step (x_i, t_j) , (x_{i+1}, t_j) and its neighbour, so that (x_i, t_{j+1}) is also dependent on (x_{i+1}, t_{j+1}) and vice versa. This is an implicit method where the all the next time step must be solved simultaneously. This can be done by first factorizing the

matrices into a lower and upper triangular matrix and then using the Gauss-Seidel or the more popular, Thomas algorithm (TDMA). After the mass and momentum balance is solved for the new time step, the energy equation is solved. This is done due to the fact that the temperature response is significantly slower than the hydraulic response.

3.3 Heat Transfer

The heat transfer is dependent on three factors. The heat transfer between the surrounding to the outside of the outer pipe wall, the isolation of the pipe wall and the heat transfer from the gas flow to the inner wall of the pipe. The outer heat transfer depends on burial depth and exposure to water. With different heat coefficient whether it is deep burial or shallow burial. Having good temperature data at sea bottom is important to get accurate solution of the energy equation [11]

3.4 Friction Factor

In most transient gas transport models the friction factor is modelled with the stationary friction factor at the instantaneous Reynolds number; neglecting any transient contribution of the friction. This is a reasonable approximation during slow transients, but it will reduce the model accuracy during fast transients.

The friction factor correlation most commonly used in transient gas transport models is the Colebrook-White Equation (2.40). To calibrate the model and correct for additional drag effects an EFF can be multiplied to compensate for additional drag effect

$$\frac{1}{\sqrt{f}} \approx -2.0 \log_{10} \left(\frac{k/D}{3.7} + \frac{2.51}{Re_D \sqrt{f}} \right) EFF \,.$$

Before new pipelines are installed, the roughness of the wall are measured. For coated and uncoated pipelines the roughness height is within the range of 6.4µm and 19.1µm respectively[26]. If the measurements of the wall roughness is accurate and the models correctly depict the drag, a lot of time, and thus money, can be saved when calibrating the numerical model to the pipeline.

Chapter 4

One Dimensional Numerical Models

To be able to solve the flow problem numerically, for both one-dimensional and two-dimensional flow, the flow is assumed to be incompressible and isothermal. Moreover, it is assumed that no external force is applied to the flow.

4.1 Incompressible Flow and Conservation Form

For the treatment of turbulent flow the Navier-Stokes equations are written on conservation form and simplified in the same manner as Equation (2.42).

$$\frac{\partial}{\partial t}\left(\rho u_i\right) + \frac{\partial}{\partial x_j}\left(\rho u_i u_j\right) = -\frac{\partial p}{\partial x_i} + \frac{\partial}{\partial x_j}\tau_{ij}. \tag{4.1}$$

4.2 Reynolds Averaging

In incompressible and isothermal flow there are two turbulent variables. From the Reynolds decomposition we then have

$$u_i = \overline{u}_i + u_i',$$

and

$$p = \overline{p} + p'.$$

Substituting these variables into the incompressible continuity equation and time averaging the equation gives

$$\overline{\frac{\partial\left(\overline{u_i} + u_i'\right)}{\partial x_i}} = 0 = \frac{\partial \overline{u_i}}{\partial x_i}.$$

Inserting the variables into the Navier-Stokes equations yields

$$\frac{\partial}{\partial t}\rho\left(\overline{u}_i + u_i'\right) + \frac{\partial}{\partial x_j}\left(\overline{u}_i + u_i'\right)\left(\overline{u}_j + u_j'\right) = \frac{\partial}{\partial x_i}\left(\overline{p} + p'\right) + \frac{\partial}{\partial x_j}\left(\overline{\tau}_{ij} + \tau_{ij}'\right). \tag{4.2}$$

Averaging and rewriting yields

$$\frac{\partial}{\partial t}\rho\overline{u}_i + \frac{\partial}{\partial x_j}\left(\rho\overline{u}_i\overline{u}_j\right) = -\frac{\partial\overline{p}}{\partial x_i} + \frac{\partial}{\partial x_j}\left(\tau_{ij} - \overline{\rho u_i' u_j'}\right), \tag{4.3}$$

where the term $-\overline{\rho u_i' u_j'}$ represents stresses caused by the turbulent fluctuations, in analogy with the viscous stresses $\overline{\tau}_{ij}$ which results from random molecular motions.

4.3 Turbulent Pipe Flow

Equation (4.3) is simplified as the flow is fully developed $\frac{\partial\overline{u}}{\partial x} = 0$. Integrating the resulting equation over the control volume $A\,dx$:

$$\int_V \frac{\partial}{\partial t}\rho\overline{u}\,dV = -\int_V \frac{\partial\overline{p}}{\partial x_i}\,dV + \int_V \frac{\partial}{\partial x_j}\left(\tau_{ij} - \overline{\rho u_i' u_j'}\right)dV\,. \tag{4.4}$$

Applying the divergence theorem gives

$$\int_V \frac{\partial}{\partial t}\rho\overline{u}\,dAdx = -\oiint_A \vec{p}\cdot\vec{n}\,ds\,dx + \oiint_A \left(\overline{\tau}_{ij} - \rho\overline{u_i' u_j'}\right)\Big|_{r=R} n_j\,ds\,dx \tag{4.5}$$

$$= -A\,dp + \left(\tau_{xr} - \rho\overline{u_x' u_r'}\right)\Big|_{r=R} 2\pi R\,dx \tag{4.6}$$

$$\begin{aligned}\Rightarrow \frac{\rho}{A}\frac{\partial}{\partial t}\int_V \overline{u}\,dAdx &= -dp - \left(\tau_{xy} - \rho\overline{u_x' u_y'}\right)_w \frac{2\pi R}{\pi R^2}\,dx \\ = \rho\frac{\partial U}{\partial t}\,dx &= -dp - \left(\tau_{xy} - \rho\overline{u_x' u_y'}\right)_w \frac{2}{R}\,dx\end{aligned} \tag{4.7}$$

$$\Rightarrow \frac{\partial U}{\partial t} = -\frac{1}{\rho}\frac{dp}{dx} - \tau_w\frac{2}{\rho R}. \tag{4.8}$$

From the definition of the Fanning friction factor (2.25) we get the wall shear stress in terms of friction, velocity, and density

$$C_f = \frac{\tau_w}{\frac{1}{2}\rho U^2} \Rightarrow \tau_w = \frac{1}{2}C_f\rho U^2. \tag{4.9}$$

Substituting the wall shear stress into Equation (4.8) and replacing radius with diameter gives

$$\frac{\partial U}{\partial t} = -\frac{1}{\rho}\frac{dp}{dx} - \frac{2C_f U\,|U|}{D}, \tag{4.10}$$

where the absolute value is taken of U on the right hand side to ensure correct sign of the term regardless of flow direction and acceleration.

For high Reynolds numbers the friction factor is approximately constant, see chart 2.5. Equation (4.10) can therefore be regarded as a first order non-linear differential equation;

$$\frac{dU}{dt} = \alpha - \beta U\,|U|\,, \tag{4.11}$$

where the parameters α and β are:

$$\begin{aligned} -\frac{1}{\rho}\frac{dp}{dx} &= \alpha \geq 0 \\ \frac{2C_f}{D} &= \beta > 0 \end{aligned} \tag{4.12}$$

Equation (4.11) can be solved by first dividing the equation with $\alpha - \beta U(t)^2$;

$$\frac{\frac{\partial U(t)}{\partial t}}{\alpha - \beta U(t)\,|U(t)|} = 1, \tag{4.13}$$

then integrating with respect to t

$$\int \frac{\frac{\partial U(t)}{\partial t}}{\alpha - \beta U(t)\,|U(t)|}\,dt = \int 1\,dt, \tag{4.14}$$

and evaluating the integrals

$$\Rightarrow \frac{\tanh^{-1}\left(\sqrt{\frac{\beta}{\alpha}}U(t)\right)}{\sqrt{\alpha\beta}} = t + C, \tag{4.15}$$

where C is an integrating constant determined by the initial condition. Solving the equation for $U(t)$ gives

$$U(t) = \sqrt{\frac{\alpha}{\beta}}\tanh\left(\sqrt{\alpha\beta}\,(t + C)\right). \tag{4.16}$$

Solving for the initial condition $U(0) = U_0$ yields

$$U(0) = U_0 = \sqrt{\frac{\alpha}{\beta}}\tanh\left(\sqrt{\alpha\beta}C\right), \tag{4.17}$$

$$\Rightarrow C = \frac{1}{\sqrt{\alpha\beta}}\tanh^{-1}\left(\sqrt{\frac{\beta}{\alpha}}U_0\right). \tag{4.18}$$

The full solution is

$$U(t) = \sqrt{\frac{\alpha}{\beta}}\tanh\left(\sqrt{\alpha\beta}\left(t + \frac{1}{\sqrt{\alpha\beta}}\tanh^{-1}\left(\sqrt{\frac{\beta}{\alpha}}U_0\right)\right)\right), \tag{4.19}$$

where α and β are parameters defined in Equation (4.12). α is constant if the pressure difference and the density is constant, which is the case during ramp-up and ramp-down transients used in this thesis. The parameter β varies with the friction factor, which may be modelled by friction models mentioned in Section 2.4. In this work three different friction models were implemented in the 1D turbulence model. These friction models are the quasi-steady friction model, the Daily et al. model with the Brunone unsteady friction coefficient k_3, and the Vardy and Brown frozen viscosity weighting friction model. An outline of the implementations of these models are found in Section 4.5.

4.4 Fully Developed Laminar Pipe Flow

In order to analyse 2D Fluent results in the laminar region a 1D model for laminar flow was needed. Integrating Equation 2.42 over the control volume Adx and assuming that the flow is fully developed, yields

$$\frac{dU}{dt} = -\frac{1}{\rho}\frac{dp}{dx} - \tau_w \frac{4}{\rho D}. \tag{4.20}$$

Recalling the definition of the Fanning friction factor

$$C_f = \frac{\tau_w}{\frac{1}{2}\rho U^2}, \tag{4.21}$$

and furthermore in laminar flow

$$C_{fs} = \frac{16}{Re}. \tag{4.22}$$

Inserting Equation 4.21 and including the stationary Fanning friction factor 4.22 gives:

$$\begin{aligned} \frac{dU}{dt} &= -\frac{1}{\rho}\frac{dp}{dx} - \frac{2C_f U^2}{D} \\ &= -\frac{1}{\rho}\frac{dp}{dx} - \frac{2\left(C_{fs} + C_f u\right)U^2}{D}, \end{aligned} \tag{4.23}$$

$$\frac{dU}{dt} = -\frac{1}{\rho}\frac{dp}{dx} - \frac{32\mu U}{D^2\rho} - \frac{2C_{fu}U^2}{D} \tag{4.24}$$

Assuming that the unsteady component is very small, Equation 4.24 may be rearranged into a linear differential equation of the form

$$\dot{U} + \kappa U = \gamma, \tag{4.25}$$

where γ and κ are the parameters defined by

$$\gamma = -\frac{1}{\rho}\frac{dp}{dx}, \qquad \kappa = \frac{32\mu}{\rho D^2} - \frac{2C_{fu}U}{D} \tag{4.26}$$

Solving the linear differential Equation 4.25 may be done by first multiplying it with $e^{-\kappa t}$ and using the product rule for derivatives

$$\int \left(\frac{\partial U}{\partial t}e^{-\kappa t} - \kappa U e^{-\kappa t}\right) dt = \int \left[\frac{\partial}{\partial t}\left(U e^{-\kappa t}\right)\right] dt = \int \gamma e^{-\kappa t}\, dt\,.$$

This equates to

$$U e^{-\kappa t} = \frac{\gamma e^{-\kappa t}}{-\kappa} + C \qquad \Rightarrow U = -\frac{\gamma}{-\kappa} + C e^{\kappa t}.$$

C is an integrating constant and is found from the initial condition

$$U(t=0) = U_0 \Rightarrow C = \frac{\kappa}{\gamma} + U_0.$$

The end result is a one-dimensional solution which can be used to model laminar flow subjected to constant pressure difference

$$U(t) = \frac{\gamma}{-\kappa} + \left(U_0 + \frac{\gamma}{\kappa}\right) e^{\kappa t}. \tag{4.27}$$

The unsteady component of the Fanning friction factor residing in the parameter κ may be modelled by several methods, where a few are mentioned in Section 2.4. In this thesis two friction models where implemented; the quasi-steady friction model, which neglects the unsteady component altogether and the Daily et al. model with constant friction coefficient k_1.

4.5 Numerical Models

To model the 1D solution (4.19) and the friction factor within, a numerical code was programmed in Fortran. Two friction models were implemented in the 1D laminar model, namely the quasi-steady friction model, and the Daily et al model with constant friction coefficient k_1. Furthermore, in the turbulent 1D model, three different friction models was considered and implemented in the code; that is, the quasi-steady friction model, the Daily et al. model with the Brunone friction coefficient, and the simplified weighting function friction model by Vardy et al. To model the steady friction factor the Darcy friction factor was calculated by solving the Colebrook-White equation implicitly.
A drawback when applying unsteady friction models to the 1D model (4.19) is that the influence of unsteady contributions of the friction factor only effects its own time step and the acceleration of the neighbouring time steps; when the unsteady component of the friction factor has diminished the unsteady solution will be the same as the one with quasi-steady modelling at the same time step. Unsteady friction contributions early in the transients will therefore not significantly effect the solution at a later time. This occurs because the solution is calculated from the initial condition and not from the previous time step.

However, when modelling the 1D model with the unsteady friction models, the unsteady friction is not only dependent upon current time step, but also the next and previous time steps, or all the previous time steps. Furthermore, in the unsteady friction models the local acceleration is needed, which is modelled in following way: The local acceleration in acceleration vector A at index i is found by

$$A(i) = \frac{U(i+1) - U(i-1)}{T(i+1) - T(i-1)}, \tag{4.28}$$

where U is the velocity vector and T is the time vector. A short explanation to how the different 1D models were implemented is found in the forthcoming sections.

4.5.1 1D Laminar Model with Quasi-Steady Friction Modelling

The quasi-steady 1D laminar model is modelled by solving

$$U(t) = \frac{\gamma}{-\kappa} + \left(U_0 + \frac{\gamma}{\kappa}\right) e^{\kappa t} \tag{4.27}$$

implicitly at each time step, where $\kappa = \frac{32}{\rho D^2}$ and $\gamma = -\frac{1}{\rho}\frac{dp}{dx}$; both κ and γ are constant. In the program-code a "do loop" solves the above equation at each time step until a pre-set parameter of tolerance is reached.

4.5.2 1D Laminar Model with IAB Friction Modelling

When modelling unsteady friction with the Daily et al. friction model, the Equation 4.27 is first implicitly solved at each time step with the quasi-steady friction factor. The resulting velocity vector is saved and the acceleration at every time step is calculated and then the unsteady friction component is calculated. The velocity is then updated by solving the Equation 4.27 with the updated value of κ. When the vector is traversed, the updated velocity is compared to the old, the process continues until a pre-set minimum average difference between the old and the updated velocity is reached.

4.5.3 1D Turbulence Quasi-Steady Friction Model

When the friction factor is modelled with the quasi-steady friction factor, the only information needed is the time and bulk velocity at the current time step. The Equation (4.19) was solved implicitly until the difference between right hand side and left hand side velocity was under a predetermined tolerance δ. Solving the equation implicitly renders the solution independent of the time step size. The implicit solver code is included below:

```
1  !Loop that traverses vectors
2  DO I=2,NSTEPS
3     Ut(I) = Ut(I-1)
4     UOLD = Ut(I)+1
5     !Loop that implicitly solves Ut(I)
6     DO WHILE  (ABS(Ut(I)-UOLD) > tol)
7        UOLD = Ut(I)
8        !Function that returns the Darcy friction factor
9        CALL FRICTION(Ut(I))
10       FS(I)=FRICT
11       BETA = FS(I)/2/D
12       !Integration constant
13       C = 1/SQRT(alpha*beta)*(ATANH(DCMPLX(Ut(1)*SQRT(beta/alpha),0)))
14       Ut(I) = SQRT(alpha/beta)*ABS(tanh(DCMPLX((sqrt(alpha*beta)*tVector
             (I)+c*SQRT(alpha*beta)))))
15    END DO
16    TAU(I) = (FS(I) * rho *UT(I)**2)/8
17    RET(I) = UT(I)*RHO*D/MU
18 END DO
```

4.5.4 1D Turbulence Daily et.al. Model with Brunone Unsteady Friction Coefficient

To model the unsteady friction, additional steps must be taken. A step by step outline of the procedure follows:

1. $U(i)$ is solved at each time step with the quasi-steady friction model and the velocity vector is saved.
2. The acceleration and unsteady component of the friction factor is calculated from the saved velocity vector.
3. The 1D model is solved with the newly found unsteady friction. The new velocity vector is compared to the old velocity vector and saved.
4. Step 2, and 3 are repeated until the average difference between the old and new velocity vector is below a pre-set tolerance.

4.5.5 1D Turbulence Vardy and Brown's Unsteady Friction Model

The algorithm is similar to the 1D turbulence Daily et al. friction model, however

1. $U(i)$ is solved at each time step with the quasi-steady friction model and the velocity vector is saved.
2. For $U(i)$ the weighting function and acceleration for all previous time steps are calculated, convoluted and numerically integrated using the trapezoid method.
3. The shear decay coefficient is calculated.
4. The unsteady component of the friction factor is estimated $f_u\left(W_a(\theta), \frac{\partial U}{\partial t}\right)$ and is used to update the value of $U(i-1)$
5. Step 2, 3, and 4 is repeated until the difference between $|U(i-1)_n - U(i-1)_{n-1}| < \delta$, where n is number of iteration of step 2, 3, and 4.

The numerical code in its totality is included in Appendix B.

Chapter 5

Computational Fluid Dynamics Model

In this thesis a commercial CFD program is to be used to simulate a detailed fully transient case which is to be compared to a more simple 1D model. There exist a number of different CFD programs available, among them are, ANSYS CFX, ANSYS Fluent, PHOENICS and STAR-CD. There are also open source alternatives, like the popular OpenFoam.

The CFD package chosen for this thesis is ANSYS Fluent 13. Recently, Fluent was bought by ANSYS and subsequently brought under their Workbench solution. ANSYS Workbench is a complete CFD package, delivering a geometric modeller, mesh generator, CFD solvers, and a result analysis program.

There are several ways to find the deficiencies of a gas transport model. Executing experiments on the actual pipe-line and comparing them with the computational model is a very expensive way of doing it, halting effective deliverance. A cheaper way is to go to numerical methods and inspect the validity of dubious simplifications, like the quasi-steady friction factor during transient periods, by comparing the model or similar models with a detailed fully transient model. The scope of this work is to see the potential deviance from a quasi-steady friction-based one-dimensional model to a more advanced fully transient two-dimensional model. To simplify notation, the bar over the mean local velocity is omitted from this point on; i.e. $\bar{u} \Rightarrow u$.

5.1 Finite Volume Method

Fluent, as many other CFD programs, uses the finite volume method (FVM). FVMs are robust and numerically cheap for conservation laws. They can be used for all geometries, using both structured and unstructured meshes. However, achieving high precision can be difficult compared to other methods. The finite volume

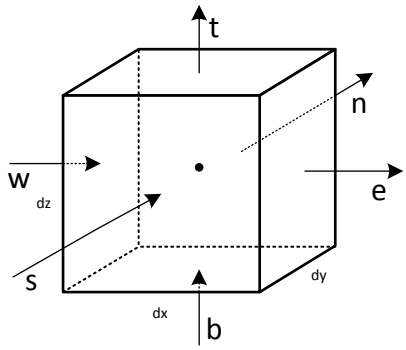

Figure 5.1: A 3D control Volume.

method can be decomposed into three main steps:

1. Discretisation of the solution domain into a suitable grid
2. Discretisation of the transport equations into a set of algebraic equations
3. Solving the discretised equations

An outline of these steps are given in the forthcoming sections.

5.1.1 Discretisation of the Solution Domain

One big asset of the FVM is that there is no limit to the shape of the discretised domain, grid, and the discrete control volumes, cells, which constitute the discretised domain. However, guidelines to generate grids to achieve high accuracy solutions exists. For instance, the grid should follow the stream lines, higher resolution is recommended where high velocity gradients are expected, the grid aspect ratio and expansion ratio should not be too great, where the expansion ratio the cells increase in size compared to neighbouring cells, while the aspect ratio is the ratio between the two cell walls in a cell.

The grids can be either be orthogonal or non-orthogonal, and structured or non-structured. The grids are orthogonal if and only if all the cells are orthogonal at the intersections; the grids are structured if and only if it is possible to make a N-dimensional array indexing the grid, where N is the spatial dimension of the domain.

The shape of the cells are often quadrilateral or triangular. Commonly, cells have a node at its center where the pressure is calculated, and the faces of the cells

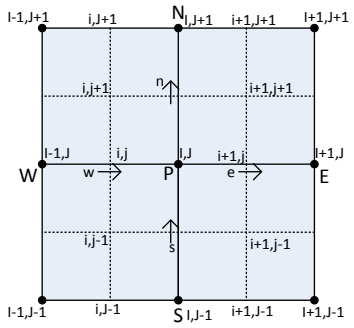

Figure 5.2: A 2D staggered grid.

are identified by their cardinal directions, n,s,w, and e, relative to the cell center. Neighbouring cell nodal points are identified by capital letters; e.g. N, S, W, and E. If the domain is three-dimensional, the fifth and sixth faces are identified by bottom (b) and top (t), see Figure 5.1, where a 3D orthogonal quadrilateral cell is shown. In addition, to increase stability of the solvers when treating convective flows, where the velocity field and pressure field must be coupled, a staggered grid is applied. In the staggered grid the velocity field is stored at the faces of the cells while other variables like the pressure and temperature are stored at the cell nodes, see Figure 5.2. Furthermore, the indexing of cell-nodes and face-intersection (vertex) in a staggered grid is with capital I and J, and with lower case i and j for cell-nodes and face-intersections respectively.

5.1.2 Discretisation of the Transport Equations

In FVMs the governing equations are written on the same form, known as the transport equation. If a general variable ϕ is introduced, the conservative form of the governing equations, in addition to equations for scalar quantities like temperature and turbulence kinetic energy, can conveniently be written as

$$\frac{\partial \rho\phi}{\partial t} + \frac{\partial \left(\rho\phi u_i\right)}{\partial x_i} = \frac{\partial}{\partial x_i}\left[\Gamma \frac{\partial \phi}{\partial x_i}\right] + S_\phi, \tag{5.1}$$

where Γ is a diffusion coefficient and S_ϕ is a source term. If the transport equation is to generate the governing equations for compressible viscous flow, ϕ is set to $1, u, v, w$, and $c_v T$, additionally, Γ and S_ϕ must be set to the appropriate values to satisfy the equations.

Furthermore in finite volume methods, the transport equations are integrated over a control volume CV; if the problem is time-dependent, the transport equation

is also integrated over time, from t to $t+\Delta t$, thus the integrated general transport equation becomes

$$\begin{aligned}\int_t^{t+\Delta t}\int_{CV}\frac{\partial \rho\phi}{\partial t}\,dV\,dt+\int_t^{t+\Delta t}\int_{CV}\frac{\partial\left(\rho\phi u_i\right)}{\partial x_i}\,dV\,dt\\ =\int_t^{t+\Delta t}\int_{CV}\frac{\partial}{\partial x_i}\left[\Gamma\frac{\partial\phi}{\partial x_i}\right]dV\,dt+\int_t^{t+\Delta t}\int_{CV}S_\phi\,dV\,dt\,.\end{aligned} \tag{5.2}$$

By applying the divergence theorem and change the order of the integration and differentiation in the temporal term, the general integrated form of the transport equation is

$$\begin{aligned}\int_t^{t+\Delta t}\frac{\partial}{\partial t}\left[\int_{CV}\rho\phi\,dV\right]dt+\int_t^{t+\Delta t}\left[\int_A\left(\rho\phi u_i\right)dA_i\right]dt\\ =\int_t^{t+\Delta t}\left[\int_A\left(\Gamma\frac{\partial\phi}{\partial x_j}\right)dA_i\right]dt+\int_t^{t+\Delta t}\int_{cv}S_\phi\,dV\,dt\end{aligned} \tag{5.3}$$

where dA_i is the face area in i direction.

The general integrated transport equation can yield a discretised equation in a cell at its nodal point P and its faces. Now for simplicity, consider a one-dimensional steady diffusion problem for the scalar variable ϕ; the integrated transport equation is in that case

$$\int_A\left(\Gamma\frac{\partial\phi}{\partial x}\right)dA+\int_{CV}S_\phi\,dV=0, \tag{5.4}$$

where A is the cross-sectional area of the east or west face depending on the integration limit. The diffusive term is evaluated at the east and west face and the source term is averaged over the control volume, yielding

$$\left[\Gamma A\frac{\partial\phi}{\partial x}\right]_e-\left[\Gamma A\frac{\partial\phi}{\partial x}\right]_w+\overline{S_\phi}\Delta V=0. \tag{5.5}$$

The diffusion coefficient and the gradient of ϕ is required at the east and west faces. A common practice in FVM is that the scalar variable and the diffusion coefficient are evaluated at the nodal points in accordance with a staggered grid. There are several ways to approximate the diffusion coefficient at the faces. The most straight forward method is to evaluate them by linear interpolation; i.e for a equidistant grid:

$$\begin{aligned}\Gamma_e&=\frac{\Gamma_E+\Gamma_P}{2}\\ \Gamma_w&=\frac{\Gamma_P+\Gamma_W}{2}.\end{aligned} \tag{5.6}$$

The gradient of the scalar variable, $\frac{\partial \phi}{\partial x}$, is approximated by the following equations:

$$\begin{aligned} \left(\frac{\partial \phi}{\partial x}\right)_e &= \frac{\phi_E - \phi_P}{\Delta x_{PE}}, \\ \left(\frac{\partial \phi}{\partial x}\right)_w &= \frac{\phi_P - \phi_W}{\Delta x_{WP}}. \end{aligned} \tag{5.7}$$

Substituting equations (5.6) and (5.7) into Equation (5.5) gives

$$\Gamma_e A_e \left(\frac{\phi_E - \phi_P}{\Delta x_{PE}}\right) - \Gamma_w A_w \left(\frac{\phi_P - \phi_W}{\Delta x_{WP}}\right). \tag{5.8}$$

This is rearranged to

$$\left(\frac{\Gamma_e}{\Delta x_{PE}} A_e + \frac{\Gamma_w}{\Delta x_{WP}} A_w\right) \phi_P = \left(\frac{\Gamma_w}{\Delta x_{WP}} A_w\right) \phi_W + \left(\frac{\Gamma_e}{\Delta x_{PE}} A_e\right) \phi_E. \tag{5.9}$$

Now the coefficients of ϕ_P, ϕ_W, and ϕ_E are identified to a_P, a_W, and a_E yielding

$$a_P \phi_P = a_W \phi_W + a_E \phi_E + S_\phi, \tag{5.10}$$

which is a discrete algebraic equation for the 1D diffusion problem for the cell control volume.

5.1.3 Solving the Discrete Equations

With a whole mesh of cells, algebraic equations e.g. Equation 5.10 is associated with each cell and constitutes a system of linear algebraic equations. Cells which are adjacent to boundary conditions must incorporate these in the algebraic equations. The system of algebraic equations can be solved by any appropriate matrix solution technique, thus yielding a distribution of the flow property ϕ.

5.2 Choice of Turbulent Model

There are many different turbulent models with different accuracy, complexity, and computer cost. A hierarchy outlining the different models according to complexity is depicted in Figure 5.3. Choosing a model depend on the physical problem which is to be modelled, wanted accuracy, and computational power at disposal.

The physical problem is simplified so that it is feasible to do the simulations on a personal computer. The fluid flow is assumed to be isothermal, incompressible, fully developed, and with constant viscosity. To avoid simulating in a long pipe to achieve fully developed flow, translational periodic boundary conditions were set on the inlet and outlet, this is explained in detail in Section 5.4.1. Furthermore, the pipe is assumed to have constant diameter. Generally, a turbulent pipe flow is three-dimensional, but since there is no reason to assume swirl flow inside the pipe, the flow can be modelled as an axis symmetric problem, reducing it to a two-dimensional flow. In gas transport flow, Reynolds numbers up to $\sim 10^7$ are

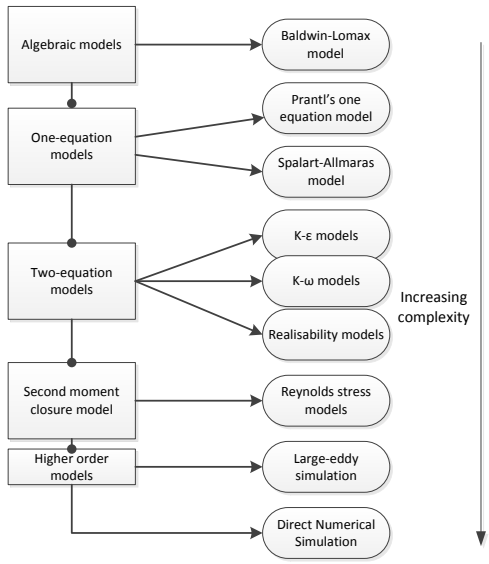

Figure 5.3: Hierarchy of turbulence models[33]

expected, so the model must be able to solve for high Reynolds numbers. The area of interest to evaluate the friction factor is the viscous sublayer; this means that the chosen model must have high accuracy near the wall. These models are known as low Reynolds number models, since the local Reynolds number, $Re_y = \frac{\rho \overline{u} y}{\mu}$, goes towards zero near the wall.

Direct numerical simulations and large eddy simulations are not feasible model alternatives due to the high Reynolds number. Therefore, only Reynolds averaged models will be considered. The usable turbulent models which are present in Fluent are given below with short descriptions. If nothing else is specified, the information is from the Fluent theory guide[3].

5.2.1 The Spalart-Allmaras Model

The Spalart-Allmaras model is a one-equation model, solving a modelled transport equation for the kinematic eddy viscosity. The model was designed for aerospace applications involving wall-bounded flows. It is a low Reynolds number model, requiring high wall resolution $y^+ \sim 1$. The Spalart-Allmaras model is not calibrated for general industrial flows and lacks sensitivity to rapidly changing flows. It is also the simplest of the presented models, making it a numerically cheap model with low accuracy.

5.2.2 The k-ϵ Model

The k-ϵ model is a popular choice for practical engineering flow simulations. It possess a good combination of robustness, computer cost, and reasonable accuracy for a wide range of turbulent flows. The model is based on the transport equations for turbulent kinetic energy k and its dissipation rate ϵ. The kinetic energy model equation is derived from the exact equation, while the ϵ model equation is obtained from physical reasoning. The model is only valid for fully turbulent flows. There are several improved sub-models improving the known weaknesses. Two of them are included in Fluent, the RNG k-ϵ model and the Realizable k-ϵ. The standard k-ϵ model is a high Reynolds model, relaying on wall functions near the wall. The RNG k-ϵ has a differential formula for effective viscosity which accounts for low-Reynolds number effects. Its effectiveness depend on appropriate near-wall treatment.

5.2.3 The k-ω Model

The k-ω model in Fluent is based on the Wilcox k-ω model. It can be modified with respect to compressibility, low Reynolds number effects, and shear flow spreading. It is sensitive to the values of k and ω outside the shear layer. The k-ω model is an empirical model which is based upon model transport equation for turbulent kinetic energy k and the specific dissipation rate ω, where ω can be seen as a ratio between ϵ and k. The k-ω model demonstrates higher accuracy than the k-ϵ model with respect to the turbulent boundary layer. With viscous correction added to the k-ω model it produces almost identical results with measured skin friction coefficient in Wilcox article[35], indicating an accurate solution in the near wall region. There is also a Shear-Stress Transport (SST) k-ω model. This model is better for free stream flows, using k-ω in the boundary layer and the ϵ in the free stream region.

5.2.4 The Transition k-kl-ω Model and Transition SST Model

As the model names implies, they are transition models. They are used to predict boundary layer development and calculate transition onset.

5.2.5 The Reynolds Stress Model

The Reynolds stress model is the most elaborate RANS turbulence model in Fluent. In two-dimensional flows, five additional transport equations are solved. This leads to high computational cost. The model is best utilized for cyclone flows, highly swirling flows in combustions, rotating flow passages, and stress induced secondary flows in ducts.

5.2.6 Conclusion

The choice of model depends mostly on a balance between boundary-layer accuracy, computer cost and general accuracy. Getting all in one model is not possible, but as a compromise the standard k-ω model with low Reynolds treatment is a good choice. As an alternative the RNG k-ϵ model could be mentioned, but it is

not as stable in near wall regions, which might cause problems during transient simulations.

5.3 The k-ω Model

As mentioned above, the k-ω model is a two-equation model. As most one- and two-equation models, it is based upon modelled transport equations for turbulent kinetic energy k and turbulent frequency ω, where the turbulent frequency is a relation between turbulent dissipation and turbulent kinetic energy

$$\omega \propto \frac{\epsilon}{k}.$$

The k-ω models the Reynolds stress tensor with the Boussinesq approximation,

$$\tau_{ij} = -\rho\overline{u_i' u_j'} = 2\mu_t S_{ij} - \frac{2}{3}\rho k \delta_{ij}, \tag{5.11}$$

where S_{ij} is the mean strain rate tensor and μ_t is the eddy viscosity. The turbulent kinetic energy k is expressed as

$$k = \frac{1}{2}\overline{u_i' u_i'}.$$

The eddy viscosity is given by

$$\mu_t = \alpha^* \frac{\rho k}{\omega}. \tag{5.12}$$

The rate of change in turbulent kinetic energy is an exact equation, while the rate of change of specific dissipation rate ω is derived with the help of dimensional analysis and empirical relations. The transport equations for k and ω are defined in [3] as:

The Turbulence Kinetic Energy Transport Equation

$$\frac{\partial \rho k}{\partial t} + \frac{\partial k \rho u_i}{\partial x_i} = \frac{\partial}{\partial x_j}\left[\left(\mu + \frac{\mu_t}{\sigma_k}\right)\frac{\partial k}{\partial x_j}\right] + G_k - Y_k + S_k, \tag{5.13}$$

The Specific Dissipation Rate Transport Equation

$$\frac{\partial \rho \omega}{\partial t} + \frac{\partial \omega \rho u_i}{\partial x_i} = \frac{\partial}{\partial x_j}\left[\left(\mu + \frac{\mu_t}{\sigma_\omega}\right)\frac{\partial \omega}{\partial x_j}\right] + G_\omega - Y_\omega + S_\omega, \tag{5.14}$$

where σ_k and σ_ω are the Prandtl numbers for k and ω respectively. The terms inside the square brackets in both equations are the effective diffusivity, (Γ), for turbulent kinetic energy and specific dissipation rate. G_k and G_ω represent the generation of k and ω. Potential sources are described by the source terms S_k and S_ω. The constants in the equations will be summarized in Section 5.3.4.

5.3.1 Turbulence Production

The production of turbulent energy and ω represented by G_k and G_ω. G_k is given by

$$G_k = -\rho\overline{u_i' u_j'}\frac{\partial u_j}{\partial x_i} \tag{5.15}$$

remembering and evaluating the Boussinesq approximation (5.11) we get

$$G_k = \mu_t S^2 \tag{5.16}$$

The production of ω is

$$G_\omega = \alpha\frac{\omega}{k}G_k, \tag{5.17}$$

where α is defined as

$$\alpha = \frac{\alpha_\infty}{\alpha^*}\left[\frac{\alpha_o + Re_t/R_\omega}{1 + Re_t/R_\omega}\right], \tag{5.18}$$

and the turbulent Reynolds number is

$$Re_t = \frac{\rho k}{\mu\omega}. \tag{5.19}$$

5.3.2 Turbulence Dissipation

The dissipation of k is given by

$$Y_k = \rho\beta^* f_{\beta^*} k\omega, \tag{5.20}$$

where

$$f_{\beta^*} = \begin{cases} 1 & \text{if } \chi_k \leq 0 \\ \frac{1+680\chi_k^2}{1+400\chi_k^2} & \text{if } \chi_k > 0 \end{cases},$$

and where

$$\chi_k = \frac{1}{\omega^3}\frac{\partial k}{\partial x_j}\frac{\partial \omega}{\partial x_j}$$

The dissipation of ω is defined as

$$Y_\omega = \rho\beta f_\beta \omega \tag{5.21}$$

where

$$f_{\beta^*} = \frac{1 + 70\chi_\omega}{1 + 80\chi_\omega}$$

and

$$\chi_\omega = \left|\frac{\Omega_{ij}\Omega_{jk}S_{ki}}{(\beta_\infty^*\omega)^3}\right|$$

$$\Omega_{ij} = \frac{1}{2}\left(\frac{\partial u_i}{\partial x_j} - \frac{\partial u_j}{\partial x_i}\right)$$

S is the strain rate tensor

$$S_{ij} = \frac{1}{2}\left(\frac{\partial u_i}{\partial x_j} + \frac{\partial u_j}{\partial x_i}\right)$$

5.3.3 Low-Reynolds-Number Correction

The coefficient α^* in equation (5.12), is used to dampen turbulent viscosity causing a low Reynolds number correction. It is defined as

$$\alpha^* = \alpha^*_\infty \left[\frac{\alpha^*_0 + Re_t/R_k}{1 + Re_t/R_k} \right] \tag{5.22}$$

where Re_t is defined in equation (5.19).

5.3.4 Model Constants

The model's constants have been altered along the years to optimize accuracy. The standard constants in Fluent are as follows

$$\alpha^*_\infty = 1, \quad \alpha_\infty = 0.52, \quad \alpha_0 = 1/9 \quad \beta^*_\infty = 0.09, \quad \beta_i = 0.072, \quad R_\beta = 8, \tag{5.23}$$

$$R_k = 6, \quad R_\omega = 2.95, \quad \zeta^* = 1.5, \quad \sigma_k = 2, \quad \sigma_\omega = 2. \tag{5.24}$$

5.3.5 Wall treatment

There are two different approaches to model the near-wall region. The first method is to calculate the value of the first node from the wall with the help of a wall function. The wall functions are semi empirical functions and enable the use of models that do not include wall turbulent effects with wall bounded flows. The other way is to resolve the whole viscous sublayer. This is only sensible to do with a turbulence model accounting for viscous-affected regions; i.e. low Reynolds number models. The two methods are illustrated in Figure 5.4.

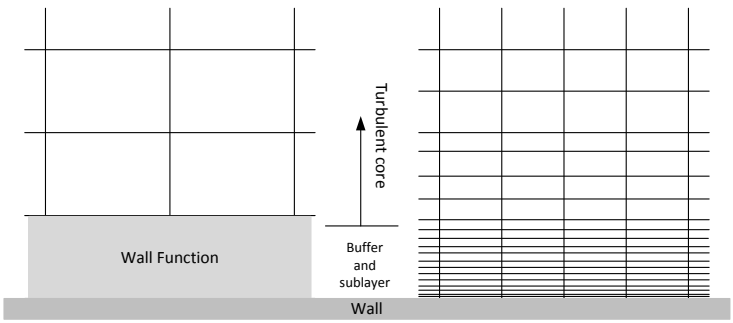

Figure 5.4: Wall function versus near-wall model approach.

In the k-ω model in Fluent the default wall treatment is the so called enhanced wall treatment (EWT). With the enhanced wall treatment the user does not need to select which of the two approaches to use. It is a combination of the law of the

wall(2.18) and the log law of the wall(2.19). Combining the two velocity contributions with a blending function yields

$$u^+ = e^{\Gamma} u^+_{lam} + e^{1/\Gamma} u^+_{turb} \tag{5.25}$$

where the blending function is

$$\Gamma = -\frac{a(y^+)^4}{1 + by^+}, \tag{5.26}$$

in which the constants are $a = 0.01$ and $b = 5$. For $y^+ < 3$ the enhanced wall treatment ensures that dimensionless velocity is approximately equal to the laminar value $u^+ \approx u^+_{lam}$, and for $y^+ > 30 \Rightarrow u^+ \approx u^+_{turb}$. It should also give reasonable results in the wall buffer region. But it is advisable to either keep $y^+ > 30$ or $y^+ < 3$; preferably around 1.

5.4 Boundary and Initial Conditions

To simulate an accurate solution, correct boundary conditions are essential. There are four boundaries that needs to be set in the domain. The boundary conditions are illustrated in Figure 5.5

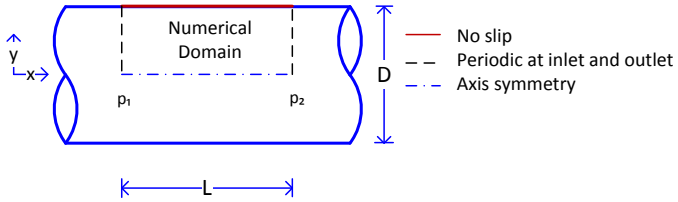

Figure 5.5: Bondary conditions for a pipe segment

5.4.1 Periodic Boundary Conditions

To simulate fully developed turbulent pipe flow, a certain entrance length is needed. The entrance length can be approximated as $L \approx DRe_D^{1/6}$[34]. This means that the pipe length must be $65D$ at $Re \sim 10^7$. In addition to this, the pipe must be even longer for a time dependent flow. Simulating a fully developed flow is still possible using periodic boundary conditions at inlet and outlet. This means that the flow exiting the pipe segment enters the entrance with the same characteristics. This makes the pipe, in essence, infinite in length. A pressure difference between the two periodic boundaries is set to drive the flow at a wanted bulk-velocity.

There are some limitations when periodic boundary conditions are applied. The flow cannot be compressible since this might interfere with the conservation of

mass in the segment, if the density changes along the pipe. Additionally, sources of any kind will violate the conservation laws and therefore all source terms must be zero[4].

5.4.2 Axis boundary condition

The flow is symmetric about the axis, meaning that the domain can be halved by setting the axial plane as an axis symmetry boundary condition. A Symmetry boundary condition functions as a mirror simulating the presence of the other half of the flow.

5.4.3 Wall boundary condition

At the pipe wall the normal no-slip condition is used, with the possibility of adding finite roughness. With the no-slip condition the velocity is zero at the wall. In Fluent, the roughness height is modelled as a sand-grain roughness height. To achieve similar roughness as found in industrial pipes, a roughness constant, C_s is added. However, no clear guidance to find an appropriate roughness constant exists, and consequently the roughness constant was left unchanged in the Fluent simulations.

5.4.4 Initial Conditions

In the k-ω the initial conditions of k and ω must be set at the inlet. The value can be estimated by Fluent via choice of turbulent intensity and hydraulic diameter. If $\omega \to 0 \Rightarrow \mu_t \to \infty$, thus non-zero values of ω must be chosen. The value of k is less important. Typical values for k and ω at the inlet calculated by Fluent from the turbulence intensity and the diameter was $k = 1.5 \cdot 10^{-4}$ and $\omega 0.32$ $Re = 10^6$ when $Re = 10^7$.

5.5 Mesh

In general the accuracy of a CFD solution is governed by the mesh resolution. With higher resolution comes higher accuracy but also higher computational cost. To optimize the grid with respect to both accuracy and computational cost one can use a non-uniform grid with higher resolution where large variations occur[32]. For pipe flow the biggest gradients will occur near the wall due to the no-slip condition. When using FVMs it is possible to use an unstructured mesh which is denser near the wall. This might be a good strategy for many problems, but with periodic inlet and outlet, and high Reynolds number flow, this can lead to inaccuracy for the mass flux, making the solution diverge. Using a structured mesh with increasing resolution near the wall is then a better alternative. As a rule of thumb the increased size between the cells should not increase with more than a factor of 1.2 per step away from the wall. furthermore, the viscous sublayer should be covered by at least 15 layers of cells[3]. Near the wall there can be quite

elongated cells without deteriorating the accuracy as long as the elongation is in the streamwise direction; albeit generally, very elongated cells should be avoided. Figure 5.6 depicts the first cell from the wall with vertex, node and edges pointed out. To achieve the wanted $y^+ \sim 1$ value near the wall, the first node becomes very small. With Reynolds number $\sim 10^7$ and a diameter of 1m, the distance from the wall to the first node is determined by

$$y = \frac{\mu y^+}{\sqrt{\rho \tau}}$$

Inserting the numbers and evaluating the wall shear stress using equation (2.30), we get that $y = 3.14 \cdot 10^{-6}$m; a distance which one by definition must use a microscope to observe. In an incompressible periodic flow, the velocity does not change in the

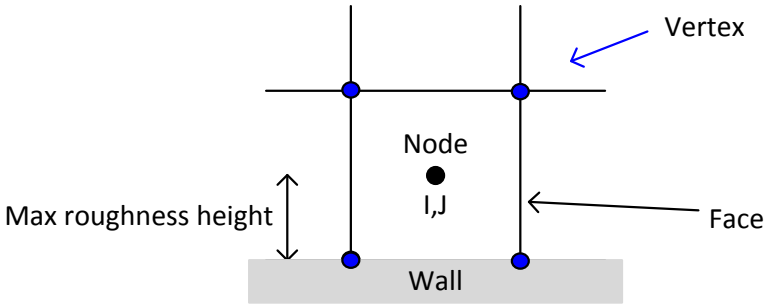

Figure 5.6: First cell from the wall

axial direction, meaning that the length of the mesh in axial direction can be very short without losing information. This greatly lessens the numerical domain and then also the computational cost. For a pipe with finite roughness height, the first node cannot be closer than the roughness height; this will lead to unphysical behaviour.

5.5.1 Mesh Generation

To generate a mesh, a geometric figure depicting the domain is made, then the figure is meshed using ANSYS Meshing. In this case the geometric shape is just a flat face the height of $D/2$ with an appropriate length. There are several ways to mesh the domain. Since this is a simple geometry, meshing it with quadrilateral orthogonal structured grid seems appropriate. In ANSYS Mesher this can be done by giving the face surface a function called "Mapped Face Meshing" and using "sizing functions" on the domain edges. To get a denser mesh near the wall, bias can be added to the radial edges. The inputs in the sizing function are number of cells, total expansion rate biggest cell over smallest cell. To calculate the first

node, height and expansion rate, an external program may be used (guessing is also possible). The external program MeshSpace is devised by Marcus Hartinger at Imperial College. The inputs can be edge length, expansion rate, and first node height, it will then return the bias factor and the number of cells required to achieve the input criteria. Figure 5.7 shows an example of two meshes with same first node distance, but with different expansion factor.

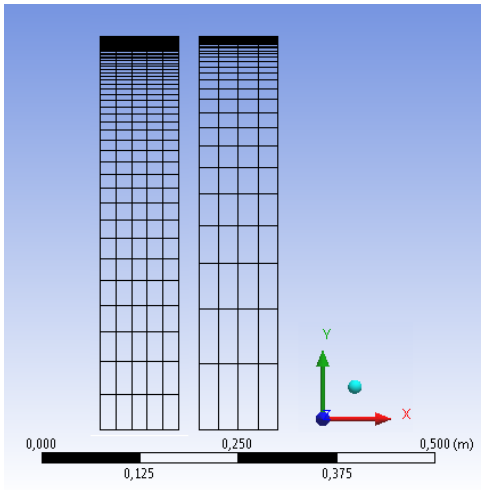

Figure 5.7: Two meshes with different expansion rate k for $Re \sim 10^7$. Left: $k = 1.1$ and $n = 80$. Right: $k = 1.2$ and $n = 54$.

5.6 Mesh and Time Independent Solution

A solution is considered mesh and time independent when a substantial increase of mesh and time resolution give no or negligible alteration of the solution. To avoid unnecessarily high resolution in space it is common to start solving with a coarse mesh resolution and increase the resolution until the solution converges. To avoid making too many refinements and simulations it is advisable to "search" for the correct mesh according to binary search or similar. When a sufficient mesh is found, the mesh can be used to find an appropriate time step in a similar manner as for the mesh. It can be noted that the mesh must be tested for the highest Reynolds number to be used in the transient case.

5.7 CFD Solvers

There are two flow solvers, the pressure based solver and the density based solver. The density based solver is designed to solve compressible flows and flow with shock, and the pressure based solver was derived for incompressible flow, but can

work for a wide range of flows. Since the flow that is to be solved is incompressible, it is natural to use the pressure based solver.

To couple pressure and velocity there are several methods, in Fluent the choices are between four schemes. Three segregated methods SIMPLE, SIMPLEC, and PISO and a coupled method named Coupled. The segregated methods solve the governing equations for each solution variable u, v, p, k and ω one after another. The next step is solving the pressure correction continuity equation. In the coupled algorithm all governing equations and pressure correction is solved simultaneously. The segregated solver needs less memory but commonly uses more iterations to converge. The coupled algorithms are not considered to be good choices due to the limited memory available in the computer at disposal. SIMPLE is an acronym for Semi-Implicit Method for Pressure Linked Equations and is a widely used method and it is also the default in Fluent. SIMPLEC (SIMPLE-Consistent) has an increased under relaxation factor that can be applied to obtain faster convergence for flows where the pressure coupling is the limiting factor for convergence. If not, the SIMPLE and SIMPLEC will yield similar convergence rate. PISO (Pressure Implicit with Splitting of Operators) is a pressure-velocity calculating method first made for non-iterative computation for transient compressible flows. It has been altered to function for iterative methods as well. It is similar to SIMPLE with an extra correction step. It is a good method for transient flows since it allows for larger time steps and, in addition, the Non Iterative Time Advancement (NITA) can be applied. When NITA is activated the computational cost is further reduced.

The flow considered in this thesis do not contain the convection term, which tends to give rise to stability issues regarding the pressure velocity coupling. Therefore, the SIMPLEC scheme will have no advantage over the SIMPLE algorithm, thus the SIMPLE method was used in the steady state simulation, and the PISO method was applied in the transient simulations with the NITA scheme activated when possible.

5.7.1 Spatial and Time Discretisation

There are several spatial discretisation methods for the momentum, k, and ω equations. The methods available in Fluent are the first order and second order upwind, the power law, QUICK, and the third order MUSCLE. First order is mostly used for an initial solution since it tends to give faster converging solution and has low accuracy. The QUICK and third order MUSCLE can give higher accuracy than the second order upwind scheme for rotating or swirling flows. In other flows the second order upwind discretisation is sufficient, and the QUICK and MUSCLE schemes have no special advantage. The power law has similar accuracy as the first order upwind.

For the spatial discretisation in the simulations the second order upwind discretisation was used, as the simulated flow neither contains rotating or swirling flow.

Time discretisation schemes in Fluent are the first order implicit, the second order implicit and the bounded second order implicit. Bounded second order and second order implicit yield the same accuracy, but the bounded second order gives

Table 5.1: Fluent settings.

	Steady Simulations	Transient Simulations
Solver	SIMPLE	PISO
Gradient	Least squares cell based	Least squares cell based
Pressure	Standard	Standard
Momentum	Second order upwind	Second order upwind
Turbulent Kinetic Energy	Second order upwind	Second order upwind
Specific Dissipation Rate	Second order upwind	Second order upwind
Temporal Discretisation		Second order implicit

extra stability. For the time discretisation the second order implicit method was applied, as the stability was not anticipated to cause problems.

5.8 Fluent Settings

A summary of the Fluent settings used in the simulations are presented in this Section.

The k-ω turbulent model was chosen with the low Reynolds correction and the default model constants were used (5.24) in all simulations. The pressure based solver was selected. The settings are conveniently summarised in Table 5.1.

The NITA scheme was used in the transient simulations when possible, this to save time. However, when the flow was decelerating it was proven to be quite unstable and tended to diverge unless very short time steps were chosen. In those cases, PISO with enough iteration per time step to achieve convergence was selected.

5.8.1 Physical Domain

In all of the simulations an axis-symmetric two-dimensional plane of the upper part of a 1 m or 0.1 m diameter pipe was used. The pipe length may vary without altering the solution[16].

The fluid chosen was water, with properties given from ocean level pressure at 15°C, see table 5.2.

Table 5.2: Fluid Properties

Property	*Value*
Viscosity, μ	$1.003 \cdot 10^{-3}$ m^2/s
Density, ρ	998.2 kg/m^3

5.9 Start Solution for the Transient Simulations

Before a solution can be initiated, an initial condition guess must be given. If the initial guess is zero velocity and only the values for k and ω are given, the solution

will converge towards a steady solution for the given pressure difference set at the translational periodic boundary condition. This is a common way of finding a fully developed steady flow without the need of a big numerical domain. The obtained steady solutions was used as a starting solution for the transient cases. It is important that the initial solution is well within the turbulent domain when using the k-ω model, since it is fundamentally developed for turbulent flow and, thus, is poor at determining transition between laminar and turbulent flow.

To get the wanted Reynolds number in the steady start solution, the correct pressure difference must be set. The pressure difference was found from equation (2.27),

$$\frac{dp}{dx} = -f\frac{(\mu Re)^2}{2\rho D^3},$$

where the Darcy friction factor is calculated from the Colebrook-White formula (2.40).

Chapter 6

Validation of the k-ω Model

Validation of a CFD model is the process of determining to which degree a model accurately represents the real world from the perspective of the intended uses of the model [2]. The process can be described by several sub-processes, these are: examining iterative convergence, check for consistency in the solution, examine grid convergence, examine time convergence for time dependent simulations, compare results to experimental data or theoretical analysis, and finally to examine model uncertainties via running a number of simulations with different models and examining the result. The focus of the validation of the k-ω model will be on the spatial convergence, on the time convergence, and on comparing stationary results with 1D stationary analysis. The latter of the validation sub-processes has not been considered as it is out of the scope of the thesis.

The terms uncertainty and error are often used interchangeably in CFD-studies, however according to the American Institute of Aeronautics and Astronautic (AIAA) [2] there are clear distinctions between the two terms; uncertainty is the potential deficiency in any phase or activity of modelling process that is due to lack of knowledge, whereas error is defined as recognizable deficiency in any phase or activity of modelling and simulation.

6.1 Iterative Convergence

Iterative convergence was checked by monitoring the respective imbalance of the linear discretised equations, known as the residuals, and mean flow characteristics during iterative solving. Convergence is achieved if the residuals converge towards zero and the mean flow characteristics converge to a steady value. The solution converged monotonically with increasing iterations in all test cases. When the residuals became below a certain value, $\sim 10^{-4}$, monitored flow characteristics, such as the mass flow, was converged to its steady state.

6.2 Consistency

The discrete equations of the CFD model should converge to the differential equations for $\Delta t \to 0$ and $\Delta x \to 0$. Consistency can thus be seen as a reflection of the behaviour of the error; if the error reduces with increased spatial resolution and decreased time step size, the procedure is consistent. This is shown in the two next sections 6.3 and 6.4.

6.3 Mesh Independence

To generate reliable data from the simulations it is important that the solution is mesh independent. For the selected CFD model there are mesh requirements with regards to the first node near the wall; if the wall function is to be used the y^+ value should be above 30, if the viscous sublayer is to be resolved the y^+ value should be in the order of 1. The simulations in this thesis the viscous sublayer is resolved i.e the first node y^+ value should not be higher than ~ 1.

The mesh can be refined both in axial and radial direction, however the number of cells in axial direction did not affect the solution other than increasing the amount of iterations required for the solution to converge. To find adequate mesh resolution in the radial direction, a mesh with relative high expansion rate e.g. $k = 1.3$ was adapted to obtain a y^+ value of ≈ 1 when simulating a flow with the highest Reynolds number occurring in the transient. Furthermore, the expansion factor was decreased, while keeping the first node y^+. When a decrease in the expansion factor yielded no or little difference to the velocity profile, the mesh solution may be regarded as mesh independent

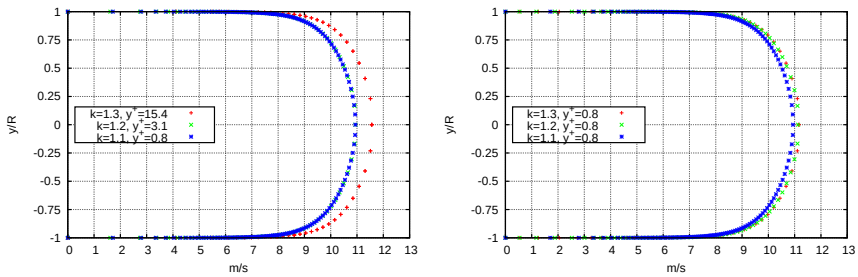

(a) Varying the closest to the wall node y^+ value

(b) Closest node to the wall is constant, expansion rate k is changed.

Figure 6.1: Different velocity profiles due to different mesh resolution. The boundary conditions are the same and results in a Reynolds number of $\sim 10^7$. Here k is the cell to cell expansion rate

In figure 6.1 different solutions obtained from different meshes with same boundary and initial conditions are shown. All the meshes with an y^+ value below 5 gives very similar profiles. With a cell to cell expansion factor of 1.3, cell close to the

axis will be very elongated and coarse in radial direction which is not advised [4]. With an expansion factor of 1.1 the number of cells is significantly increased, and thus the computational time is increased.

The meshes used in the turbulent transient simulations has a cell to cell expansion rate of 1.2 and 1.1 for the transients up to $Re = 10^6$ and $Re = 10^7$ respectively.

6.4 Time Step Independence

To ensure high accuracy results from the transient simulations it is crucial that the simulated transients are independent with regards to the chosen time step size and that the solution is converged at each time step.

To achieve time step independent simulations, several test simulations of the beginning of the transients was conducted. In the first simulation a presumed suitable time step size was chosen. The best way to be certain of an converged solution at each time step, in the authors opinion, is to control the convergence by iterating the solver until the residuals are below a predetermined set criteria, e.g $> 10^5$. In the next simulation the time step size was halved and the then the simulations were compared, see Figure 6.2

This procedure was repeated for all the transient cases with different start and end Reynolds number.

From figures 6.2a and 6.2b it can be concluded that it is important to ensure that the solution is converged at each time step before reducing the time step size.

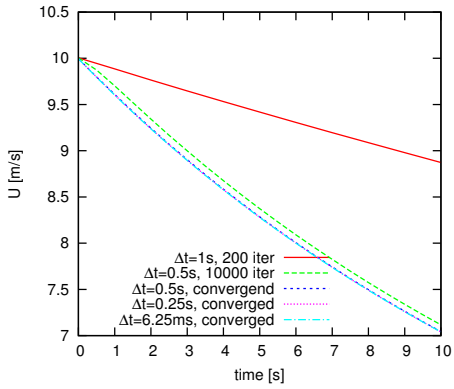

(a) Bulk Velocity

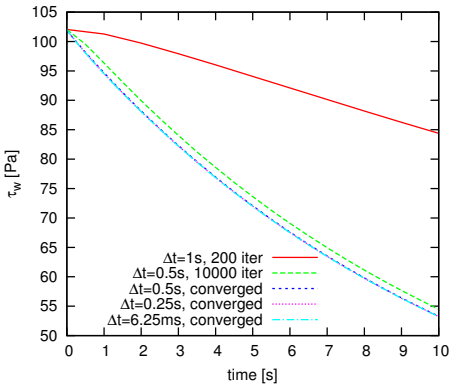

(b) Wall shear stress.

Figure 6.2: Decreasing time step size and increasing number of iterations per time step for transient from $Re_0 = 10^7$ to $Re_1 = 2 \cdot 10^4$.

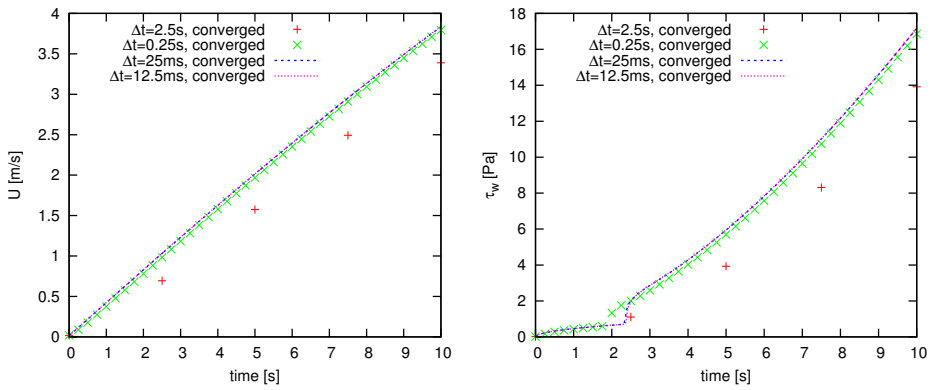

(a) Bulk Velocity

(b) Wall shear stress.

Figure 6.3: Decreasing time step size for transient from $Re_0 = 2 \cdot 10^4$ to $Re_1 = 10^7$.

6.5 Comparing the k-ω Model to 1D Theory

So far the focus has been to obtain reliable solutions with respect to the solver's consistency and convergence. Now attention is paid to the uncertainties of the 2D model compared to the "real" world. The geometry and boundary conditions at hand were chosen to be simple so that it would be possible to compare the transient 2D results to simple 1D models based on the analytic solution of the problem. Consequently, it is possible to compare stationary 2D k-ω results to 1D analysis to assess the model uncertainty.

The mean flow parameters that are compared are the bulk velocity, the friction factor, and the wall shear stress. The one-dimensional equations that were used are:

$$\frac{dp}{dx} = -f\frac{(\mu Re)^2}{2\rho D^3}, \tag{2.27}$$

$$\tau_w = -\frac{D}{4}\frac{dp}{dx}, \tag{2.30}$$

$$\frac{1}{\sqrt{f}} \approx -2.0\log_{10}\left(\frac{k/D}{3.7} + \frac{2.51}{Re\sqrt{f}}\right). \tag{2.40}$$

The pressure difference of the 2D stationary periodic boundary condition was determined by choosing a Reynolds number, calculating the corresponding friction factor from Equation 2.40, and inserting the parameters into Equation 2.27. Thus, the 2D and 1D pressure difference are identical. However the 2D bulk velocity, wall shear stress, and the friction factor are dependent upon the accuracy of the k-ω Model.

In this section, results from the 1D stationary analysis are considered the correct value. The 2D model's uncertainties are given in percent and are calculated by

dividing the difference between 1D and 2D results by the 1D result, e.g.

$$\% \text{ Uncertainty} = 100 \left(\frac{\text{2D} - \text{1D}}{\text{1D}} \right).$$

In the first section herein, Section 6.5.1, smooth pipe flows are considered and in the second section, Section 6.5.2, flows with finite roughness at the wall are treated.

6.5.1 Stationary Flow in Smooth Pipes

Three 2D k-ω simulations were performed on meshes specifically suited to the simulated Reynolds numbers; the Reynolds numbers of the simulations were 10^4, 10^6, and 10^7, were the meshes yielded $y^+ \approx 1$ for the flows. Mean flow characteristics from these simulations are compared with the 1D steady analysis in Table 6.1, in Table 6.2 the resulting uncertainties are listed. Furthermore, several simulations with different Reynolds number were performed using the meshes applied in the transient simulations. The two meshes were adapted to attain $y^+ \sim 1$ at the highest occurring Reynolds number, which were $Re = 10^6$ and $Re = 10^7$. Figures 6.4a and 6.4b shows the uncertainty of the wall shear stress, bulk velocity and friction factor versus Reynolds number.

Table 6.1: Results from three steady state simulation in Fluent and 1D steady analysis flow for a pipe with $D = 1$ m and no roughness.

$\frac{dp}{dx}$ $\left[\frac{\text{Pa}}{\text{m}}\right]$	*1D Steady Results*			*2D k-ω Steady Results*		
	Re	f	τ_w	Re	$4C_f$	τ_w
0.00156	10^4	$3.09 \cdot 10^{-2}$	0.389 [mPa]	$9.51 \cdot 10^3$	$3.41 \cdot 10^{-2}$	0.389 [mPa]
5.845	10^6	$1.16 \cdot 10^{-2}$	1.47[Pa]	$9.996 \cdot 10^5$	$1.17 \cdot 10^{-2}$	1.47 [Pa]
408.16	10^7	$8.10 \cdot 10^{-3}$	102[Pa]	$9.998 \cdot 10^6$	$8.12 \cdot 10^{-3}$	102 [Pa]

Table 6.2: Percent uncertainty between 2D and analytical steady-state flow for a pipe with $D = 1$ m and no roughness.

1D Re	Re	f	τ_w
10^4	-4.90%	10.4%	$-1.38 \cdot 10^{-6}\%$
10^6	-0.330%	0.664%	$-5.74 \cdot 10^{-6}\%$
10^7	-0.109%	0.219%	$-2.49 \cdot 10^{-7}\%$

The bulk velocity and the friction factor predicted by the 2D k-ω simulations differs significantly from the 1D analysis; the highest uncertainty of the bulk velocity is 6.2% and for the friction factor it is 12.5%, see figure 6.4a. The wall shear stress on the other hand, has an uncertainty no larger than $\sim 0.15\%$. The 2D friction factor is calculated using the wall shear stress and the velocity squared. The friction factor uncertainty can therefore be calculated from the propagating uncertainties according to

$$\Delta f = \Delta \tau_w - 2\Delta U, \tag{6.1}$$

where the Δ prefix symbolizes that parameter is the percent uncertainty. The large uncertainty in the friction factor is almost only caused by the too low bulk velocity.

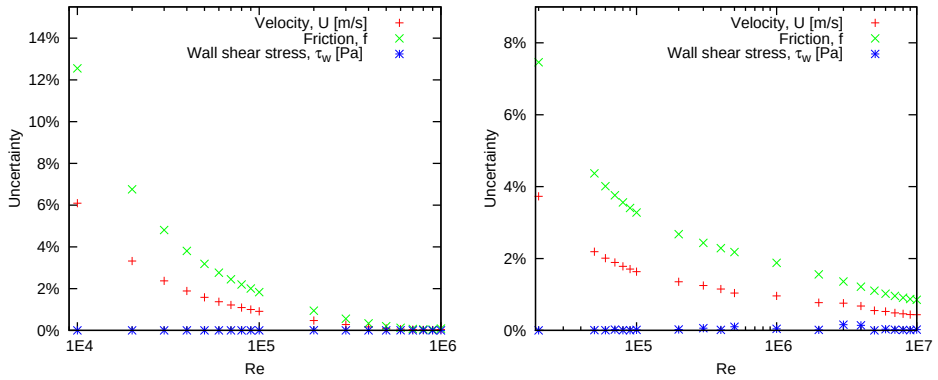

(a) Absolute uncertainty versus Reynolds number. Mesh is adapted to be adequate for flow with Reynolds number 10^6.

(b) Absolute uncertainty versus Reynolds number. Mesh is adapted to be adequate for flow with Reynolds number 10^7.

Figure 6.4: The 2D model's uncertainty in the mean results versus Reynolds number from stationary simulations with meshes adapted to $Re = 10^6$ and $Re = 10^7$ left and right figure respectively. The Re-scales are logarithmic.

However, the uncertainty of the 2D k-ω model's predicted bulk velocity decreases with increased Reynolds number of the simulations. The uncertainty is below 2% in both meshes when simulating flow with $Re = 10^6$. In addition to the Reynolds number, the uncertainties are dependent on the mesh; in the simulations where the first node $y^+ \ll 1$ the uncertainties are larger than in simulations with the same Reynolds number, but with $y^+ \sim 1$, and in simulations with $y^+ > 2$ the k-ω model over-predicts the bulk velocity.

The uncertainty in velocity converges towards zero in the mesh adapted to 10^6, while the uncertainty converges towards 0.44% in the mesh adapted to $Re = 10^7$. The two meshes both had $y^+ \approx 1$, but the radial cell expansion factor was 1.2 and 1.1 for $Re = 10^6$ and 10^7 respectively. A simulation with a cell expansion factor of 1.1 with the same y^+ yielded an uncertainty of 0.56% in the velocity. This implies that the solution was not space resolution independent, and that a high radial cell expansion factor increases the predicted bulk velocity, and in the case of the $Re = 10^6$ adapted mesh the increased velocity is the similar to the bulk velocity undershooting occurring in the k-ω simulations. Although the $Re = 10^6$ mesh did not give a mesh independent solution, it was judged that the simulated transient results was still trustworthy.

There are numerous causes that can increase uncertainties of the k-ω simulations; Oberkampf et al. [21] lists five sources to simulation errors; these are: physical modelling errors, discretization and solution errors, programming errors, and computer round-off errors. The programming errors and computer round-off

errors are assumed to have been handled by the Fluent development teams.

It is believed that most of the uncertainties in the k-ω model simulations is the result of uncertainties in the underlying physical models. In general there is a lack of complete knowledge and understanding of the complex physical processes in turbulence flow, this is reflected in the turbulence models by the uncertainties when compared to real world experiments. Some of the uncertainty can be related to the physical geometry; the empirical constants used in the k-ω model are calculated from flat plate experiments [38], and are likely not applicable to pipe geometry without calibrations.

6.5.2 Stationary Flow In Rough Pipes

To investigate the impact of roughness height to the wall with respect to the uncertainty of the simulations several simulations at different Reynolds numbers and with varying wall roughness height was conducted. The goal was to simulate transient behaviour in transitional roughness regime where $4 < k^+ < 60$.

As mentioned in Section 5.5 the wall roughness height should not be resolved by the mesh. This requirement can be in conflict with the requirement to the first node y^+ value, especially so when a flow in the transitional regime were to be simulated. Lets consider a flow where the roughness height k is equal or smaller than the first node y height, yielding $\frac{k}{y} \leq 1$. Dividing k^+ by y^+ gives

$$\frac{k^+}{y^+} = \frac{k\frac{u_\tau}{\nu}}{y\frac{u_\tau}{\nu}} = \frac{k}{y}, \tag{6.2}$$

solving for y^+ and inserting $\frac{k}{y} \leq 1$

$$y^+ = k^+\frac{y}{k} \Rightarrow y^+ \geq k^+. \tag{6.3}$$

This means that if the transitional roughness regime is to be simulated the first node must have $y^+ \geq 4$, which will result in increased uncertainties of the simulation. Although this was anticipated to occur, simulations at the limit of the transitional roughness regime was attempted

Five stationary simulations with Reynolds number 10^6 and four simulations with Reynolds number 10^7 were performed; in these simulations the roughness coefficient varies from 0.0382 to 6.93, see Table 6.3 for an overview. The right column of Table 6.3 is a measure of the importance the roughness is to the flow. For $\left(\frac{k}{D}\right) Re < 10$, roughness is unimportant and for $\left(\frac{k}{D}\right) Re > 1000$ the flow is fully rough [33].

As with the stationary simulations of flows in smooth pipes, the wall shear stress, bulk velocity and friction factor were extracted and compared to 1D steady-state analysis.

Figure 6.5 and figure 6.6a shows that the uncertainty of the bulk velocity increases with increased k^+ above 1. The cause of increased uncertainty is most likely caused by the too high first node y^+ value, since $y^+ > 5$ tend to give too high bulk velocity compared to one-dimensional analysis, see figure 6.1a. This is illustrated

Table 6.3: Roughness height for the simulations in figure 6.5 and figure 6.6.

Simulation	k^+	*Roughness height* k[m]	$\left(\frac{k}{D}\right)$ *Re*
Re 10^6	0.0382	$1 \cdot 10^{-6}$	1
	0.192	$5 \cdot 10^{-6}$	5
	0.385	$1 \cdot 10^{-5}$	10
	1.99	$5 \cdot 10^{-5}$	50
	4.10	$1 \cdot 10^{-4}$	100
Re 10^7	0, 320	$1 \cdot 10^{-6}$	10
	1.64	$5 \cdot 10^{-6}$	50
	3.35	$1 \cdot 10^{-5}$	100
	6.93	$2 \cdot 10^{-5}$	200

by figures 6.6a and 6.6b, where the the uncertainty is plotted against roughness coefficient in Figure 6.6a and in Figure 6.6b the first node y^+ value versus k^+ from the same simulations are shown. In addition, u^+ is displaced according to equation (2.36) and equation (2.37). u^+ is a function of k^+ and y^+. If u^+ is displaced, so is y^+, as seen in figure 6.6b.

Reliable solutions was not obtained with roughness coefficient above 4, due to the unsatisfactory high y^+ value. This severely limits the possibility to simulate transients in the transitional roughness regime, without compromising the accuracy of the simulation.

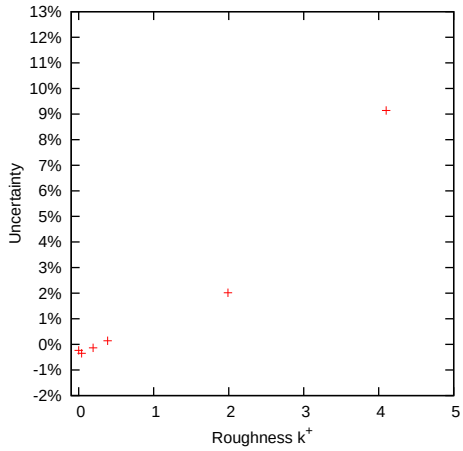

Figure 6.5: Percent uncertainty in velocity between two- and one-dimensional analysis with respect to pipe wall roughness. The flow is stationary and with Reynolds number 10^6.

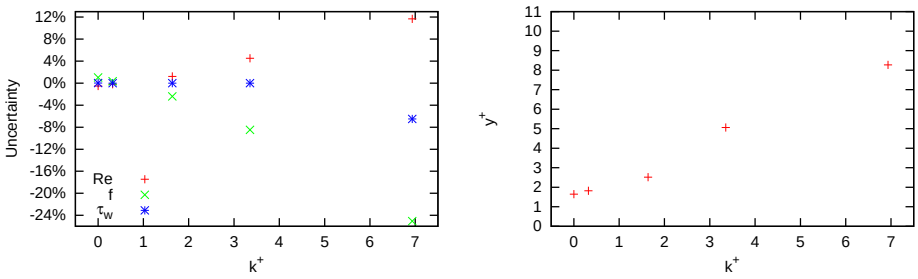

(a) Percent error for Reynolds number and Friction factor against k^+.

(b) The same simulations plotted against the first node y^+ value

Figure 6.6: Error between 2D and 1D when wall roughness is present. The flow is stationary and with 1D Reynolds number 10^7.

Chapter 7

Results and Discussion

In this chapter the results are presented and discussed. The first section covers transient laminar flow, highlighting the difference between stationary and transient friction in simple flows. In the next section the transient turbulent ramp-up results are presented, thereafter, a section on the transient ramp-down results, and lastly the section covering transient flows in pipes with roughness height. Each section's main findings are summarized at the end of the respective section. There have been simulated a total of 15 transients, five laminar transients, whereof three were ramp-up flows and two were ramp-down flows, and 10 turbulent transients, where six simulations were in smooth pipes, three accelerating and three decelerating, and four in rough pipes, two accelerating and two decelerating.

To initiate the transients, a fully developed steady state solution with a constant pressure difference Δp_0 was at time $t = 0$ subjected to a step change in pressure difference to a new constant pressure difference Δp_1. The transients were then simulated until a new steady state solution was obtained.

To avoid simulating the transition between laminar and turbulent flow the initial and end bulk velocities were either well above or below the turbulent region ($Re > 2300$ for pipe flow) in all transient cases. The meshes used in the turbulent transient simulations up to $Re = 10^6$ had an expansion factor of 1.2, and for higher Reynolds-number flows the expansion factor was 1.1. All meshes were adapted to suit the highest Reynolds number occurring in the transient case.

The bulk velocity, wall shear stress and the Darcy friction factor was extracted from the one-dimensional models and from the two-dimensional model. These quantities were then manipulated using self-made Fortran-codes to produce data-sets that were plotted using Gnuplot. Since the Darcy friction factor definition (2.24) is only valid in stationary conditions, the two-dimensional Darcy friction factor is calculated through the definition of the Fanning friction factor (2.25) times four

$$f = 4C_f = 4\frac{\tau_w}{\frac{1}{2}\rho U^2}. \tag{7.1}$$

The bulk velocity from the two-dimensional model had a significant systematic uncertainty compared to one-dimensional steady-state analysis, see Section 6.5. However, this was not an issue for the two-dimensional wall shear stress. At the initial solution in e.g. the turbulent transient Case-2, the 2D wall shear stress uncertainty from 1D results was $6.27 \cdot 10^{-3}\%$ compared to 3.54% for the bulk velocity. Transient effects on the friction factor stems from the transient effects on the the wall shear stress. Therefore the transient effects on the wall shear stress rather than on the friction factor are shown in the results.

In the forthcoming sections the term "error" will be used instead of uncertainty when referring to differences between the 1D models and the 2D model. It is assumed that the differences between the models are mainly caused by the 1D unsteady friction modelling, and therefore may be seen as an recognizable deficiency. Moreover, the 2D model is considered as the correct, so that the error is calculated as

$$\% \text{ Error} = 100\frac{1D - 2D}{2D}. \tag{7.2}$$

In this text, ramp-up transients are considered accelerating flows and ramp-down transients are considered decelerating flows.

In the figures the data sets are labelled with the model which was used to obtain the data. The laminar 2D model is labelled with "2D laminar", the k-ω two-dimensional model is labelled with "2D k-ω". Results from the 1D quasi-stationary friction model are labelled with "Steady Friction", the results from the instantaneous acceleration model with the Brunone coefficient are labelled with "Daily et al.", and the weighting function based unsteady friction model are labelled with "Vardy et al.".

7.1 Laminar Transient Results

Laminar flow has fewer variables and simulations are significantly less computational costly than for turbulence flows. Simulating laminar transients may yield understanding of transient effects on the friction factor without the added complexity from turbulence. Five laminar transients was therefore simulated with fluent. They have been compared with two 1D laminar models, one with quasi-steady friction modelling, and the other with the Daily et al. friction modelling. In Table 7.1 the parameters describing the different cases are presented.

With the diameter set to one meter the flow evolves slowly so very large time-steps were used. Transient laminar case five has the same non-dimensional parameters as laminar case 4, but the diameter was set to 0.1m and the time step was set to 50s, which yields the same non-dimensional time step $\Delta t^* = 7.54$. Case 4 and 5 were almost identical in all other aspects, see Figure 7.1. Figure 7.1b shows that the ramp-down flows converge faster towards the new steady-state than the ramp-up flows. Furthermore, it shows that the flows with larger difference between Re_0 and Re_1 converged slower in non-dimensional time than those with less difference between start and end Reynolds number.

The friction factor in the laminar transients deviates clearly from the stationary friction, as can be seen in figures 7.2a and 7.2b, where the friction factor from the laminar transients are plotted alongside the steady friction factor verses Reynolds number. The unsteady component of the friction factor is positive in the ramp-up flows and negative in the ramp-down flows, see Figure 7.2b. In addition, the magnitude of the unsteady component increases with increased difference between Re_0 and Re_1. This validates the assumption that the unsteady component of the friction factor may be modelled by the instantaneous acceleration, as is the case for the Daily et al. friction model.

The transient friction in the ramp-down flows was smaller than the transient friction in the equivalent ramp-up flow, this causes the observed faster convergence of the ramp-down flows; on average, the decelerating flow is subjected to less friction during the transient.

Table 7.1: Summary of the key parameters for the simulated laminar transients.

Laminar case	Re_0	Re_1	Δt	D	Flow time
1	0	500	5ks	1m	65ks
2	0	1000	5ks	1m	65ks
3	0	1500	5ks	1m	65ks
4	1500	0	5ks	1m	65ks
5	1500	0	50s	0.1m	650s

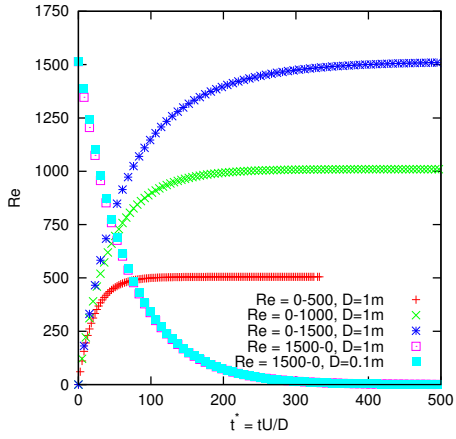

(a) Reynolds number versus time.

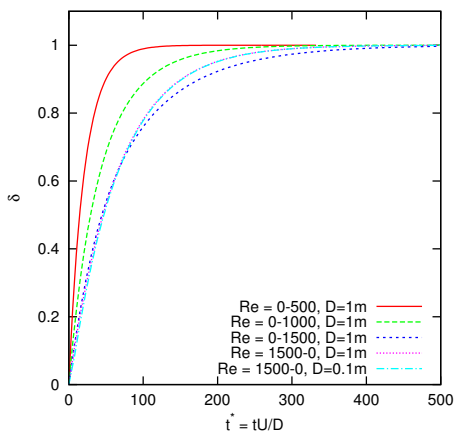

(b) Dimensionless plot of the laminar transients. δ is a dimensionless variable; for ramp-up flows $\delta = \frac{u}{U_{max}}$ and for ramp-downs $\delta = 1 - \frac{u}{U_{max}}$

Figure 7.1: Laminar transient results from ramp-up and ramp-down simulation. Reynolds number is limited 1500

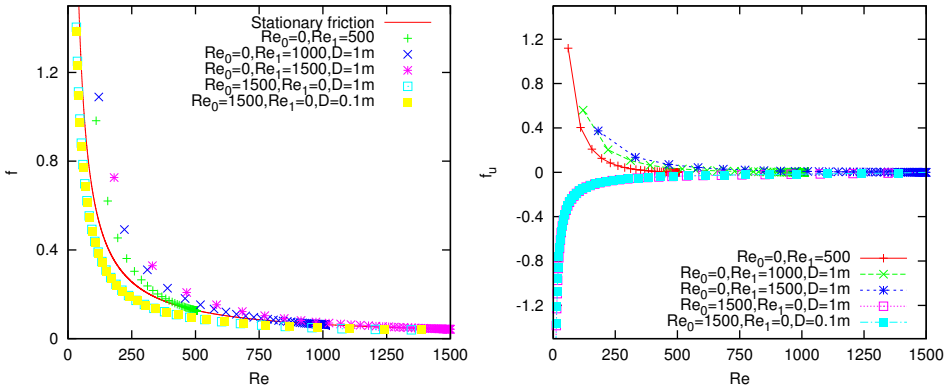

(a) Darcy friction factor plotted against Reynolds number.

(b) Unsteady component of the friction factor versus Reynolds number

Figure 7.2: Friction factor and the unsteady component of the friction factor versus Reynolds number from different laminar cases.

7.1.1 1D Laminar Friction Models Evaluation

In this section the friction models which was implemented in the 1D laminar model are evaluated. The implemented friction models was the quasi-steady friction model and the Daily et al. friction model with constant friction coefficient k_1. In the transients $k_1 = 0.449$; a value proposed by Carstens et al. [8]. However, the proposed value yielded poor results for the ramp-down simulations, a new value more suitable was found, by trial and error, for the ramp-down cases.

The bulk velocity and the wall shear stress from the 2D model and the 1D models are compared in figures 7.3(case 1), 7.4(case 2), 7.5(case 3), and 7.6(case 4); the left side shows the velocity while the right side depicts the wall shear stress. Results from case 5 were exempted, as they are in essence the same as for case 4.

The quasi-steady friction model's wall shear stress undershoots the 2D wall shear stress in the first part of the ramp-up simulations. Furthermore, the initial undershooting causes the 1D velocity to overshoot the 2D bulk velocity until convergence. The trend is opposite for the ramp-down flow, where the 1D quasi-steady wall shear stress overshoots at the start of the transient, and the velocity subsequently undershoots the 2D bulk velocity.

The Daily et al. friction modelling significantly improved the velocity predictions compared to the quasi-steady friction modelling in all transients, although, with decreasing accuracy with larger difference between Re_0 and Re_1. However, the predicted wall shear stress deviated more from the 2D results than the quasi-steady wall shear stress. This paradox is most likely the result of the 1D laminar model's time advancement, discussed in Section 4.5. In the ramp-down simulation the proposed value of $k_1 = 0.449$ yields unsatisfactory modelling of the transient wall shear stress; trial and error gave a more suitable modelling when $k_1 = 0.3$, see

Figure 7.6.

Overall, the Daily et al. friction model applied to the 1D laminar model gave significantly better results than with quasi-steady friction; both by predicting the correct sign of the unsteady component and to some extent the form. Furthermore the friction coefficient k_1 can be changed to give more accurate results.

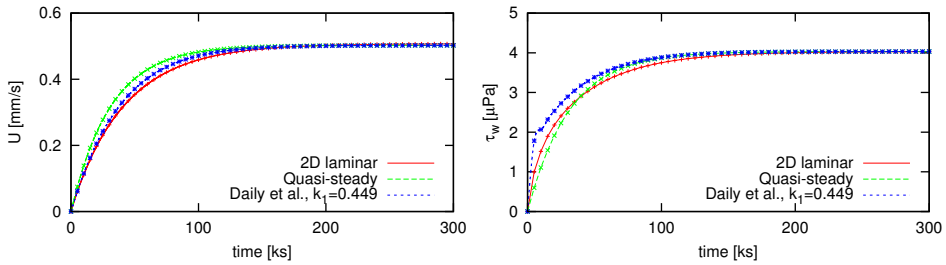

(a) Velocity development. (b) Wall shear stress development

Figure 7.3: Laminar transient results from simulation of ramp-up from $Re_0 = 0$ to $Re_1 = 500$

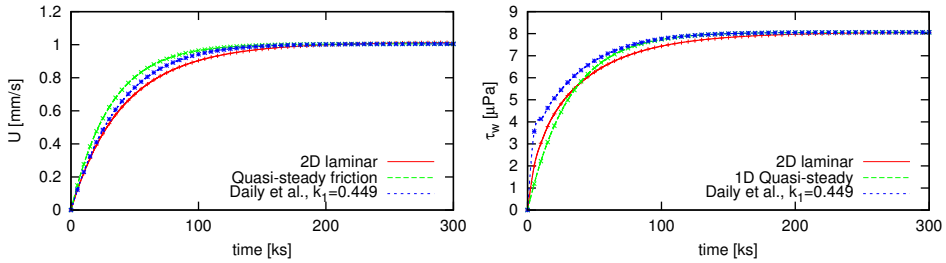

(a) Velocity development. (b) Wall shear stress development

Figure 7.4: Laminar transient results from simulation of ramp-up from $Re_0 = 0$ to $Re_1 = 1000$

7.1.2 Laminar Transient Simulations Summary

The simulated laminar transients showed that the wall shear stress indeed differs from the quasi-steady wall shear stress. The sign of the unsteady component is determined by whether it is an accelerating or a decelerating flow; accelerating flows gives a positive sign and decelerating flows gives a negative sign. The magnitude of the unsteady component increases with increased difference between Re_0 and Re_1. Furthermore the ramp-down flows converges faster in non-dimensional time then corresponding ramp-up flows. This was found to be due to transient behaviour which decreased the friction in the ramp-down flows and increased the friction in the ramp-up flows.

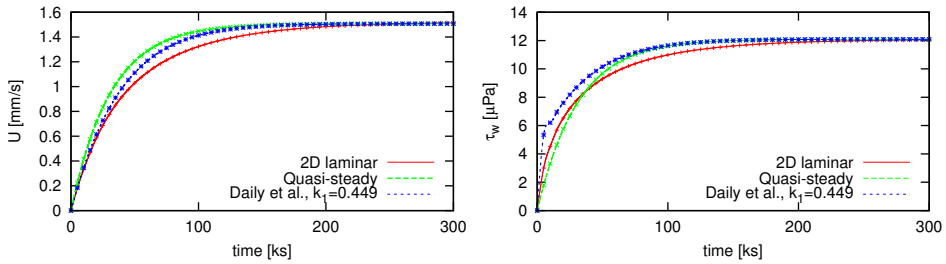

(a) Velocity development. (b) Wall shear stress development

Figure 7.5: Laminar transient results from simulation of ramp-up from $Re_0 = 0$ to $Re_1 = 1500$

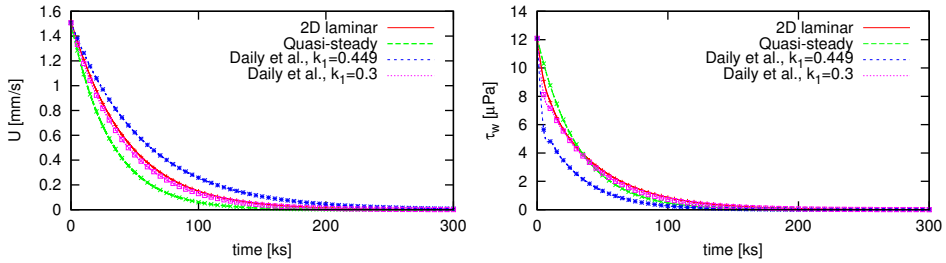

(a) Velocity development. (b) Wall shear stress development

Figure 7.6: Laminar transient results from simulation of ramp-up from $Re_0 = 1500$ to $Re_1 = 0$

The 1D quasi-steady friction model modelled the velocity poorly compared to the modelling with the 1D Daily et al. friction model. Albeit, the friction coefficient in the Daily et al. model needed refinement in the ramp-down simulations. Nevertheless, the Daily et al friction model produced far better results than the quasi-steady model.

7.2 Ramp-up Transients in Smooth Pipes

Three accelerating turbulent transient cases were simulated. The first case starts at Reynolds number 10^4 and ends at Reynolds number 10^6, the second and third cases are from Reynolds number $2 \cdot 10^4$ to 10^7, however, the third case has a different diameter than the second case. The higher start Reynolds number of the latter two transients was chosen to reduce the k-ω model bulk-velocity undershooting compared to one-dimensional results. An overview of key parameter of the simulated transients are found in Table 7.2. It may be noted that data was only recorded at every 10th time step in the simulations of transient Case-1 and -2; the calculation at every time step was significantly quicker than writing the data to files. The ramp-up simulation with pipe diameter $D = 0.01$m was not simulated until a stationary solution was obtained, it is only used to explore the impact of different diameter in the turbulent transients. The initial solution and end solution errors from the stationary 1D analysis are listed in Table 7.3.

Table 7.2: Table containing key parameters of the turbulent ramp-up transients.

Case	Re_0	Re_1	D	k	Δt	Flow time
1	$1 \cdot 10^4$	$1 \cdot 10^6$	1 m	0	125 ms	700 s
2	$2 \cdot 10^4$	$1 \cdot 10^7$	1 m	0	25 ms	150 s
3	$2 \cdot 10^4$	$1 \cdot 10^7$	0.01 m	0	50 µs	0.438 ms

Table 7.3: Start and end uncertainty between the two-dimensional k-ω and one-dimensional stationary analysis.

Transient	Start of simulation		End of simulation	
case	U	τ_w	U	τ_w
1	−5.27%	0.957%	−0.135%	−0.171%
2	−3.54%	0.00627%	−0.516%	0.00166%

From Table 7.3 we see that the start and end 2D solutions are close to the 1D stationary flow analysis indicating a converged solution at both initial state and end state.

7.2.1 Observed Flow Behaviour in the Ramp-up Simulations

In this section the flow behaviour from the 2D k-ω ramp-up simulations are examined. First, are the key mean flow parameters, velocity, wall shear stress, unsteady component of the wall shear stress, and acceleration, from Case-1 and -2 inspected in an effort to identify characteristic flow behaviour. Four characteristic time scales are discovered; velocity and turbulence profiles in the vicinity of the occurrence of the time scales are extracted from the simulation of Case-2 and plotted. In Section 7.2.2 the profiles are investigated and related to the wall shear stress, velocity, and acceleration response.

Normalized bulk velocities and wall shear stress from the three ramp-up cases are presented in the two top figures in Figure 7.7. The bottom left and right figures in Figure 7.7 shows the unsteady component of the wall shear stress. To find the unsteady component, the wall shear stress applicable in steady flows with the same instantaneous Reynolds number was subtracted at each time step. The velocity undershooting from the 2D model's inaccuracy propagated to the calculated steady wall shear stress, causing a higher unsteady component than the actual unsteady component.

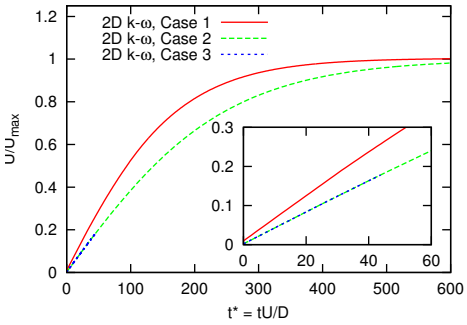

(a) Normalized bulk velocity.

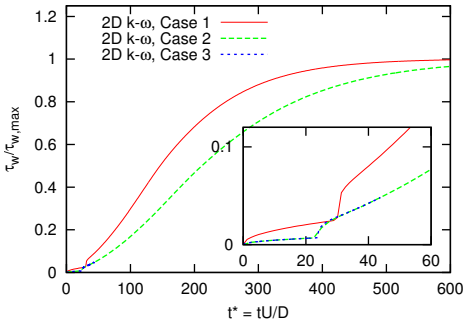

(b) Normalized wall shear stress.

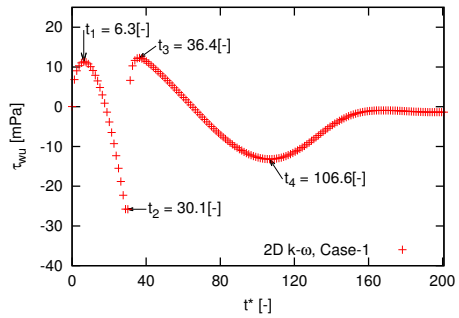

(c) τ_{wu} from ramp-up Case-1.

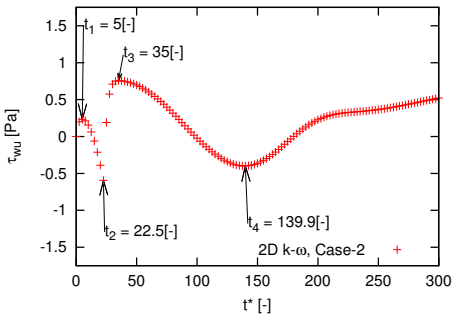

(d) τ_{wu} from ramp-up Case-2.

Figure 7.7: The two top figures shows the bulk velocities and the wall shear stresses normalized by their respective maximum; the bulk velocities are on the left side and the wall shear stresses are on the right side. The bottom figures shows the unsteady component of the wall shear stress from Case-1 (left) and -2 (right). In addition, the wall shear stress' characteristic turning points are marked and labelled on the bottom two figures. The time scales in the figures are non-dimensional.

Case-2 and -3 simulations overlaps when non-dimensional parameters are used, see figures 7.7a and 7.7b. This coincide well with the understanding of fluid dynamics; a flow will behave in the same manner as a flow with the same non-dimensional parameters, in this case Re_0 and Re_1. Different diameters does not change the nature of the transient flow if $\frac{k_s}{D}$, Re_0, and Re_1 are the same.

Transient Case-1 converges faster in non-dimensional time than the two other cases. This is explained by the smaller difference between the initial Reynolds number and the end Reynolds number.

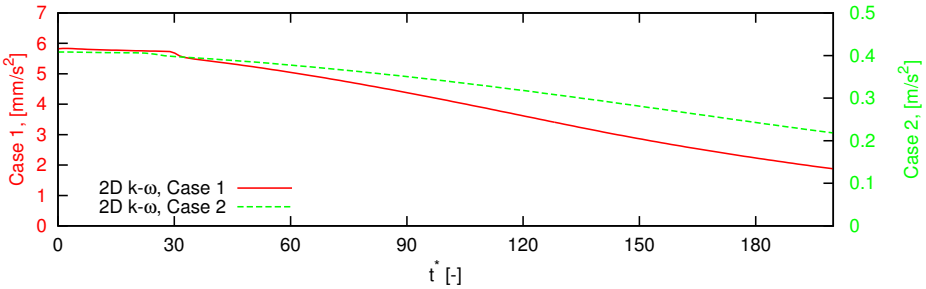

Figure 7.8: Acceleration from Case-1 and -2 versus non-dimensional time. Note that different acceleration scales are used on the cases.

The 2D wall shear stress deviates greatly from the quasi-steady wall shear stress in the ramp-up transients. Additionally, the unsteady component of the wall shear stress development in the ramp-up cases exhibits the same pattern. It has four distinct turning points which are chronologically labelled with t_1, t_2, t_3, and t_4 in figures 7.7c and 7.7d; these turning points may be considered time-scales describing the unsteady wall shear stress. First the unsteady component rises up to a local maximum at time t_1, after this it changes sign and becomes negative. At t_2 it reaches its minimum value before abruptly rising becoming positive and fast encountering a new local maximum at t_3. Before reaching the last local minimum at t_4, τ_{wu} reverses sign and becomes negative. After the last minimum the unsteady component converges almost asymptotically towards a quasi-steady state. The magnitude of the τ_{wu} at the turning points may be regarded as measures of the strength of the unsteady wall shear stress [12].

Despite the large unsteady component components of the wall shear stress, the velocity development is not significantly altered, see the small figures in Figure 7.7a and in Figure 7.7b. However, some impact on the velocity is visible if inspecting the acceleration, see Figure 7.8; the acceleration is almost constant until the unsteady component of the wall shear stress reaches its minimum. At that point the acceleration drops and the negative acceleration slope increases. This transpires at the same time as the turbulent kinetic energy increases rapidly, indicating that energy was transferred from inertia to increased turbulence dynamics at that time.

Seddighi et al. [25] which simulated ramp-up flows with DNS up till Reynolds number 5000, found that the transient wall shear stress first overshoots, then undershoots the stationary wall shear stress for a longer period of time before converging asymptotically. He et al [12] simulated constant accelerating flow until Reynolds number $5 \cdot 10^4$, where similar unsteady behaviour was reported. The reported unsteady wall shear stress behaviour is similar to what is found in this work, but the number times the unsteady component of the wall shear stress changes sign is not

the same, see figures 7.7c and 7.7d. The 2D wall shear stress from the ramp-up simulations seems to oscillate with decreasing frequency before converging. Perhaps the extra "oscillation" is a result of the much greater difference between Re_0 and Re_1 used in the simulations in this thesis compared to the simulations of He et al.[12] and Seddighi et al.[25].

7.2.2 Flow Dynamics around the Characteristic Time Scales

To investigate the flow dynamics around the time scales t_1, t_2, t_3, and t_4 velocity profiles, universal velocity profiles, turbulent viscosity profiles, and turbulent kinetic profiles were extracted from simulation of Case-2 and plotted. The profiles appear in the same order as listed above. Profiles from around t_1 are shown in Figure 7.9, t_2 in Figure 7.10, t_3 in Figure 7.11, and t_4 in Figure 7.12. The figures on the left depicts the dynamics close to the wall while the right side figures includes the whole radius.

The velocity profiles from the time steps around t_1 are accelerated to an almost uniform velocity profile, increasing the velocity field close to the wall and thus the wall shear stress. The distortion reaches its maximum at t_1, after this the velocity profile retracts slightly from the wall, see figures 7.9a and 7.9b. There are great deviances between the universal velocity profile and the unsteady profiles, first below, then increasingly above as the τ_{wu} decreases after the local maximum (figures 7.9c and 7.9d. The turbulence viscosity remains unchanged during this period while the turbulence kinetic energy rises slightly close to the wall from $t = 0.75$, see figures 7.9e and 7.9g.

In the time steps before the minimum at $t_2 = 2.25$s, the velocity profile continues to retract from the wall at a slow rate. At $t = 2.5$s the velocity profile close to the wall has undergone an angled flattening, increasing the velocity gradient normal to the wall from $r = 0.999R$ to R, see figures 7.10a and 7.10c. At the minimum t_2 the turbulence viscosity is still unchanged while the kinetic energy has increased slightly. Right after the minimum the turbulent kinetic energy close to the wall increased with a magnitude of over 3 compared to the previous profile; a sharp increase of the turbulence viscosity is also seen. The extent of the induced turbulence propagates further from the wall with each time step. The increase in turbulence is highest a short distance from the wall, this increased turbulence slows down the velocity, creating the angled flattening of the velocity profile, see figures 7.10e and 7.10g.

The unsteady component of the wall shear stress is once again positive as it rises towards the time-scale $t_3 = 3.5$s. The velocity profile is rounding off, resembling the universal velocity profile for larger and larger y^+ values, see Figure 7.11d. The extent of the turbulence extends further for each time step, but is far from diffusing through to the axis. The turbulence viscosity remains mostly unchanged from the axis to about $0.9R$, while the turbulence kinetic energy is unchanged to $r \approx 0.95R$, see figures 7.11e and 7.11g. The turbulence is rounding off the velocity profile with increasing distance from the wall.

The velocity profiles at times around t_4 are almost indistinguishable from the universal velocity profile, although some distortions are visible for $y+ > 10000$, see Figure 7.12d. The velocity profiles right before the last turning point are rounding off near the axis, to where the turbulence has diffused. At the minimum $t_4 = 14$s the turbulence has extended throughout the radius of the pipe, and the flow evolves towards a quasi-steady flow.

According to Vardy et al. [31] the two main reasons for deviation from quasi-stationary wall shear stress are inertia due to acceleration or deceleration and effects from delayed response of turbulence dynamics. When the unsteady wall shear stress overshoots, inertia forces dominates and when it undershoots turbulent forces dominates. This coincide well with the observed flow dynamics in the ramp-up simulations.

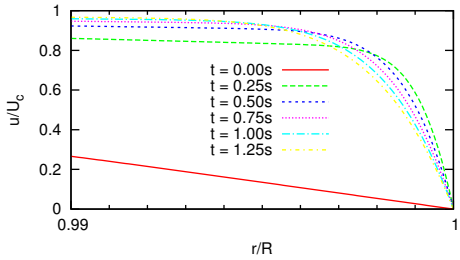

(a) Velocity profiles close to the wall.

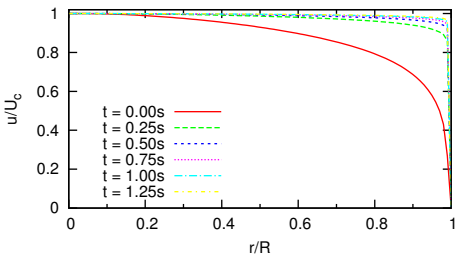

(b) Velocity profiles.

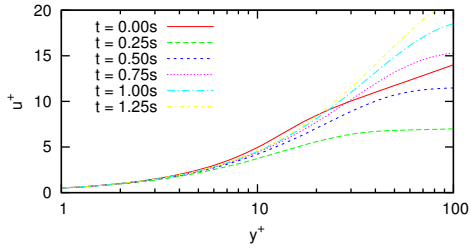

(c) Universal Velocity profiles close to the wall.

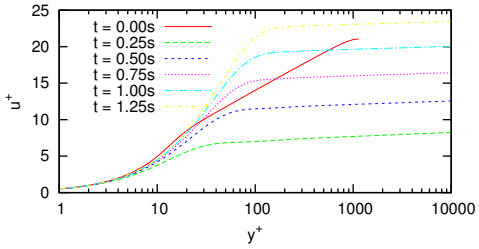

(d) Universal velocity profiles.

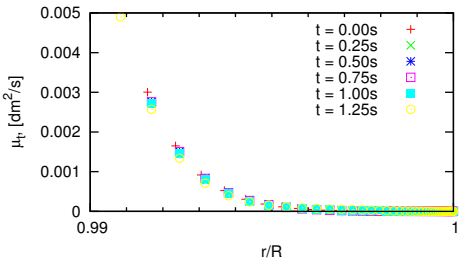

(e) Turbulent Viscosity close to the wall.

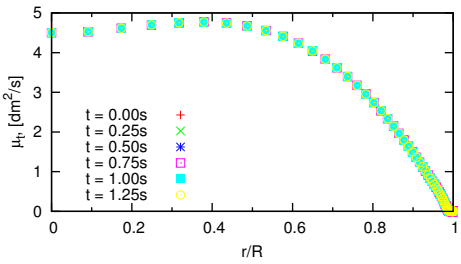

(f) Turbulent Viscosity.

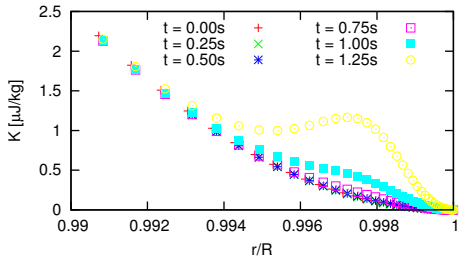

(g) Turbulent kinetic energy close to the wall.

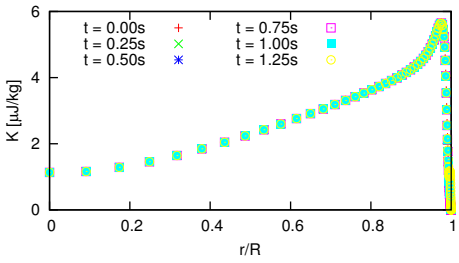

(h) Turbulent kinetic energy K.

Figure 7.9: Velocity, turbulence kinetic energy, inertia, and eddy viscosity before, during, and right after the first turning point of τ_{wu}. All result from Case-2 simulation.

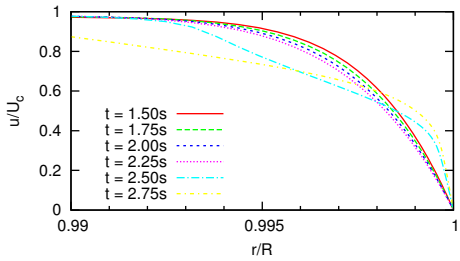

(a) Velocity profiles close to the wall.

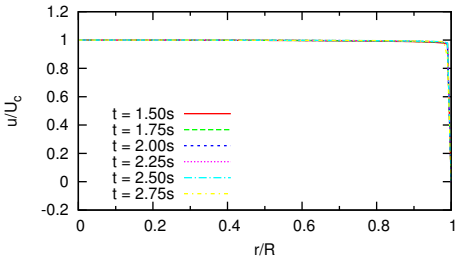

(b) Velocity profiles.

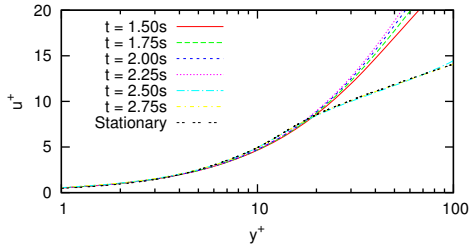

(c) Universal Velocity profiles close to the wall.

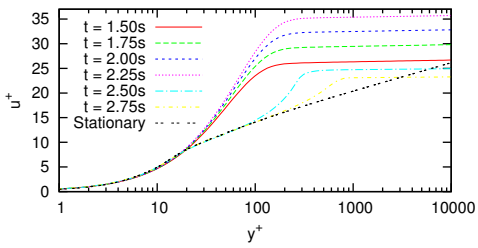

(d) Universal velocity profiles.

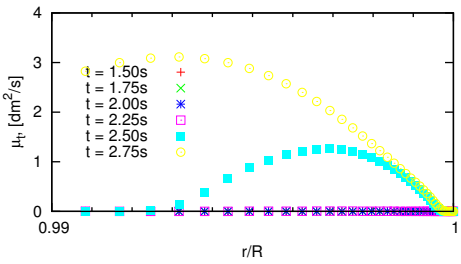

(e) Turbulent Viscosity close to the wall.

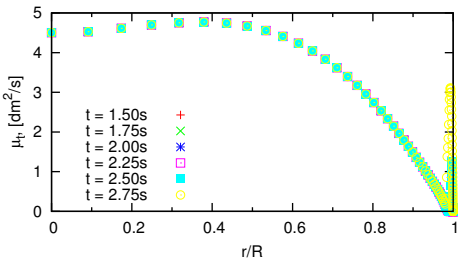

(f) Turbulent Viscosity.

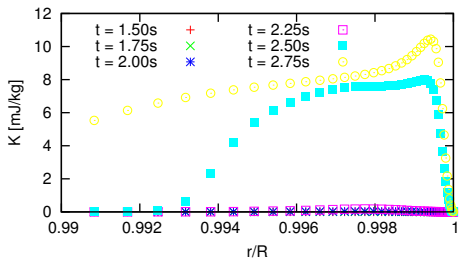

(g) Turbulent kinetic energy close to the wall.

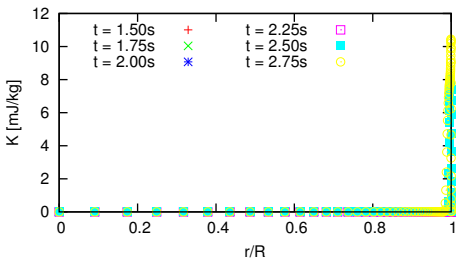

(h) Turbulent kinetic energy K.

Figure 7.10: Velocity, turbulence kinetic energy, inertia, and eddy viscosity before, during and right after the second turning point of τ_{wu}. All result from Case-2 simulation.

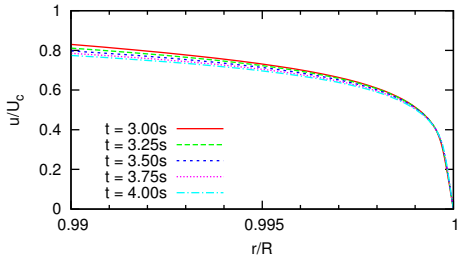

(a) Velocity profiles close to the wall.

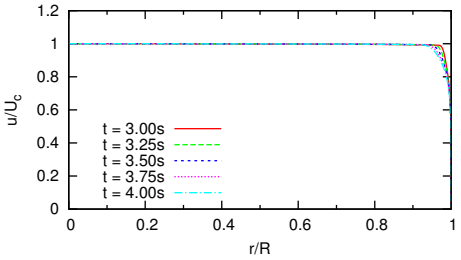

(b) Velocity profiles.

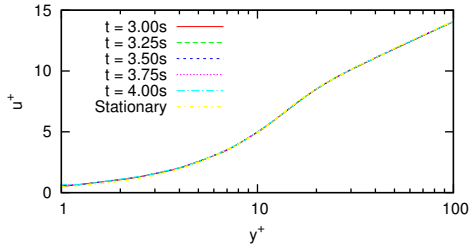

(c) Universal Velocity profiles close to the wall.

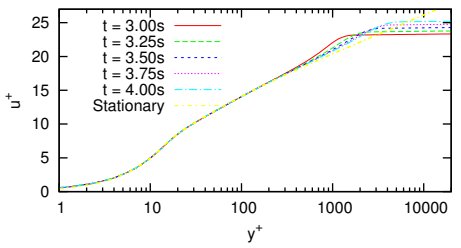

(d) Universal velocity profiles.

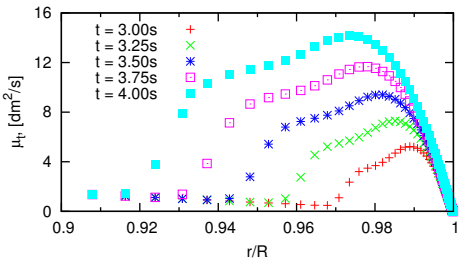

(e) Turbulent Viscosity close to the wall.

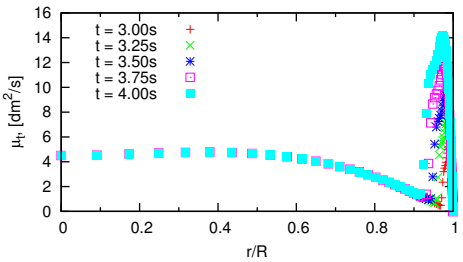

(f) Turbulent Viscosity.

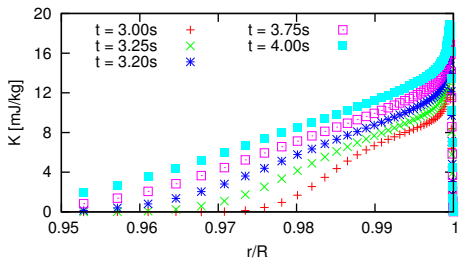

(g) Turbulent kinetic energy close to the wall.

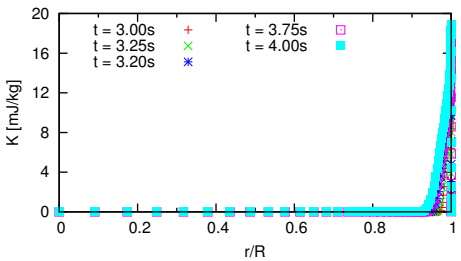

(h) Turbulent kinetic energy K.

Figure 7.11: Velocity, turbulence kinetic energy, and eddy viscosity before, during and right after the third turning point t_3 of the τ_{wu}. All result from Case-2 simulation.

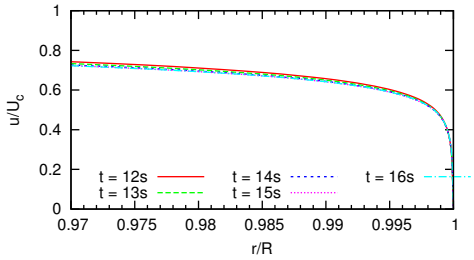

(a) Velocity profiles close to the wall.

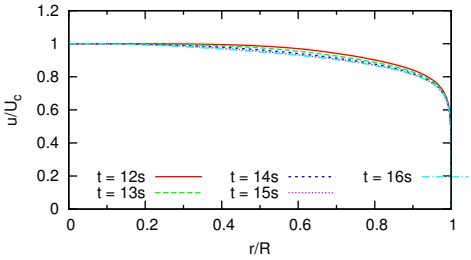

(b) Velocity profiles.

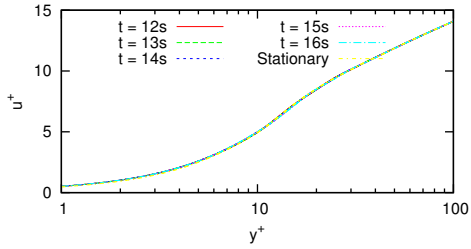

(c) Universal Velocity profiles close to the wall.

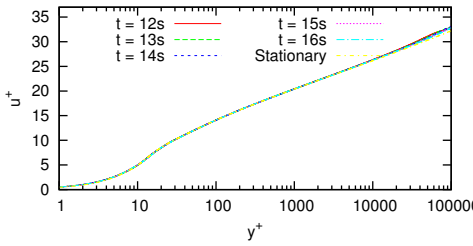

(d) Universal velocity profiles.

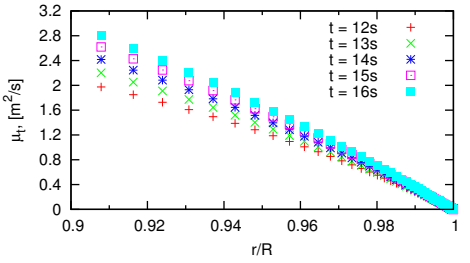

(e) Turbulent Viscosity close to the wall.

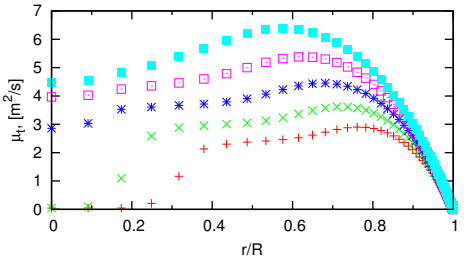

(f) Turbulent Viscosity.

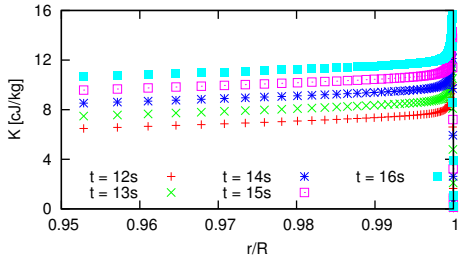

(g) Turbulent kinetic energy close to the wall.

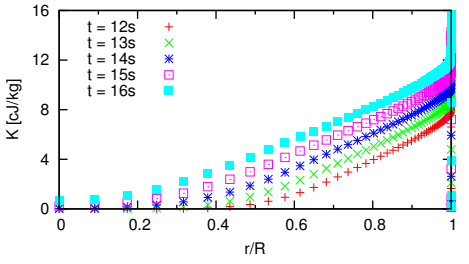

(h) Turbulent kinetic energy K.

Figure 7.12: Velocity, turbulence kinetic energy, and eddy viscosity before, during and right after the fourth turning point of the τ_{wu}. All result from Case-2 simulation.

7.2.3 Parameters Predicting the Characteristic Turning Points

Being able to predict the times at which the turning points occurs is important in order to correctly predict the unsteady wall shear stress in a 1D friction model. To predict the delay times of the turbulence, He et al. ([13] 2000) proposed an inner time scale T_p for the turbulence production delay and an outer scale T_d for the turbulence diffusion delay; the delay from when the turbulence is produced at the wall until it has propagated to the axis. The time scales are as follows:

$$T_d = \frac{D}{\sqrt{2}u_\tau}, \tag{7.3}$$

$$T_p = \frac{\nu}{u_\tau^2}. \tag{7.4}$$

The turbulence diffusion time and turbulence production delay is calculated at the instantaneous time when the turbulence is created. If the acceleration is below a certain value, the turbulence diffusion time is only dependent on the initial conditions. If the acceleration is above this value, the turbulence will have diffused through from the wall to the axis at the time defined by the minimum of the function $f(t, t + T_d)$, see figures 7.13a and 7.13b.

The initial rise time ψ_{TL} for smooth flow, (2.61) defined in Section 2.4, and the initial turbulence diffusion time from Case-1 and -2 is found in Table 7.4. Figures 7.13a and 7.13b shows the turbulence diffusion time development over time and the function $f(t, T_d + t)$ for Case-1 and Case-2 respectively. Figure 7.13c shows the limiting rise time during the transients.

Table 7.4: Rise times and turbulence diffusion times for the different start Reynolds numbers in the transient cases. The rise time is defined in equation (2.61).

Re_0	t_{LT} [s]	T_d [s]	T_p [s]
$1 \cdot 10^4$	1571.0	1132.6	2.58
$2 \cdot 10^4$	958.5	618.6	0.77

Both the turbulence diffusion time and the rise time at initial conditions are larger than the convergence time of the transient cases. However, the turbulence diffusion time reduces with increased Reynolds number. Because of the rapid increase in Reynolds number, the newly created turbulence soon catches up to the initial turbulence. The first turbulence to propagate to the axis is the turbulence created at $min(f(t, T_d + t))$ which is at 43s and 6s for Case-1 and Case-2 respectively. The turbulence has propagated to the axis at the approximate times of 105s in Case-1 and 14s in Case-2, see Figure 7.13. This coincide with the 2D profiles extracted from the simulation, where the turbulence viscosity and kinetic energy reaches the axis at 106.25s and 14s.

The characteristic turning points t_1 and t_2 may be related to the turbulence production delay T_p. The turning point t_2 can be attributed to an additional delay

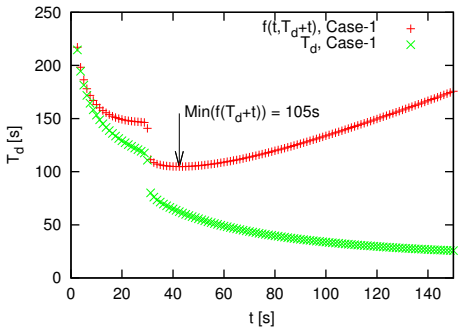

(a) Turbulence diffusion time at each time step from Case-1 transient.

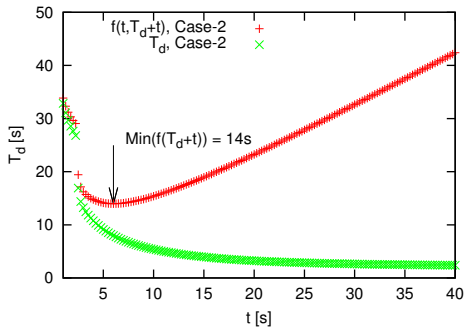

(b) Turbulence diffusion time at each time step from Case-2 transient.

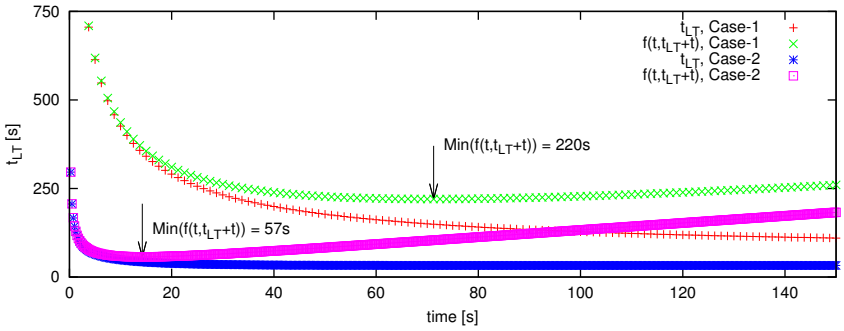

(c) Rise time from Case-1 and -2.

Figure 7.13: The two top figures show the evolement of turbulence diffusion time and the instantaneous diffusion time added to the local time. Bottom figure shows the limiting rise time. All three figures from Case-1 and -2 simulations.

in turbulence viscosity compared to the turbulence production delay. The turning point t_3 do not have any particular parameters attached to it. It is in the developing stage of the flow, when the turbulence spreads radially but parts of the flow are still not effected by the induced turbulence. t_3 may be regarded as the point where the turbulence relative to excess inertia is at its lowest. The last characteristic time can be coupled to the turbulence diffusion delay T_d. The calculated T_d deviates little from the observed turbulence diffusion delay in the profiles and the occurrence of the turning point at t_4, see figures 7.12f, 7.7d, and 7.13b.

Because of the higher initial Reynolds number, the Case-2 turbulence delay is shorter in non-dimensional time than in Case-1, this causes the three first characteristic turning points to transpire at an earlier non-dimensional time in Case-2 than Case-1, see e.g. Figure 7.7b. The last turning point occurs at an earlier non-dimensional time in Case-1 than -2 because of the shorter non-dimensional convergence time.

7.2.4 Performance of the 1D Models in the Ramp-up Transients

In this section the 1D and 2D simulation results from the transient ramp-up cases are compared. There are three 1D friction models that are compared with the 2D k-ω model, namely the quasi-stationary friction model, the Daily et al. friction model and the Vardy et al. friction model.

Because of the lack of dependence upon neighbouring time steps in the 1D models (discussed in Section 4.5), the 1D velocity will not be particularly influenced by unsteady wall shear stress behaviour from earlier time steps. To show the effect of the missing time dependency, the 2D bulk velocity and time were inserted into the 1D model (4.19) to calculate the 1D wall shear stress required to produce the 2D bulk velocity development. Subsequently, the steady component of the wall shear stress was removed from the resulting unsteady wall shear stress to produce the result presented in figures 7.14a and 7.14b. The produced unsteady component of the wall shear stress accounts for any time-shift caused by earlier time steps in the 2D k-ω simulation; resulting in an exaggerated absolute increase of the unsteady component, before the 2D model and 1D models converge together towards the end.

The resulting unsteady component does not only show the time development deficiency of the 1D model; it can yield information about the 2D wall shear stress. The turning points can be regarded as the point were the 2D unsteady component of the wall shear stress changes sign. Moreover, if the unsteady component is positive the average unsteady component must have been positive and if it is negative, the average of the unsteady component must also be negative. From the figures it can therefore be deduced that the unsteady component changes sign four times and that the unsteady component is on average positive in the ramp up simulations.

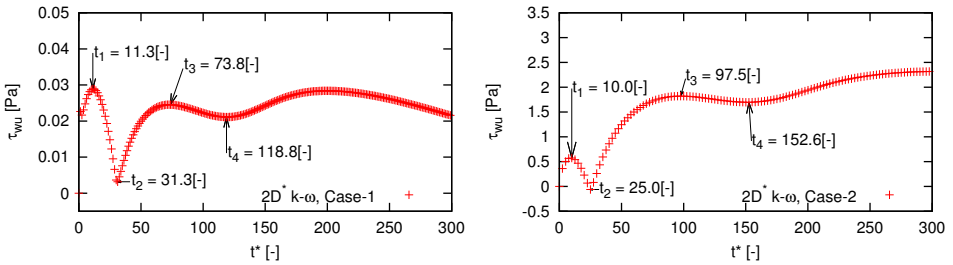

(a) 2D k-ω one-dimensionalized unsteady component of the wall shear stress from Case-1.

(b) 2D k-ω one-dimensionalized unsteady component of the wall shear stress from Case-2.

Figure 7.14: The one-dimensionalized unsteady component. Top figure from Case-1 k-ω simulation and bottom figure from Case-2 k-ω simulation.

Results from the 1D models and the 2D model simulations of Case-1 and Case-2 are compared in figure 7.15 and 7.16 respectively. Additional figures depicting the percent error between the 1D models and the 2D model can be found in Appendix

A.

All of the 1D models predicted a bulk velocity fairly close to the 2D model predictions (see figures 7.15b and 7.16b, in fact, in both ramp-up cases the largest percent error between the 1D models' and the 2D model's bulk velocity was at the stationary initial solution due to the 2D k-ω model uncertainty, see figures A.1a and A.3a in Appendix A. However, the wall shear stress predictions from the 1D models differs greatly from that of the 2D model. Ivo Pothof [23] argued that the Daily et al. and Vardy et al. friction models have several deficiencies; the importance of the initial Reynolds number should diminish after the turbulence diffusion time, the assumption of linear acceleration in the instantaneous friction model, and the symmetry of the unsteady component $\tau_{uw}\left(\frac{du}{dt}\right) = -\tau_{uw}\left(-\frac{du}{dt}\right)$, which ignores that the unsteady behaviours are caused by different physical phenomena during acceleration than in deceleration. In the same article Pothof proposed a friction model based upon observation of turbulence transients. The proposed model accounts for physical differences between acceleration and deceleration, effects from reversed flow near the wall during rapid deceleration, and the reduction of unsteady behaviour toward the turbulence diffusion delay.

To further inspect the differences, the three 1D friction models are compared to the 2D results in the three forthcoming sections.

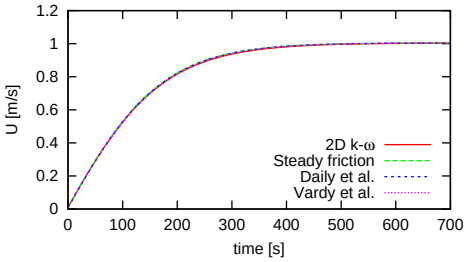

(a) Bulk velocity versus time from Case-1

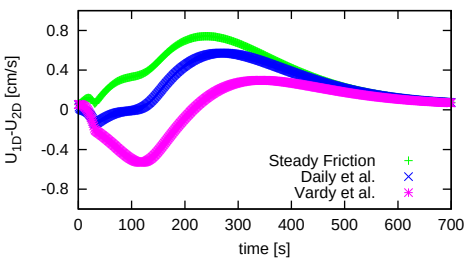

(b) Difference in bulk velocity between the 2D k-ω model and the 1D models

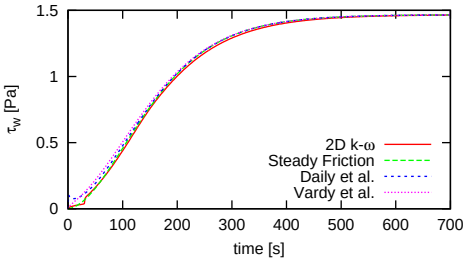

(c) Wall shear stress versus time from Case-1.

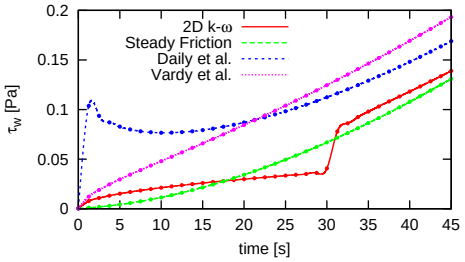

(d) Wall shear stress development in the first period of Case-1 simulations

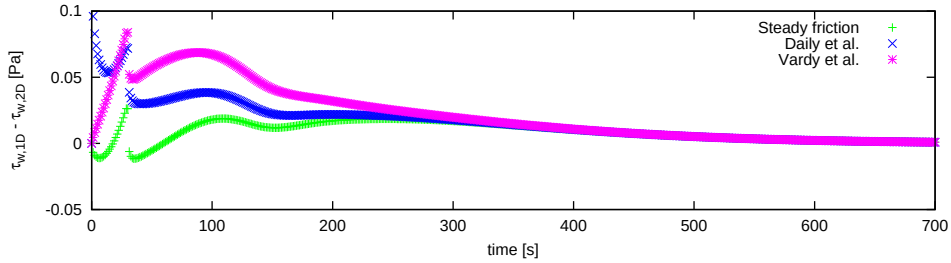

(e) Difference between 1D and 2D wall shear stress.

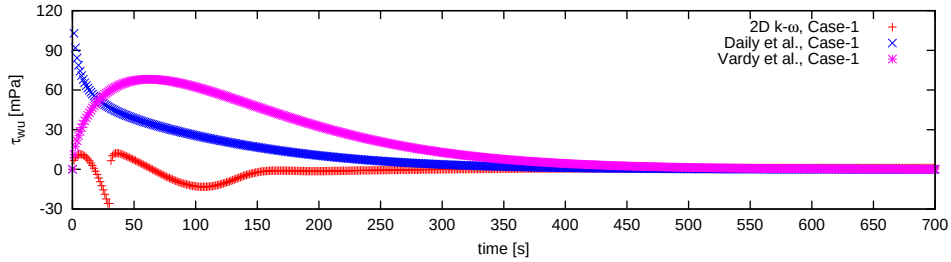

(f) The unsteady component of the wall shear stress from the simulations of Case-1.

Figure 7.15: Bulk velocity and wall shear stress from the simulations of transient Case-1, with $Re_0 = 10^4$ and $Re_1 = 10^6$.

Quasi-Stationary Friction Model

The quasi-stationary models lacks any transient contribution to the wall shear stress, and therefore, undershoots and overshoots according to the transient behaviour of the wall shear stress in the 2D simulations. The largest errors occurs early in the transients where the quasi-steady wall shear stress ranges from undershooting with $\sim 100\%$ to overshooting with $\sim 85\%$ compared to the 2D wall shear stress, see figures A.4a and A.4a in Appendix A. Moreover, since the average of the unsteady wall shear stress were positive in the simulations, the predicted 1D velocity overshoots throughout the ramp-up simulations, see figures 7.15b on page 80 and 7.16b on page 83.

The quasi-steady friction model predicts unsatisfactory predictions of the wall shear stress at the early stages of the simulated transients. However, a short time after the turbulence diffusion time, the quasi-steady wall shear stress were within 10% of the 2D wall shear stress.

Instantaneous Daily et al. Friction Model

Right after the transients was initiated the wall shear stress predicted by the Daily et al. friction model overshot the 2D wall shear stress greatly. The error at first time step was 1245% in Case-1 simulations and almost 1600% in Case-2 simulations, see e.g. figures A.2a and A.4a in Appendix A. The overshooting reduces rapidly as the acceleration and the shear decay coefficient decreases, see figures 7.16f and 7.16f. After the minimum of the 2D wall shear stress the difference between the 1D and 2D wall shear stress decreases, first from above then from below (relative to the 2D wall shear stress). The wall shear stress overshooting in the first stage of the transients, caused the Daily et al. friction model bulk velocity to undershoot the 2D bulk velocity in the same period.

The Daily et al. friction model has no time dependency and does not capture any rise time or turbulence delays. The model's Brunone coefficient was derived based on the assumption of frozen turbulence viscosity during the transient, and that the acceleration is constant for a sufficient amount of time defined by the rise time (2.61),

$$\psi_{TL} = 3.323C^*. \tag{7.5}$$

Turbulence profiles from the 2D simulations revealed that the viscosity is indeed frozen, but only for a short amount of time. Moreover, the acceleration in the ramp-up simulations were fairly constant, see Figure 7.8, but the rise time were longer than the duration of the transients, see Table 7.4 and Figure 7.13c, making the instantaneous acceleration model a poor approximation at early stages of fast ramp-up cases.

Vardy et al. Weighting Friction Model

The Vardy et al model captures the initial rise in unsteady wall shear stress well, but it overshoots when energy is transferred from inertial forces to first turbulence production and later to increased turbulence viscosity. Vardy et al. [29] pointed

out that the frozen viscosity assumption "cannot be valid over large time scales because the flow must adjust to the evolving conditions". The viscosity increases in an annulus near the wall after approximately 2.5s in Case-2, decreasing the accuracy of the model.

The weighting model is superior to both the instantaneous friction model and the quasi-steady friction model during the initial rise of wall shear stress in the transients. This was also at the time which the turbulent viscosity remained approximately constant.

The Vardy et al. friction model includes time dependency, but the model do not account for any turbulence effects after the turbulence increases in the transients. The model does not predict any of the characteristic time scales, however it may be possible to superimpose the effects of the delayed turbulence response described by e.g. the turbulence diffusion time and the turbulence production delay time.

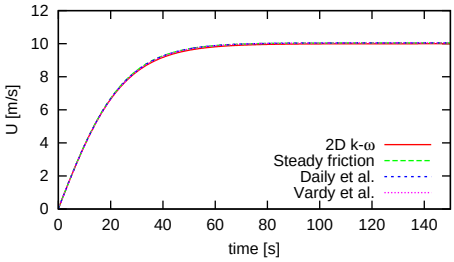

(a) Bulk velocity versus time from Case-2

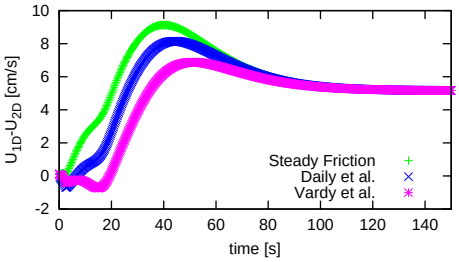

(b) Difference in bulk velocity between the 2D k-ω model and the 1D models

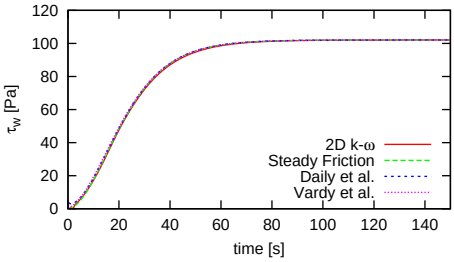

(c) Wall shear stress versus time from Case-2.

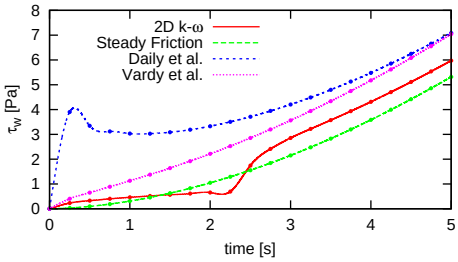

(d) Wall shear stress development in the first period of Case-2 simulations

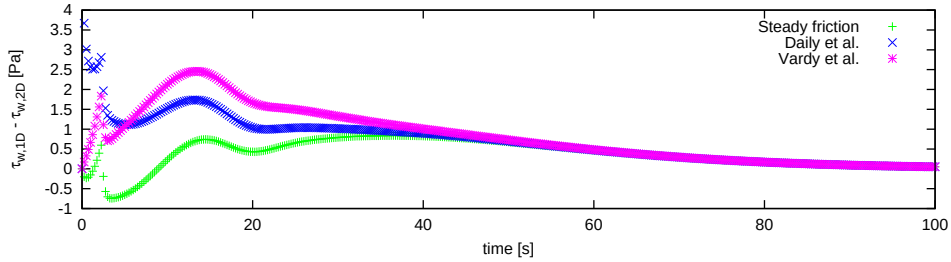

(e) Difference between 1D and 2D wall shear stress.

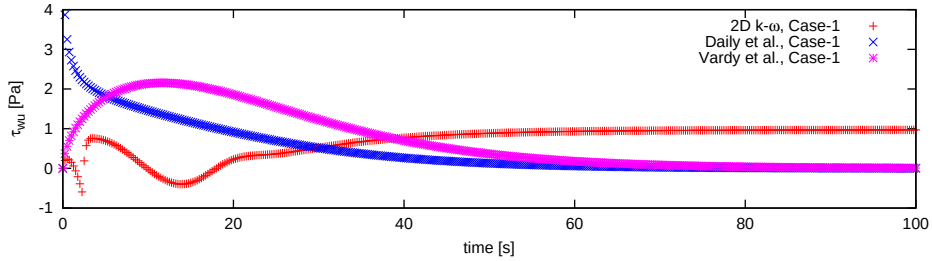

(f) The unsteady component of the wall shear stress from the simulations of Case-2.

Figure 7.16: Bulk velocity and wall shear stress from the simulations of transient Case-2, with $Re_0 = 2 \cdot 10^4$ and $Re_1 = 10^7$.

7.2.5 Section Summary

The 2D wall shear stress exhibit significant transient contribution compared to quasi-steady wall shear stress. The transient contribution is mainly caused by deformation of the velocity profile due to inertia forces and turbulence dynamics. Four turning points of the unsteady component were identified, whereof, three was directly linked to turbulence delays, namely the turbulence diffusion time, T_d, and the turbulence production delay, T_p.

All the 1D models predicted velocity close to the bulk velocity predicted by the 2D k-ω model; the largest error was at the start of the transients, caused by the 2D model's inaccuracy. The transient 1D friction models can only model positive unsteady component of the wall shear stress, and are mostly governed by the acceleration and could not predict the varying wall shear stress observed in the 2D flow.

7.3 Ramp-down Transients in Smooth Pipes

Three decelerating transient cases, referred to as Case-4, Case-5, and Case-6, have been simulated. Case-4 is from Reynolds number 10^6 to 10^4, Case-5 and -6 are from Reynolds number 10^7 to $2 \cdot 10^4$. Transient Case-4 and -5 has a diameter of 1m and Case-6 has a diameter of 0.01m, see Table 7.5. Initial fluid parameters and end solution parameters are tabulated in Table 7.6. The end solution's mean velocities and wall shear stresses was as expected from stationary results indicating that the simulations has converged to steady state flows, see Table 7.6 and Figure 6.4a.

Table 7.5: Table containing key parameters of the ten different turbulent transient cases simulated in this thesis.

Case	Re_0	Re_1	D	k	Δt	Flow time
4	$1 \cdot 10^6$	$1 \cdot 10^4$	1 m	0	1 s	24000 s
5	$1 \cdot 10^7$	$2 \cdot 10^4$	1 m	0	0.5 s	21000 s
6	$1 \cdot 10^7$	$2 \cdot 10^4$	0.01 m	0	0.5 µs	1.5 s

When simulating the ramp-down flows with Fluent it was intended to use NITA, (Non Iterative Time Advancement), but the NITA method tended to make the solver diverge. For the ramp-down from $Re = 10^6$ a stable solver was obtained when the time step $\Delta t < 0.05$ s and relaxation parameters was set to stop potential divergence. This would require at least 420000 time steps before reaching steady state. Therefore NITA was replaced by normal time advancement, making bigger time steps possible and reducing the total number of iterations and thus reducing the computation time.

Table 7.6: Start and end uncertainty between two-dimensional k-ω and one-dimensional steady-state analysis. The one-dimensional steady-state analysis serves as the reference.

Transient	Start of simulation		End of simulation	
case	U	τ_w	U	τ_w
4	−0.0411%	−0.000521%	−5.27%	0.840%
5	−0.437%	−0.0233%	−3.54%	0.359%
6	−0.437%	$-1.56 \cdot 10^-5\%$	−3.40%	−0.597%

7.3.1 Observed Flow Behaviour in the Ramp-down Simulations

The first apparent observation is that the ramp-down transients used longer time to converge to its new steady state than the equivalent ramp-up transients, this is the opposite of what was observed in the laminar transient simulations, see figures 7.17, 7.7a on page 68, and 7.1b on page 63. This occurs due to the non-linearity of the friction factor in the turbulent regime; the friction factor is fairly constant

at the high Reynolds numbers and increases toward the end of the ramp-down simulations.

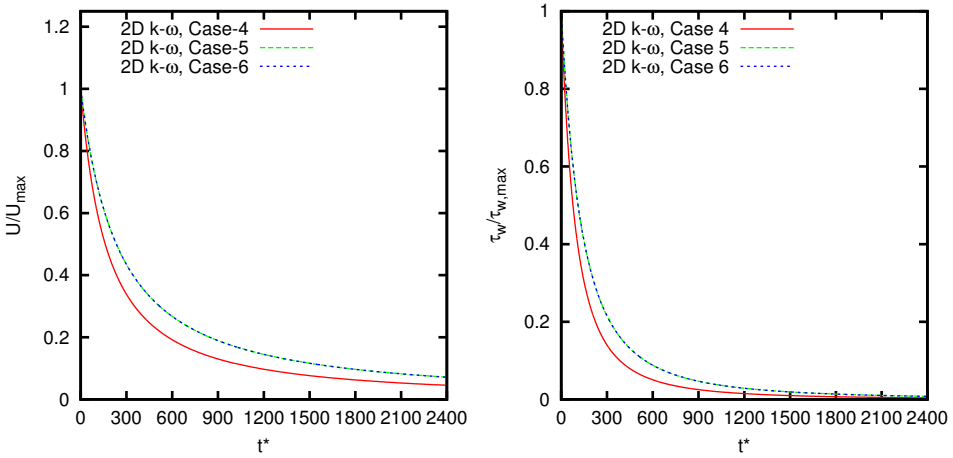

(a) Velocity development.

(b) Wall shear stress development.

Figure 7.17: Bulk velocity and wall shear stress development from the 2D simulations of transient Case-4,-5, and -6. Non-dimensional time is used.

The ramp-down k-ω simulation results showed no apparent sudden changes in the wall shear stress, see Figure 7.17b. However, plotting the unsteady component of the wall shear stress reveals the unsteady behaviour, see top three sub-figures in Figure 7.18 on page 88. Nevertheless, the unsteady component relative to the total wall shear stress is small compared to the ramp-up simulations and converges asymptotically towards $\sim 10\%$ and $\sim 6\%$ of the total wall shear stress for Case-4, and Case-5 and -6 respectively, see Figure 7.18d. The large τ_{wu}/τ_w at the the end of the transients are caused by the propagating uncertainty from the 2D-model's velocity when calculating the unsteady component.

Even though the unsteady component is smaller than the propagating uncertainty, an idea about the sign and magnitude of the unsteady component can still be found, at least if it is assumed that the uncertainty is dependent upon the Reynolds number according to what was found in Figure 6.4 on page 56. With this in mind, the unsteady component depicted in the three top figures of Figure 7.17b will have a positive offset approximately equal to twice that of the uncertainty in the 2D bulk velocity. At the start of the simulation of transient Case-4 the bulk velocity uncertainty was 0.0411%, yielding a very small offset, see Figure 7.18a. In Case-5 and -6 however, the uncertainty was 0.44% yielding an uncertainty in the unsteady component of $\approx 0.87\%$. This equates to an offset of the unsteady component of the wall shear stress at the start of Case-5, and -6 to 0.87Pa and 0.87kPa respectively.

From the unsteady analysis of the laminar ramp-down cases it was expected that

the unsteady component of the wall shear stress should be negative in the turbulent ramp-down cases. However, this was not the case for the simulated turbulent transients; the Case-4 simulation was the only simulated transient with a clear negative unsteady component in the early stage of the transient. If, however, the propagating uncertainty is considered in Case-5 and -6, it is conceivable that the unsteady component is negative in a short period at the beginning. Furthermore, comparing the velocity development from the 2D simulations with the 1D quasi-steady based model (done in Section 7.3.2) indicates that there exists a negative unsteady component at the start of all the ramp-down simulations. Subsequently, inspecting the unsteady component of the simulations of transient Case-5 and -6 reveals that the first time steps are indeed negative compared to the unsteady component calculated at the steady state condition. Moreover, the 1D-2D model comparing suggest that the initial negative unsteady component of the wall shear stress influences the velocity evolvement greatly.

Calculating the wall shear stress that the 1D model requires to produce the same bulk velocity development as found in the 2D model shows that the the produced unsteady component at the start is negative, and that it remains so for $t^* < 106$ seconds in Case 4, and $t* < 0.1$ in Case-5 and -6, see figures 7.19a and 7.19b. In the ramp-up simulations, the turning points of the 1D-model-equivalent unsteady component of the wall shear stress coincided with the change of sign of the 2D unsteady component. However, since the unsteady component is so much smaller relative to the total wall shear in the ramp-down simulations, the uncertainty becomes more important. Consequently, predicting the change of sign of the 2D unsteady component from the turning points of the 1D-model-equivalent unsteady component of the wall shear stress is not an accurate method. The observed turning points of the unsteady component in figures figures 7.19a and 7.19b may stem from other reasons: E.g. when the 2D and 1D simulations converges towards its steady state condition, which consequently reduces the unsteady component of the wall shear stress and a turning point must be present.

A saw tooth behaviour is observed in the unsteady component of the wall shear stress, see figures 7.21b and 7.21d. The origin of the saw tooth behaviour is not known, but it bear some resemblance with the sudden change in wall shear stress found in the ramp-up simulations; a decrease in the unsteady component followed by a rapid increase. The big difference is that the increase and decrease sometimes follow each other in rapid succession creating the jagged form of the unsteady component. In the ramp-up flow this behaviour was mainly a result of the delay in turbulence production and viscosity, this may also be the case in the ramp-down simulations. However, the fluctuating behaviour is at a very low scale and play very little role in the velocity evolvement; it can therefore most likely be disregarded in any 1D friction models meant for predicting gas mean flow characteristics in the industry. Nevertheless, further investigation into the phenomena might yield useful insight into turbulence behaviour.

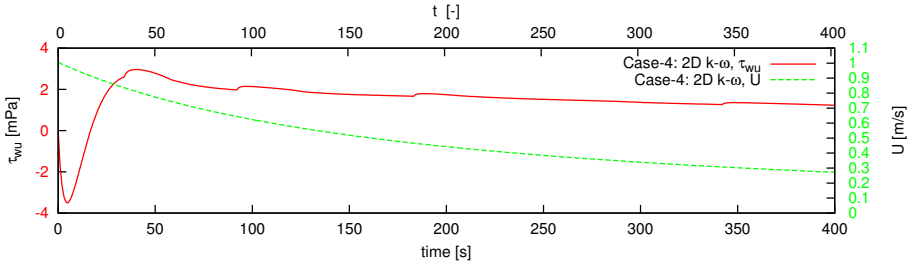

(a) Case-4.

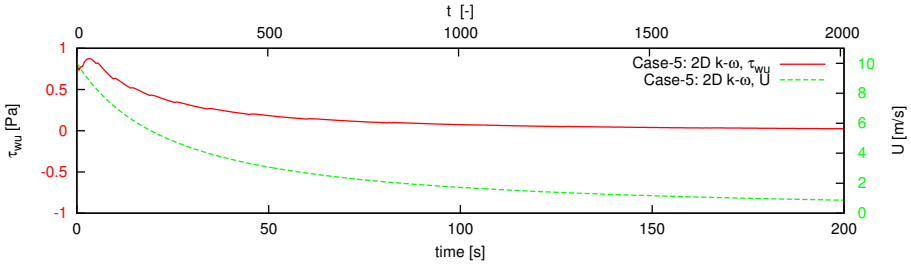

(b) Case-5.

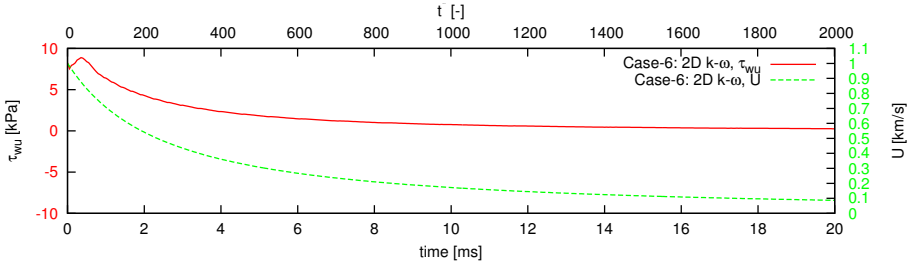

(c) Case-6.

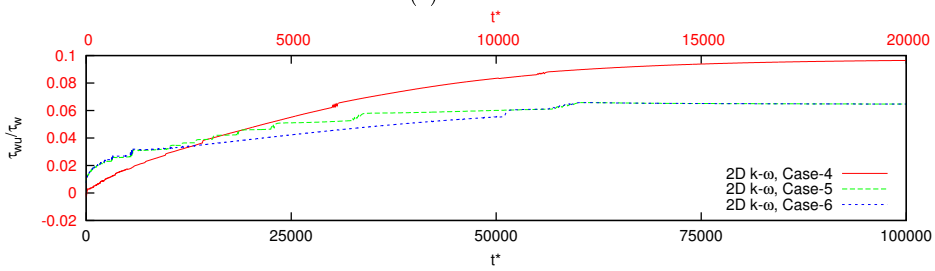

(d) 2D wall shear stress

Figure 7.18: Wall shear stress from the 2D k-ω simulations of the ramp-down transients.

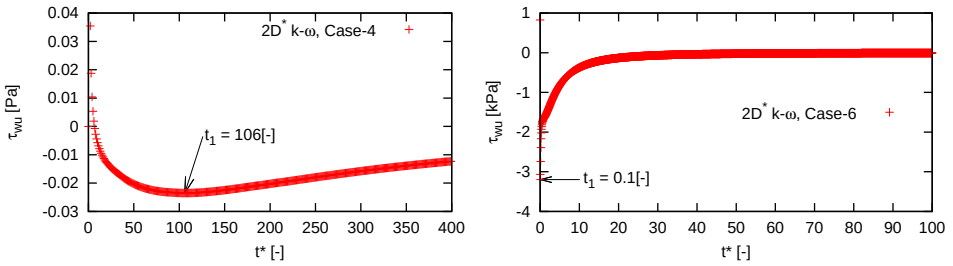

(a) 2D k-ω one-dimensionalized unsteady component of the wall shear stress from Case-4.

(b) 2D k-ω one-dimensionalized unsteady component of the wall shear stress from Case-6.

Figure 7.19: The one-dimensionalized unsteady component. Top figure from Case-4 k-ω simulation and bottom figure from Case-6 k-ω simulation.

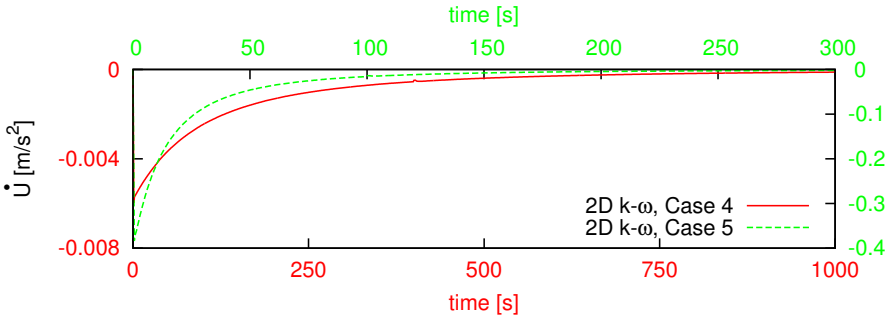

Figure 7.20: Acceleration from 2D k-ω simulation of transient Case-4 and -5.

7.3.1.1 Characteristic Time Scales in the Ramp-Down Simulations

The unsteady component of the wall shear stress have two turning points in the ramp-down cases, two less than in the ramp-up simulations. These turning points does not fit with the calculated turbulence production delay nor the turbulence diffusion time, see Table 7.7, where the turbulence diffusion time and turbulence delay time are tabulated and figures 7.21a and 7.21c, where the characteristic times of the unsteady wall shear stress are marked.

Due to the high Reynolds numbers at the start of the ramp-down transient cases, the turbulence production delay times and turbulence diffusion times are very short compared to the ramp-up cases. The turbulence production delay times were not properly resolved in the ramp-down simulations. Furthermore, the turbulence diffusion times were not fully resolved in the transient simulations of Case-5 and -6. The fact that the ramp-down simulations shows two less turning points than the ramp-up flow can be coupled with the unresolved turbulence production delay, which caused the first two turning points in the ramp-up simulations. It is then natural to deduce that the two existing turning points in the ramp-down simulations were caused by the turbulence diffusion delay and the relation between the turbulence and the excess inertia. However, the turbulence diffusion times does not coincide with the existing turning points of the unsteady wall shear stress; e.g. in the Case-4 simulation the turning points are: $t_1 = 5$s, and $t_2 = 40$s, while the turbulence diffusion time is 18.2s; in the ramp-up simulations, the last turning point t_4 coincided quite accurately with the turbulence diffusion time. It is therefore logical to assume that the last turning point in the ramp-down simulations, t_2, can be related to the turbulence diffusion time, consequently, t_1 is at the time where the relation between excess inertia and turbulence is at an extreme. However, the time of the turning point t_2 was roughly twice that of the turbulence diffusion time in the ramp-down cases. This might be a result of the propagating uncertainty, a coincidence, or perhaps the turning point t_2 is related to the time it takes for the turbulence to propagate from the wall to the wall on the opposite side.

Table 7.7: Rise times and turbulence diffusion times for the different start Reynolds numbers in the ramp-down transient cases.

Case	Re_0	Rise Time	T_d	T_p
1	$1 \cdot 10^6$	91.5s	18.4s	0.68ms
2	$1 \cdot 10^7$	32.7s	2.2s	9.8µs
3	$1 \cdot 10^7$	3.27ms	0.22ms	0.98ns

Profiles from the start of the simulations were extracted to get a better overview of the inertia and turbulence processes transpiring in the ramp-down flows. Unlike in the ramp-up transients the profiles did not show much distortion due to the unsteady flow. Even right after the transient was initiated the velocity profiles deviated little from the universal velocity profile, see figures 7.22b 7.23b.

The radial turbulence delay is barely visible in the turbulence kinetic energy profiles, figures 7.22d and 7.23d. Profiles from the times after the turbulence dif-

fusion time do not exhibit any visible radial turbulence delay. On the other hand, the radial turbulence delay is not prominent in the turbulence viscosity profiles. The turbulence viscosity remains approximately constant for the duration of the turbulence diffusion time, see figures 7.22f and 7.23f.

Generally, the turbulence and velocity profiles from the 2D ramp-down simulations showed small transient behaviour compared to the ramp up-cases. Some of the explanation for this resides in the fact that the turbulence information travels much faster at high Reynolds numbers than low; the turbulence delay is almost non-existing. In addition, there was no visible diverting of energy from the acceleration to turbulence, see the acceleration in Figure 7.20.

The Ramp-down simulations performed by Seddighi et al. [25] the unsteady wall shear component started off negative for a short time and then it was positive for the remainder of the transient, this was also the result in the constantly decelerating simulation done by Ariyaratne et al[5]. As seen above, this was the result found in the simulation of transient Case-4. For the transient Cases-5 and -6, however, this is not as clear, but when accounting for the propagating uncertainty, it can be argumented to some degree of certainty, that the same is the case for the latter two transient cases.

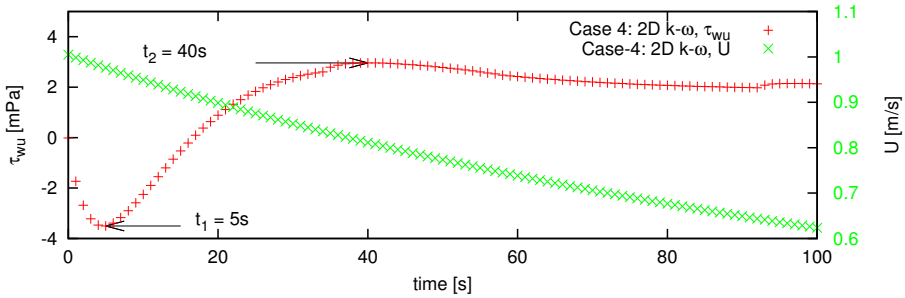

(a) Characteristic times from Case-4.

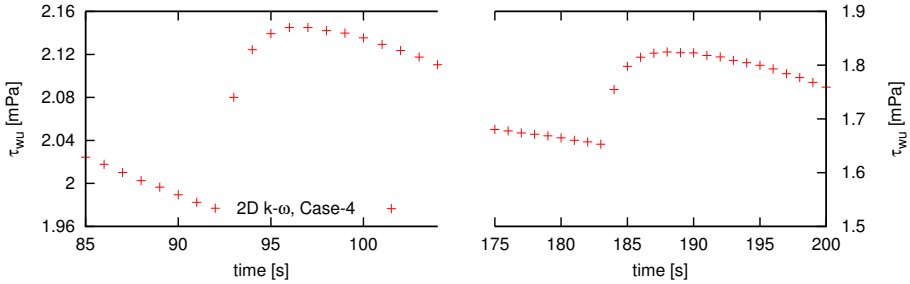

(b) Case-4 Wall shear stress behaviour.

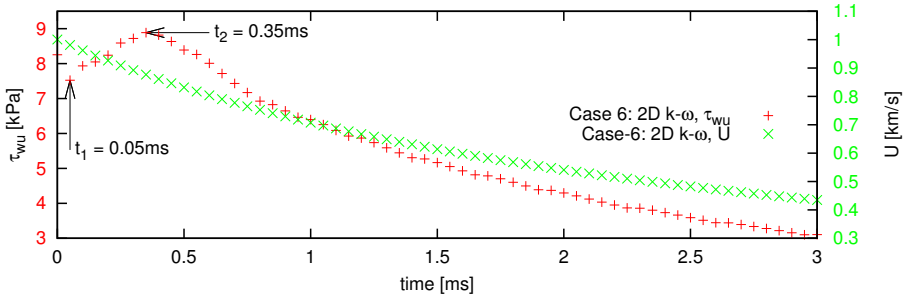

(c) Characteristic times from Case-6.

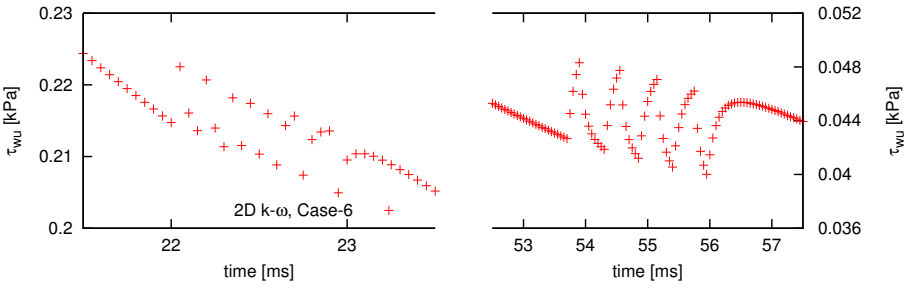

(d) Case-6 Wall shear stress behaviour.

Figure 7.21: Wall shear stress development

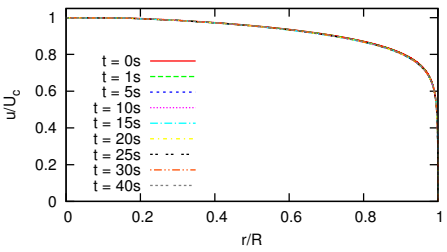

(a) Velocity profiles.

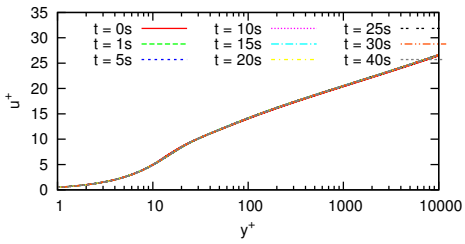

(b) Universal velocity profiles.

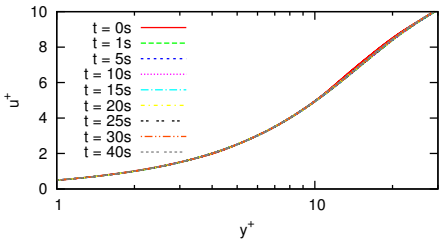

(c) Universal velocity profiles close to the wall.

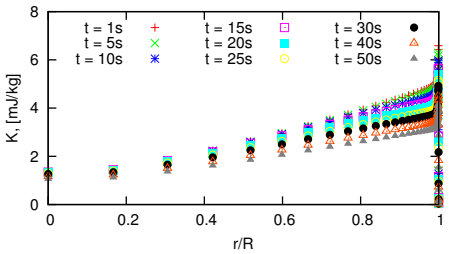

(d) Turbulence kinetic energy profiles.

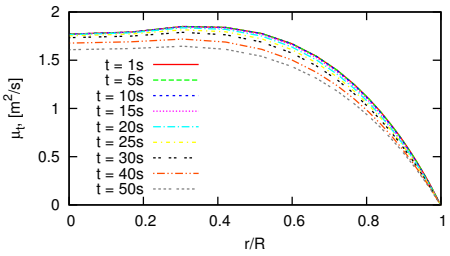

(e) Turbulence viscosity profiles.

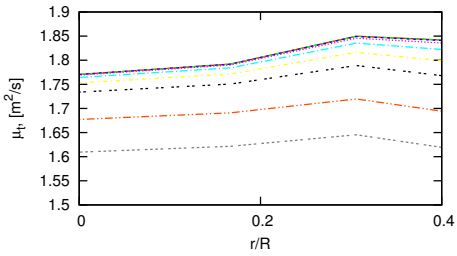

(f) Turbulence viscosity profiles zoomed in to better see the viscous turbulence delay.

Figure 7.22: Velocity and turbulence profiles from 2D simulation of transient Case-4, where $Re_0 = 10^6$ and $Re_1 = 10^4$.

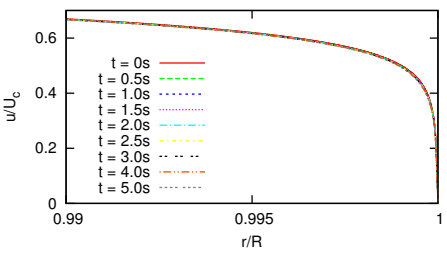

(a) Velocity profiles.

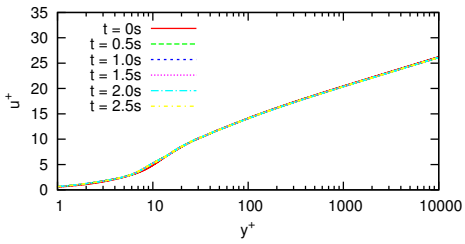

(b) Universal velocity profiles.

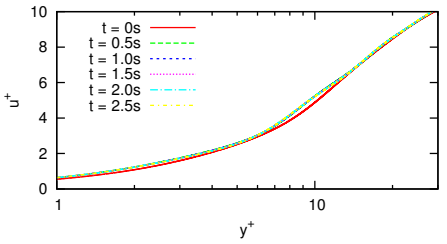

(c) Universal velocity profiles close to the wall.

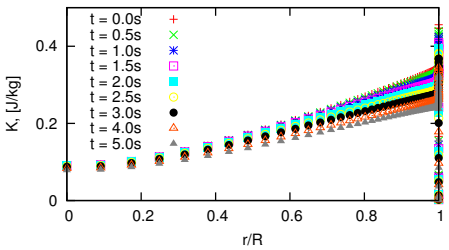

(d) Turbulence kinetic energy profiles.

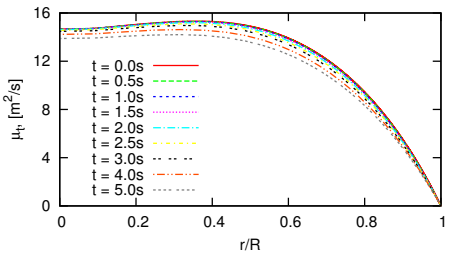

(e) Turbulence viscosity profiles.

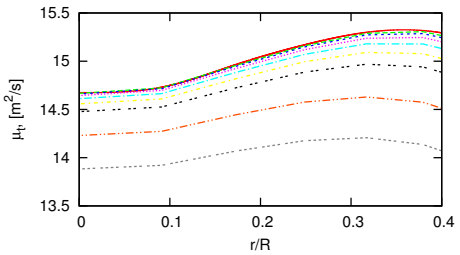

(f) Turbulence viscosity profiles zoomed in to better see the turbulence delay.

Figure 7.23: Velocity and turbulence profiles from 2D simulation of transient Case-5, where $Re_0 = 10^7$ and $Re_1 = 2 \cdot 10^4$.

7.3.2 Performance of the 1D Models in Ramp-Down Transients

This section treats the performance of the three 1D friction models compared to the 2D k-ω simulations of the ramp-down transients considered in this thesis. Figures comparing the results are divided into three main figures, one for each case, where the subset of figures depict the same physical parameters. The sub-figure layout is as follows: Top left shows the velocity development, top right shows the difference in velocity, middle left shows the wall shear stress development, the middle right shows a zoomed in version of the same at the start of the transients, the second from the bottom shows the wall shear stress difference, and the last shows the unsteady component of the wall shear stress. Case-4 figures are found on page 97, Case-5 on page 98, and Case-6 figures are presented on page 99.

Despite that the 2D unsteady component of the wall shear stress is mostly positive, it is assumed as discussed in the previous section, that it is negative in the beginning, and that the initial positive unsteady component is a result of the propagating uncertainty from the bulk velocity undershooting residing in the 2D k-ω model.

Even though the ramp-down 2D simulations showed relative small unsteady wall shear stress behaviour, the 1D models velocity predictions have greater errors than in the ramp-up transients. The errors between the 2D model and the 1D models velocities were largest at the latter part of the transients, around the time when the velocity has reached $\sim 0.25U_0$.

7.3.2.1 Quasi-Stationary Friction Model

With no transient behaviour included, the quasi-stationary friction model predicts a too high wall shear stress in the beginning and thus a too low velocity. The lower unsteady wall shear stress of the 2D simulations causes after a while large errors between the 2D simulations and the 1D quasi-steady simulations. At the maximum the error in velocity is $\sim 20\%$ and for the wall shear stress it is $\sim 35\%$, see figures A.5, A.6, and A.7 in Appendix A. The velocity errors are significantly higher in the ramp-down cases than in the corresponding ramp-up simulations, where the velocity error during the transients were below 6%. However, the wall shear stress error is lower in the ramp-down cases compared to the ramp-up cases. This can be explained by that in turbulence flow the friction factor is not linear to the Reynolds number, the rate of change decreases with increased Reynolds number. Consequently, a change in the friction factor at high Reynolds number influences the flow more than the same change in friction factor at a lower Reynolds number. Thus, the initial unsteady wall shear stress of the 2D flow influences greatly the transient flow, inducing large error in the velocity between the 1D model and the 2D model. Additionally, the larger error in wall shear stress is mostly a result of the different prediction of velocities; the unsteady component of wall shear stress in the 2D ramp-down simulations are below the uncertainty, see Figure 7.18d.

The Quasi-Steady friction model yields unsatisfactory velocity predictions for

the ramp-down transients. The simulations suggests that any transient behaviour at high Reynolds numbers are especially important to achieve an accurate transient model.

7.3.2.2 Daily et al. Friction Model

The Daily et al. friction model starts with overpredicting the magnitude of the unsteady component of the wall shear stress, rendering a too low wall shear stress in the beginning of the transients. Since the 2D wall shear stress converges relatively quick towards a quasi-steady state, the Daily et al. wall shear stress continues to undershoot the 2D wall shear stress for a long period of time. The undershooting does not influence the velocity prediction, since the velocity in the 1D models is only dependent upon the local parameters. Subsequently, the velocity predicted when the Daily et al. friction model was applied closely resembles the 1D model with quasi-steady friction modelling, the velocity is changed by the amount the local unsteady wall shear stress and time dictates.

The rise time is much shorter in the ramp-down cases than in the ramp-up cases. However, the rise time is several magnitudes larger than the chosen time step of the simulations. This renders the Daily et al. friction model unsatisfactory at the beginning of the transient, neglecting any delay in the inertia forces.

Nevertheless, the use of an instantaneous based friction model is more appropriate at high Reynolds numbers; the rise time reduces with increased Reynolds number. However in the case of turbulence and large difference between the initial Reynolds number and the end Reynolds number in a transient (as the case have been in this work), the unsteady component of the wall shear stress cannot merely be a function of the local Reynolds number and the acceleration. In any case, adjustment can easily be made to calibrate an IAB in order to fit existing data and can thus be readably implemented into transient gas transport models, likely with greater success than in ramp-up transients.

7.3.2.3 Vardy et al. Model

Since the Vardy et al. friction model accounts for the rise time, the unsteady wall shear stress modelling is slightly better than the simpler Daily et al. friction model. However, the modelled unsteady component of the wall shear stress surpasses that of the Daily et al. model after a short time and remains larger for the remainder of the simulated ramp-down transients. Although more sophisticated than the Daily et al. friction model, the turbulence delays nor the turbulence forces occurring thereafter are not in any way modelled by the Vardy et al. model. These are parameters affecting the unsteady component in the opposite direction than the inertia forces, i.e. the modelled wall shear stress/friction factor is exaggerated compared to the 2D modelled counterparts.

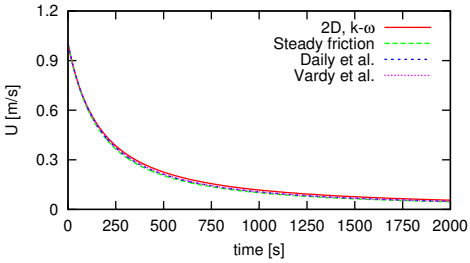

(a) Bulk velocities from simulations of transient Case-4.

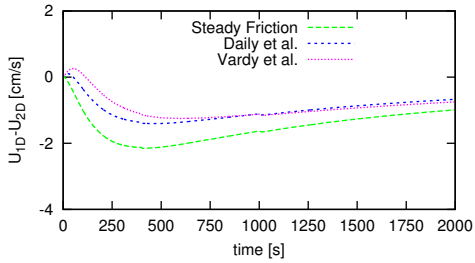

(b) Velocity differences between the 1D models and the 2D model. The velocity is in cm/s.

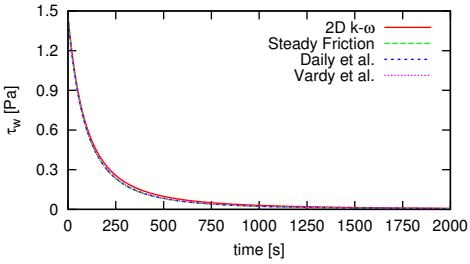

(c) Wall shear stress from simulations of transient Case-4.

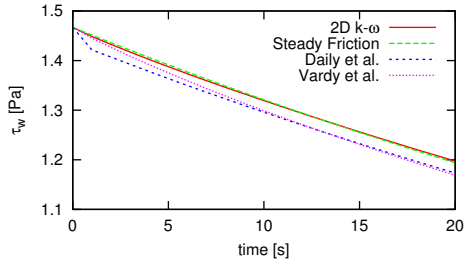

(d) Wall shear stress at the beginning of the transient.

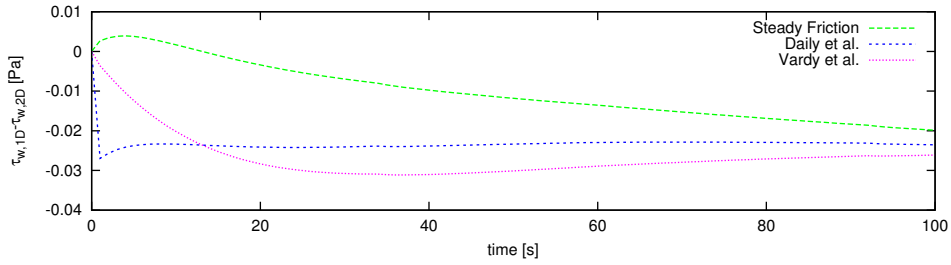

(e) Differences in wall shear stress between the 1D models and the 2D model.

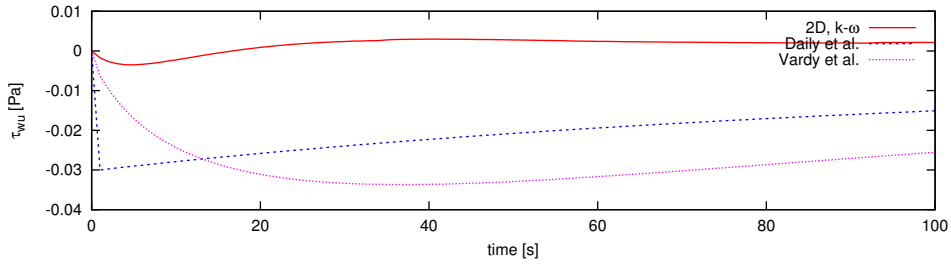

(f) τ_{wu} from the different models.

Figure 7.24: Velocity, wall shear stress, and differences between the 1D models and the 2D model from the simulations of transient Case-4.

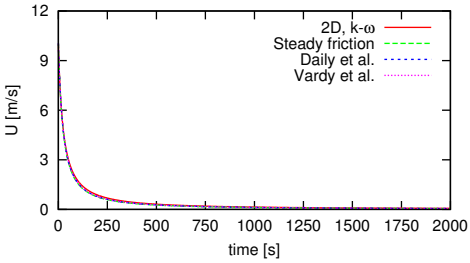

(a) Bulk velocities from simulations of transient Case-5.

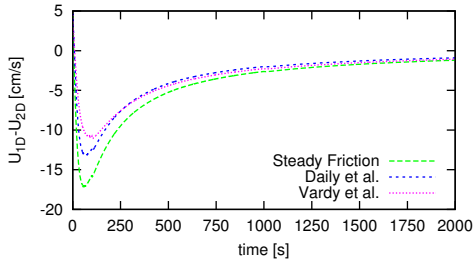

(b) Velocity differences between the 1D models and the 2D model. The velocity is in cm/s.

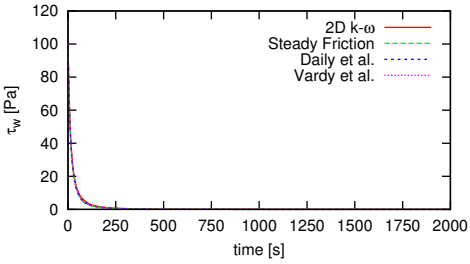

(c) Wall shear stress from simulations of transient Case-5.

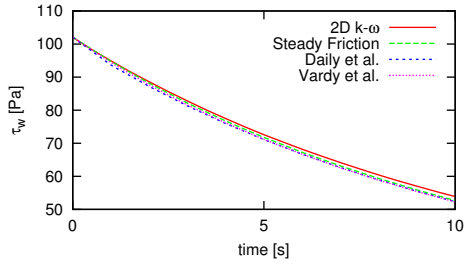

(d) Wall shear stress at the beginning of the transient.

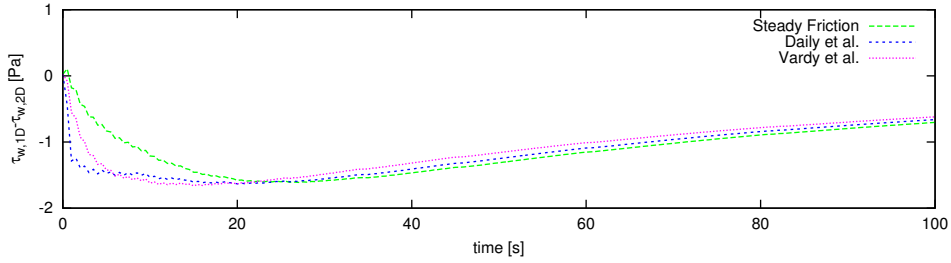

(e) Differences in wall shear stress between the 1D models and the 2D model.

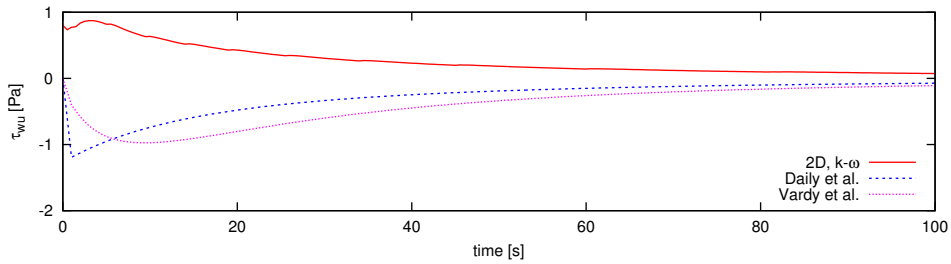

(f) τ_{wu} from the different models.

Figure 7.25: Velocity, wall shear stress, and differences between the 1D models and the 2D model from the simulations of transient Case-5.

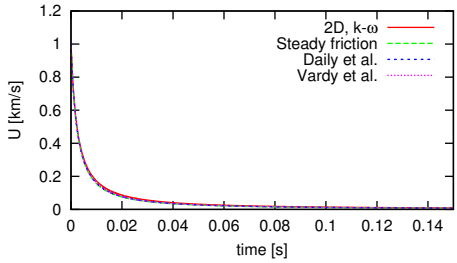

(a) Bulk velocities from simulations of transient Case-6.

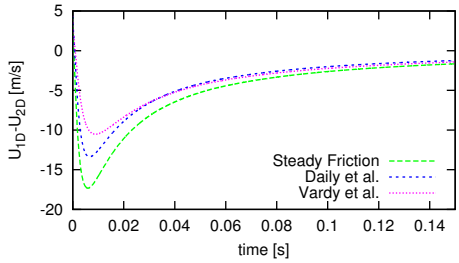

(b) Velocity differences between the 1D models and the 2D model. The velocity is in cm/s.

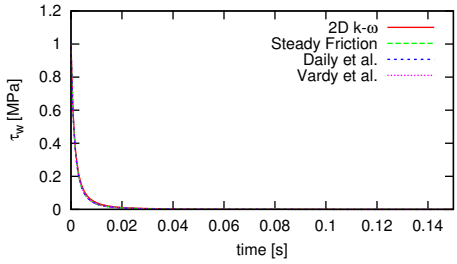

(c) Wall shear stress from simulations of transient Case-6.

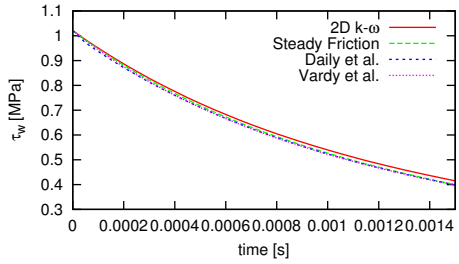

(d) Wall shear stress at the beginning of the transient.

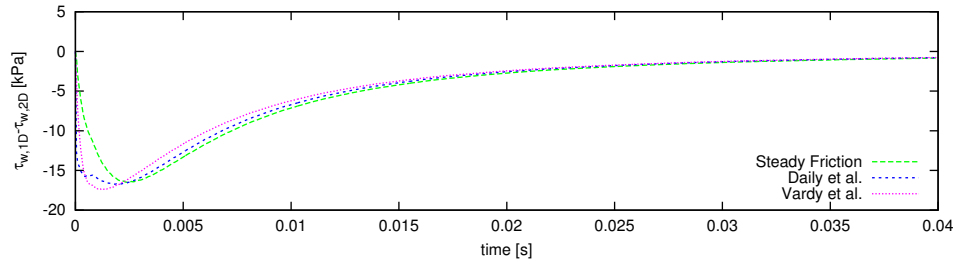

(e) Differences in wall shear stress between the 1D models and the 2D model.

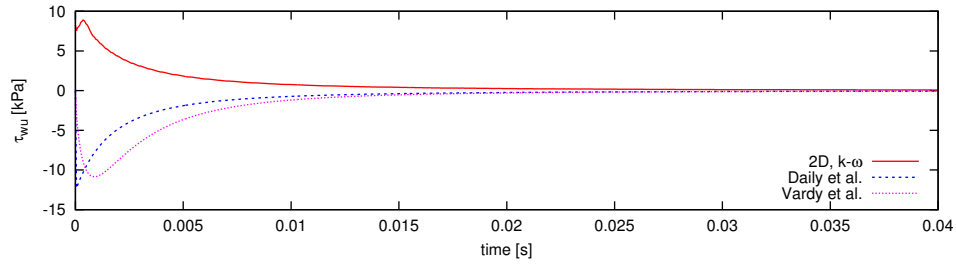

(f) τ_{wu} from the different models.

Figure 7.26: Velocity, wall shear stress, and differences between the 1D models and the 2D model from the simulations of transient Case-6.

7.3.3 Section Summary

The ramp-down flows showed relatively small transient behaviour both on the velocity profiles and the wall shear stress. The unsteady component of the wall shear stress was smaller than the uncertainty of the 2D model. This made it difficult to determine the sign of the unsteady component of wall shear stress, especially in Case-5 and -6. However, there were several indications that the average unsteady component was generally negative in the ramp-down simulations.

The unsteady component of the wall shear stress from simulation of Case-4 showed clear turning point, however these did not transpire at the times calculated from the turbulence production delay or the turbulence diffusion time. In addition, the turbulence production delay time was not fully resolved in the ramp-down 2D simulations, causing any transient behaviour at that time scale to be lost.

Even though the 2D wall shear stress was close to the quasi-steady wall shear stress, the the predicted velocity from the 1D models differs greatly, with errors up till 20%. The importance of correctly predicted wall shear stress at the start of a high Reynolds number ramp-down transient is evidently very important.

The unsteady friction models predicted a too big unsteady component of the wall shear stress compared to the 2D model's.

7.4 Ramp-up and Ramp-down Transients With Wall Roughness

There have been simulated four transients in pipes with finite roughness height at the wall, two accelerating and two decelerating, see Table 7.6. The wish was to simulate flow in the transitional roughness regime, $4 < k^+ < 60$. This proved difficult due to conflicting mesh resolution demand and restriction; the viscous sublayer should be resolved to achieve good accuracy, and the area to where the roughness extend, cannot be resolved. Achieving these two conditions at the same time within the transitional regime was not possible. Case-7 and -9 has $k^+_{max} = 0.65$, making it possible to resolve the viscous sublayer, achieving the same accuracy as with smooth wall, but the flow is regarded as hydraulically smooth, as k^+ is below four. In Case-8 and -10 the k^+_{max} is 3.4 and the flow is nearly in the transitional roughness regime, but the viscous sublayer is not properly resolved when $y^+ \gtrsim 3$ leading to reduced model accuracy and velocity overshooting when comparing to similar 1D flow. The development of y^+ and k^+ from case 8 and 10 are shown in Figure 7.27.

From Figure 7.27 it can be assumed that the 2D simulation at the start of transient Case-8 should yield accurate results. Regrettably, the simulation of transient Case-10 will yield large inaccuracy due to insufficient mesh resolution near the wall at the start of the transient. Thus, the results from simulation of Case-10 will likely not give any reliable data regarding transient effects due to wall roughness in ramp-down transients.

Nevertheless, the selected roughness height is within the relative roughness height found in coated gas transport pipes.

Table 7.8: Table containing key parameters of the four turbulent transient cases simulated in pipes with roughness in this thesis.

Case	Re_0	Re_1	D	k	Δt	Flow time
7	$2 \cdot 10^4$	$1 \cdot 10^7$	1 m	2µm	2.5 ms	150 s
8	$2 \cdot 10^4$	$1 \cdot 10^7$	1 m	10µm	2.5 ms	200 s
9	$1 \cdot 10^7$	$2 \cdot 10^4$	1 m	2µm	0.5 s	22000 s
10	$1 \cdot 10^7$	$2 \cdot 10^4$	1 m	10µm	0.5 s	22000 s

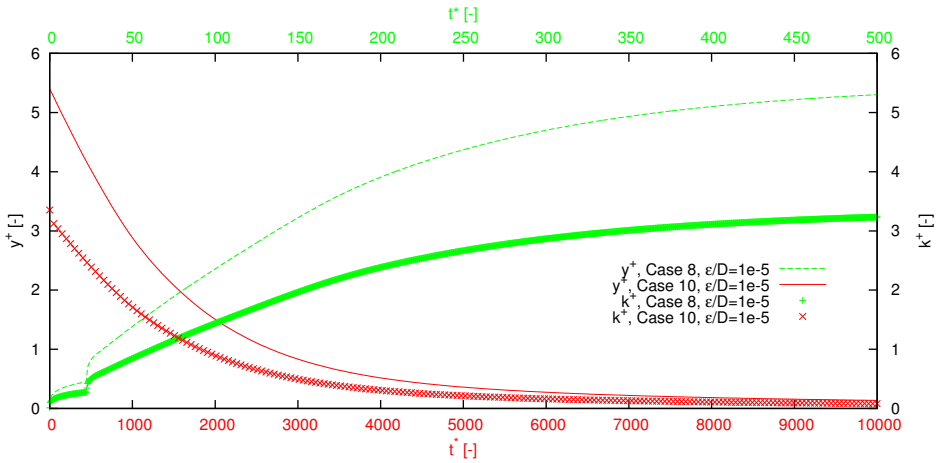

Figure 7.27: y^+ and k^+ development from case 8 and 10. The y^+ curves are shown with lines, while the k^+ curves are shown with points. In addition, the Case-8 data and time-axis are coloured green and the Case-10 data is coloured red

7.4.1 Ramp-up Transients

In this section the results from the ramp-up transients with finite roughness are treated. Firstly the 2D simulations are compared to the corresponding 2D ramp-up simulation without wall roughness. Secondly, the the 1D friction models are compared to the 2D simulations.

The velocity overshooting in Case-8, from the poorly resolved viscous sublayer, is evident in Figure 7.28a where both Case-7 and -8 Reynolds number versus non-dimensional time are shown. In addition to the velocity overshooting, the wall shear stress overshoots the 1D predicted wall shear stress in Case-8, see Figure 7.28b. However, as mentioned in the previous section, it is assumed that the Case-8 2D simulation yields results with high enough accuracy if $y^+ \gtrsim 3$, which the simulation is if $t^* \gtrsim 120$. The largest transient behaviour is observed when $t^* \sim= 23$, which enables analysis of the most important transient behaviour of Case-8.

To find any transient effects due to the added roughness, results from cases 2, -3, 7, and 8 are compared at times well before the uncertainty of Case-8 increases (the Case-3 simulation is selected at the beginning of the transients instead of the

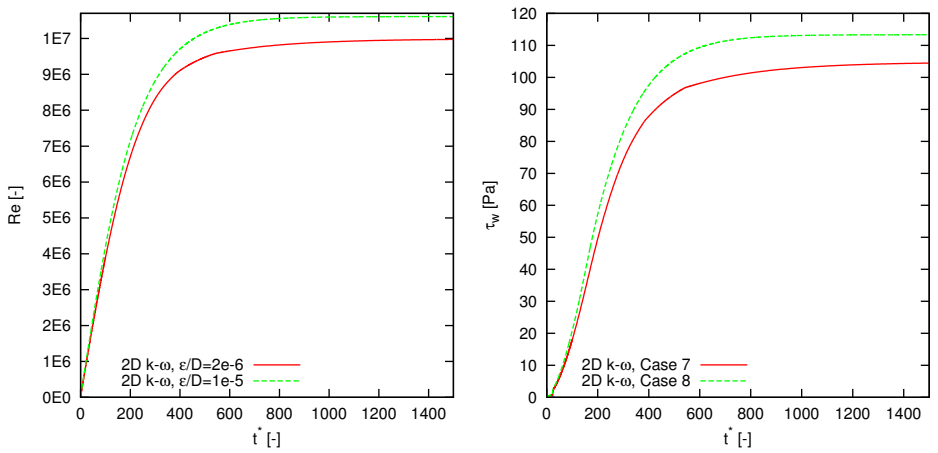

(a) Reynolds number against non-dimensional time from case 7 and 8.

(b) Wall shear stress against non-dimensional time from case 7 and 8.

Figure 7.28: Case 7 and case 8 with $Re_0 = 2 \cdot 10^4$ to $Re_1 = 10^7$ with roughness. In the top Figure 7.28a the Reynolds number is plotted; in the bottom Figure 7.28b the wall shear stress is plotted. Case 7 has a roughness height of 2µm and case 8 has a roughness height of 10µm

Case-2 simulation because of the higher time-step density). Firstly, the unsteady behaviour of the wall shear stress is very similar to what was found in the smooth flow ramp-up simulations. However, the turning point of the unsteady component occurs at earlier times and the unsteady component is at times lower than in the smooth flow. This indicates that there is an increase in turbulence forces, which tend to give an increase in the unsteady component in the negative direction and that the turbulence delays are effected by increase wall roughness. The turbulence diffusion delay,

$$T_d = \frac{D}{\sqrt{2u_\tau}}, \tag{7.3}$$

is inverse proportional to the fourth root of the wall shear stress, and the turbulence production delay,

$$T_p = \frac{\nu}{u_\tau^2}, \tag{7.4}$$

is inverse proportional to the wall shear stress. An increased wall shear stress will reduces both the turbulence delays, albeit, the turbulence diffusion delay is not as strongly dependent upon the wall shear stress as the turbulence production delay. The observed skewed turbulence delay, is that of the turbulence diffusion delay, which seems reasonable according to its prescribed equation.

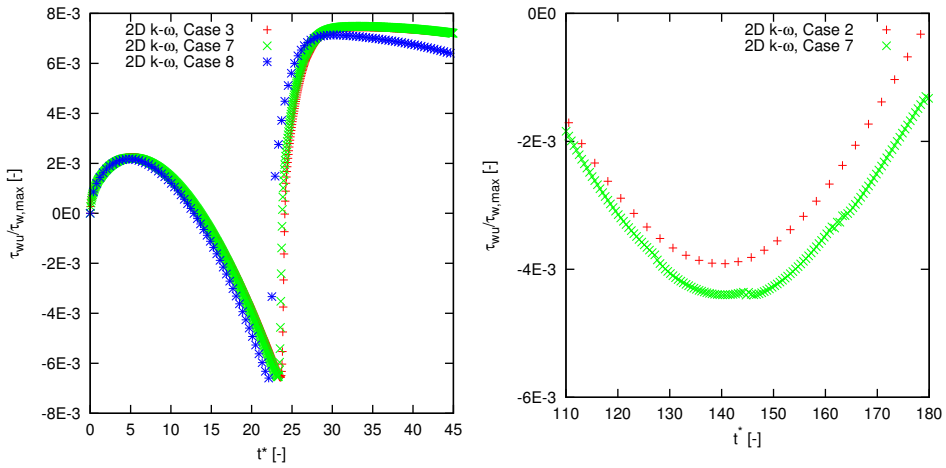

(a) Unsteady component of the wall shear stress relative to the wall shear stress at $Re = 10^7$ versus non-dimensional time.

(b) Unsteady component of wall shear stress divided by the total wall shear stress versus non-dimensional time.

Figure 7.29: The development of the unsteady component of the wall shear stress from ramp-up transient cases 3, 7, and 8 plotted against non-dimensional time.

7.4.2 Performance of the 1D Friction Models in Ramp-Up Transients with Roughness

The transients simulated with wall roughness height never achieve fully rough flow, not even transitional flow is encountered. Therefore, the 1D models with adaptation for fully rough flow is not tested, they are however included in the Fortran code included in the Appendix. The 1D friction models is thus the same as applied in the smooth wall flows, but with increased friction factor due to the imposed wall roughness height.

The wall shear stress development of Case-7 and -8 resembles much what was found in the simulations of smooth flow, so the performance of the 1D models are very similar to what was observed in transient Case-2 and -3. However, the unsteady component of the wall shear stress is at times slightly shifted downward, likely due to increased turbulence dynamics, and the 1D models, thus, displays an increase in wall shear stress error compared to the smooth walled transients.

The error between the 2D and 1D velocities in Case-7 is below the k-ω uncertainty, and the 1D quasi-steady friction model works satisfactory to predict the bulk velocity, see Figure 7.30b. However, if accurate prediction of the wall shear stress is needed for real time surveillance and leak detection, the friction models performs unsatisfactory, see Figure 7.31b

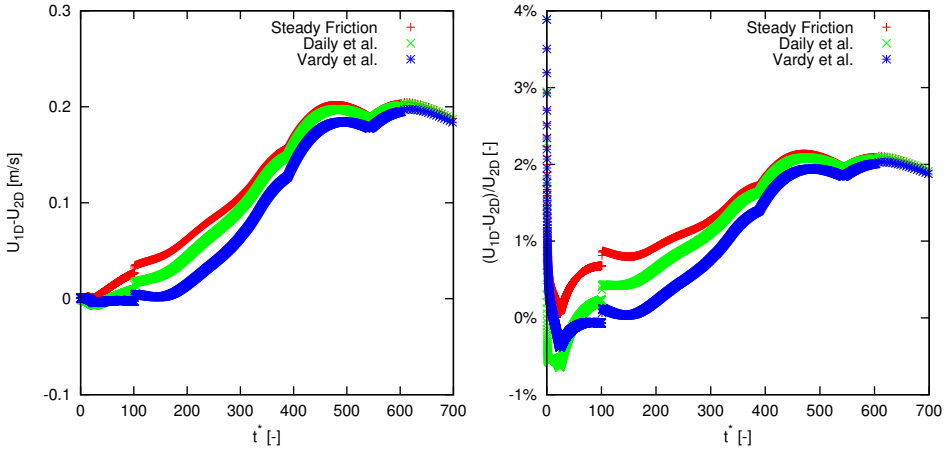

(a) Velocity difference between the 2D model and the 1D friction models.

(b) Difference in wall shear stress between the 2D model and the 1D friction models.

Figure 7.30: Differences between the 2D and 1D models when simulating transient Case-7.

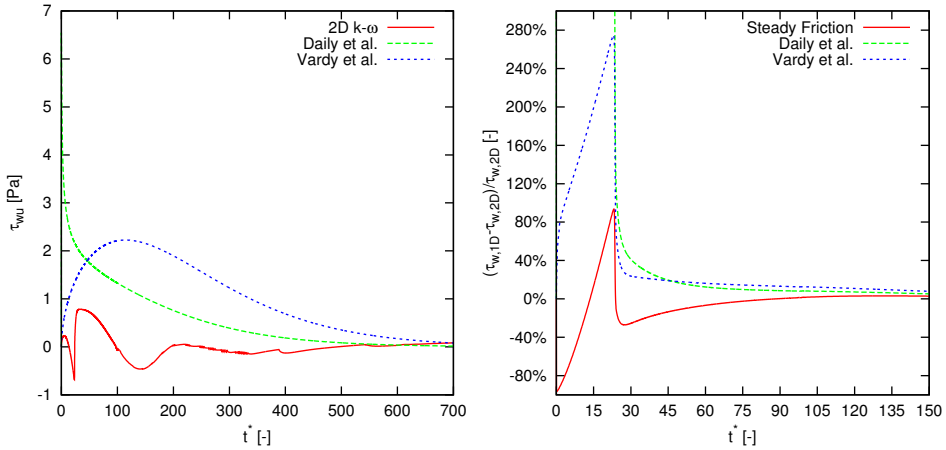

(a) Velocity difference between the 2D model and the 1D friction models.

(b) Difference in wall shear stress between the 2D model and the 1D friction models.

Figure 7.31: Differences between the 2D and 1D models when simulating transient Case-7.

7.4.3 Ramp-down Transients

The ramp-down cases are the same as the ramp-up cases, only with reversed start and end Reynolds number. However, the 2D simulation of the case with roughness height of 10µm has high uncertainty at the beginning of the transient because of the poorly resolved viscous sublayer. In addition to this, the convergence criteria per time step was set larger, 10^{-3}, compared to the other simulations, where it was set to 10^{-6}. Due to the large uncertainty from the poorly resolved viscous layer it was decided that a new simulation was not needed. Nevertheless, the velocity and the wall shear stress from the 2D simulation of transient Case-10 are depicted alongside the results from Case-9 to show the large uncertainty, see Figure 7.32. Results from Case-10 simulations, will however not be compared with the 1D models or the equivalent ramp-down simulations with different wall roughness.

The wall shear stress and velocity development was not greatly effected by the roughness height in the 2D simulation of Case-9. If compared to the smooth walled simulation with same initial and end Reynolds number, Case-5, one can see that the unsteady component is slightly lower in Case-9, see Figure 7.33. The unsteady component is, as in the simulation of Case-5, smaller than the propagating uncertainty. So, claiming that the lower unsteady component is caused by different flow dynamics from the imposed wall roughness cannot be done with certainty; the reduction in unsteady wall shear stress may be a result of altered uncertainties due to the roughness height; the velocity undershooting decreases with increased roughness height, see Figure 6.6a on page 59.

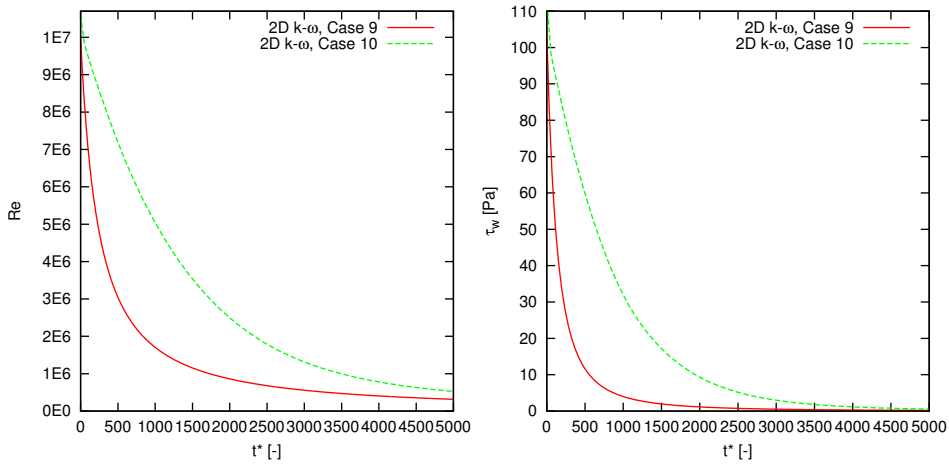

(a) Reynolds number versus non-dimensional time.

(b) Wall shear stress versus non-dimensional time.

Figure 7.32: Reynolds number and wall shear stress versus non-dimensional time from the k-ω simulation of transient cases-9 and 10.

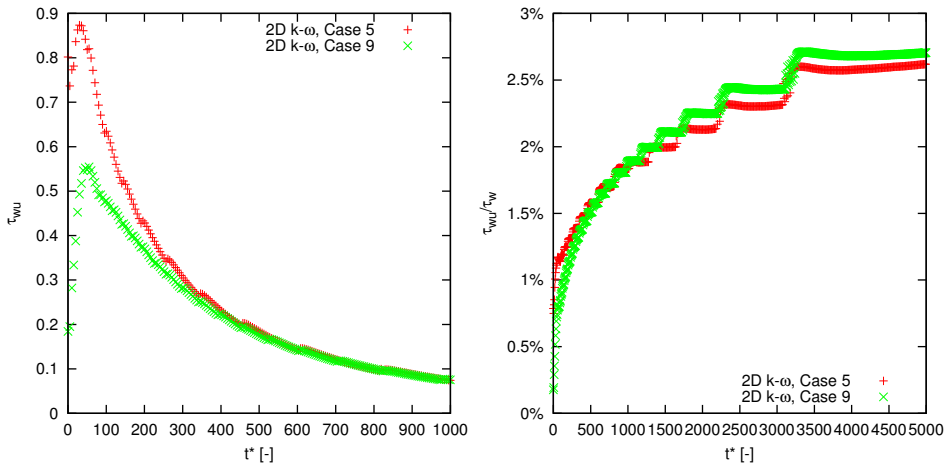

(a) Unsteady component of the wall shear stress versus non-dimensional time.

(b) Unsteady component of wall shear stress divided by total wall shear stress versus non-dimensional time.

Figure 7.33: Wall shear stress development from the 2D simulations of transient Case-5 and -9.

7.4.3.1 Performance of the 1D Friction Models in Ramp-Down Transients with Roughness

Only transient ramp-down Case-9 is considered due to the high uncertainty at the start of the 2D simulation of transient Case-10. The results are similar to the ramp-down simulations in smooth pipes, see Figure 7.34. It is evident that the relative roughness height must be increased to see any real effect of unsteady behaviour on the flow, both with the 2D and 1D models.

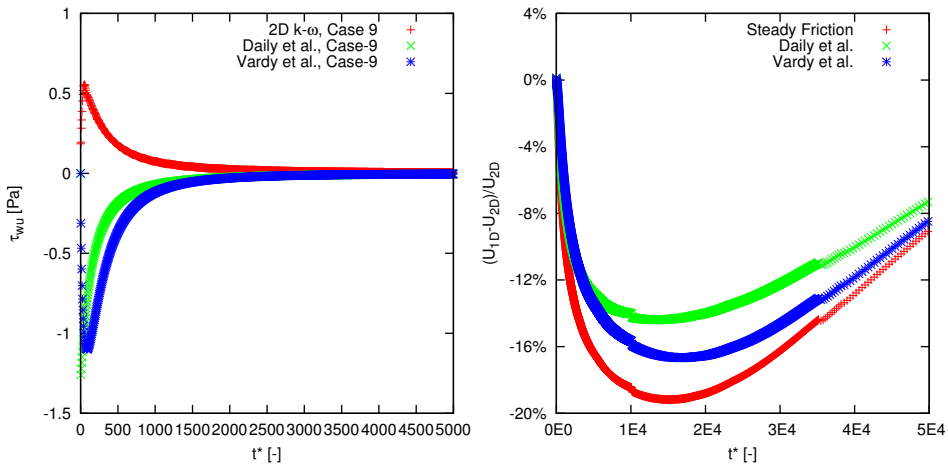

(a) Unsteady component of the wall shear stress.

(b) The velocity difference between the 2D model and the 1D models.

Figure 7.34: Unsteady component of the wall shear stress and velocity difference from the 1D models and the 2D model simulations of Case-9

7.4.4 Section Summary

The roughness height in combination with the resolution of the near wall field criteria was not possible to fulfil. The first part of transient Case-8 could be examined and yield somewhat reliable data on how roughness affects the flow evolvement. The flow was not in the fully rough regime, and therefore the 1D friction models for fully rough flow was not applied. The wall roughness shortened the turbulence delay times and increased turbulence dynamics causing a slightly lower wall shear stress compared to smooth flow. The reduction in turbulence delay times are in conjunction with the turbulence diffusion delay ,T_d, and the turbulence production delay, T_p.

Chapter 8

Conclusion

The scope of this work was to investigate the implication of using a quasi-steady friction factor modelling in 1D gas transport models. Both laminar and turbulence transients were considered. Transients were simulated with detailed 2D models and compared with 1D models with both quasi-steady friction modelling and simple transient friction modelling.

The Turbulence k-ω model had a systematic bulk velocity undershooting compared to 1D analysis. This uncertainty propagated and doubled the uncertainty of the friction factor, and thus, the wall shear stress was extensively used to evaluate the transient behaviour instead of the friction factor.

The laminar transient simulations showed that, in laminar flow, the transient contribution to the wall shear stress was not negligible, and furthermore, that the sign of the unsteady component of the wall shear stress was positive in accelerating flows and negative in decelerating flows. Additionally, the wall shear stress was highest at the beginning of the transients and converged asymptotically towards a quasi-steady state in a smooth manner. The 1D IAB Daily et al. friction model gave higher accuracy predictions compared to the 1D quasi-steady friction model.

The use of quasi-steady friction modelling in the 1D turbulence model, yielded high accuracy when predicting bulk velocity in the ramp-up transients. However, the 2D unsteady wall shear stress deviated greatly from the quasi-steady predictions. Similar characteristic transient wall shear stress behaviour was observed in all the ramp-up flows. Moreover, the turning points of the unsteady component was coupled to two turbulence time scales, namely the turbulence diffusion time and the turbulence production delay.

In the ramp-down simulations the unsteady component of the wall shear stress was small compared to the total wall shear stress, making it difficult to accurately determine the sign of the unsteady component. However, the velocity development showed that the unsteady component was negative at the start of the transients and that a relatively small unsteady component of wall shear stress at high Reynolds numbers, strongly influenced the flow development. In addition, the unsteady be-

haviour caused large differences between the 1D and 2D velocity predictions. Unlike in the ramp-up simulations, the turbulence time scales were not in conjunction with any of the turning points of the unsteady component of the wall shear stress.

Neither of the implemented 1D friction models predicted satisfactory wall shear stress development in the turbulence transients. Furthermore, the large differences between the transient wall shear stress behaviour in the turbulence ramp-up and ramp-down transients, indicates that 1D transient friction models should not treat ramp-up and ramp-down transients similarly (as is the case for the implemented transient friction models). However, the simulations showed that improving the 1D transient friction modelling can significantly improve the accuracy of the 1D transient velocity modelling in the ramp-down cases.

Due to the limited roughness height, the flow in rough walled pipes did not differ significantly from similar simulations with smooth flow. Although, slight changes to the occurrence of the unsteady component's turning points and magnitude were observed in the ramp-up simulations.

8.1 Future Work

Below are some suggestions for what future work can consist of.

- Simulations of transients in the transitional roughness regime should be attempted. As mentioned, the roughness height was limited by the k-ω model mesh demands. This has been solved in Fluent 14, where an equation describing a shift in wall placement has been introduced:

$$y^+ = y^+ + \frac{k}{2} \tag{8.1}$$

  where k is the roughness height. This equation gives a correct displacement of the velocity due to roughness. This removes the restriction to the mesh resolution, so that the mesh can be resolved inside the wall roughness height without deteriorating the solution.

- Adjust the k-ω model constants to increase the accuracy of the 2D model and reduce the velocity undershooting at "low" Reynolds number.

- It is advisable to employ other methods to model the 1D momentum equation, at least if transient friction models are to be validated.

- Investigating the turbulence delayed response and inertial forces with a more detailed RANS model or perhaps DNS. This might give more insight into the transient friction development, and its difference from the quasi-steady friction factor, and may eventually lead to better 1D friction models.

Bibliography

[1] *Modelling of fast transients by numerical methods*, 1991.

[2] Guide for the Verification and Validation of Computational Fluid Dynamics Simulations. *AIAA Std. G-077-1998e*, pages 1–19, 1998.

[3] ANSYS. *ANSYS FLUENT Theory Guide.*

[4] ANSYS. *ANSYS FLUENT User's Guide.*

[5] Chanchala Ariyaratne, Shuisheng He, and Alan E. Vardy. Wall friction and turbulence dynamics in decelerating pipe flows. *Journal of Hydraulic Research*, 48(6):810–821, 2010.

[6] Anton Bergant, Angus Ross Simpsonm, and John Vitkovsky. Developments in unsteady pipe flow friction modelling. *Journal of Hydraulic Research*, 39(3):249–257, 2001.

[7] BP. *BP Statistical Review of World Energy June 2012.*

[8] M. R. Carstens and J. E. Roller. Boundary-shear stress in unsteady turbulent flow. *J. Hyd. Div. Proc. ASCE*, 85:67–81, 1959.

[9] Daily et.al. Resistance coefficients for accelerated and decelerated flows through smooth tubes and orifices. 1956.

[10] Robert W. Fox, Philip J. Pritchard, and Alan T. McDonald. *Introduction to Fluid Mechanics.* Wiley, 7 edition, 2004.

[11] Joachim Dyrstad Gjerde. Transient flow in gas transport, 2011.

[12] S. He, C. Ariyaratne, and A.E. Vardy. A computational study of wall friction and turbulence dynamics in accelerating pipe flows. *Computers & Fluids*, 37(6):674–689, 2008.

[13] S. He and J.D. Jackson. A study of turbulence under conditions of transient flow in pipe. *Journal of Fluid Mechanics*, 408(1):1–38, 2000.

[14] H.B Keller. Accurate difference methods for nonlinear two-point boundary value problems. *SIAM Journal on Numerical Analysis*, 11, 1974.

[15] Leif Idar Langelandsvik. *Modeling of natural gas transportand friction factor for large-scale pipelines : Laboratory experiments and analysis of operational data.* PhD thesis, Norwegian University of Science and Technology, Department of Energy and Process Engineering, 2008.

[16] Torbjørn Lyssand. Transient dynamikk i gasstransport, 2011.

[17] A.S Monin and A.M Yaglom. *Statistical fluid mechanics: mechanincs of turbulence.* MIT Press, first edition, 1971.

[18] Lewis. F Moody. Friction factors for pipe flow. 1944.

[19] Johann Nikuradse. Gesetzmassigkeiten der turbulenten stromung in glatten rohren. 1932.

[20] Nikan Noorbehesht and Pedram Ghaseminejad. Numerical simulation of the transient flow in natural gas transmission lines using a computational fluid dynamic method. *American Journal of Applied Sciences*, 10:24–34, 2013.

[21] Wiliam L. Oberkampf and Frederick G. Blottner. Issues in computational fluid dynamics code verification and validation. Technical report, Sandia National Laboratories, 1997.

[22] Olje- og energidepartementet and Oljedirektoratet. *Fakta 2012 Norsk petroliumsvirksomhet.*

[23] Ivo Pothof. A turbulent approach to unsteady friction. *Journal of Hydraulic Research*, 46(5):679–690, 2008.

[24] Osborne Reynold. An experimental investigation of the circumstances which determine whether the motion of water shall be direct or sinuous, and of the law of resistance in parallel channels. 1883.

[25] Mehdi Seddighi, Shuisheng He, Paolo Orlandi, and AlanE. Vardy. A comparative study of turbulence in ramp-up and ramp-down unsteady flows. *Flow, Turbulence and Combustion*, 86(3-4):439–454, 2011.

[26] Elling Sletfjerding. Friction factor in smooth and rough gas pipelines; an experimental study, 1999.

[27] Roger Temam. *Navier-Stokes equations : theory and numerical analysis.* AMS Chelsea Publishing, 3rd edition, 1984.

[28] A.E. Vardy and J.M.B Brown. Transient, turbulent, smooth pipe friction., 1995.

[29] A.E Vardy and J.M.B Brown. Transient turbulent friction in smooth pipe flows. *Journal of Sound and Vibration*, 259(5):1011–1036, 2003.

[30] A.E Vardy and J.M.B Brown. Transient turbulent friction in fully rough pipe flows. *Journal of Sound and Vibration*, 270:233–257, 2004.

[31] A.E. Vardy, J.M.B. Brown, and S. He. Signs of unsteady skin friction, March 2004.

[32] H. K. Versteeg and W. Malalasekera. *An Introduction to Computational Fluid Dynamics The Finite Volume Method*. Pearson Education Limited, second. edition, 2007.

[33] Frank M. White. *Viscous Fluid Flow*. McGraw-Hill, third edition, 2006.

[34] Frank M. White. *Fluid Mechanics*. McGraw-Hill, sixth edition, 2009.

[35] D. C. Wilcox. Comparison of two-equation turbulence models for boundary layers with pressure gradient. *AIAA JOURNAL*, 31, 1993.

[36] B.H Yan, H.Y. Gu, and L. Yu. Numerical research of turbulent heat transfer in rectangular channels in ocean environment. 2011.

[37] Tor Ytrehus. The governing conservation equations in fluid mechanics. Technical report, DEPARTMENT OF ENERGY AND PROCESS ENGINEERING, NTNU, 2012.

[38] Tor Ytrehus. Oral communication, 2013.

[39] Zbigniew Zarzycki, Sylwester Kudzma, and Kamil Urbanowicz. Improved method for simulating transients of turbulent pipe flow. *Journal of Theoretical and Applied Mechanics*, 49(1):135–158, 2011.

[40] Jun Zhang, Andy Hoffman, Keefe Murphy, John Lewis, and Michael Twomey. Review of pipeline leak detection technologies. 2013.

[41] Werner Zielke. Frequency dependent friction in transient pipe flow. *Journal of Basic Engineering*, 90(3):109–115, 1968.

Appendices

Appendix A

Additional Figures

In this appendix figures depicting the error between 1D and 2D results are presented. The 2D results are considered to predict transient behaviour "correctly" and are therefore treated as the correct value to which the error is evaluated.

A.1 Figures from Case 1

Case 1: Ramp-up from Reynolds number 10^4 to 10^6.

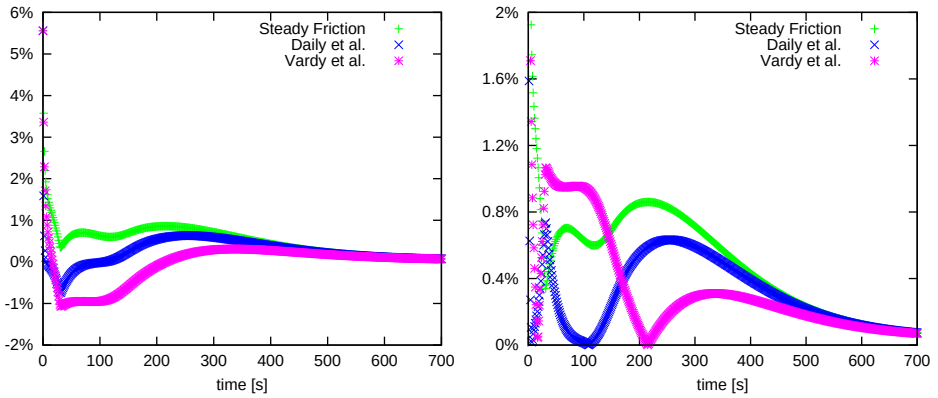

(a) Error in velocity between the 1D models and the 2D model.

(b) Absolute error in velocity between the 1D models and the 2D model.

Figure A.1: Percent error in bulk velocity between the 2D k-ω model and 1D models from Case-1 simulations

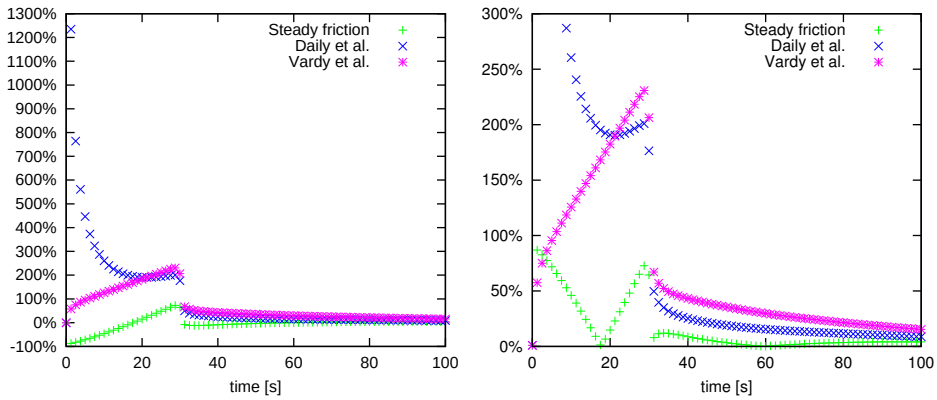

(a) Error in wall shear stress between the 1D models and the 2D model.

(b) Absolute error in wall shear stress between the 1D models and the 2D model.

Figure A.2: Percent error in wall shear stress between the 2D k-ω model and 1D models from Case-1 simulations

A.2 Figures from Case-2

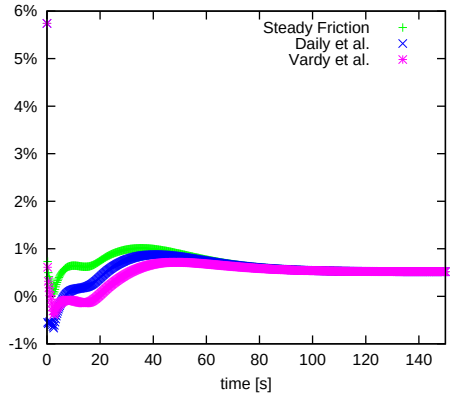

(a) Error in velocity between the 1D models and the 2D model.

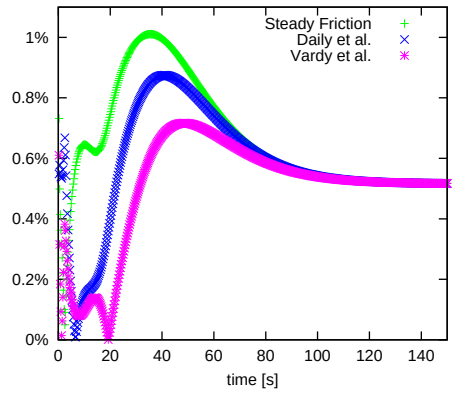

(b) Absolute error in velocity between the 1D models and the 2D model.

Figure A.3: Percent error in bulk velocity between the 2D k-ω model and 1D models from Case-2 simulations

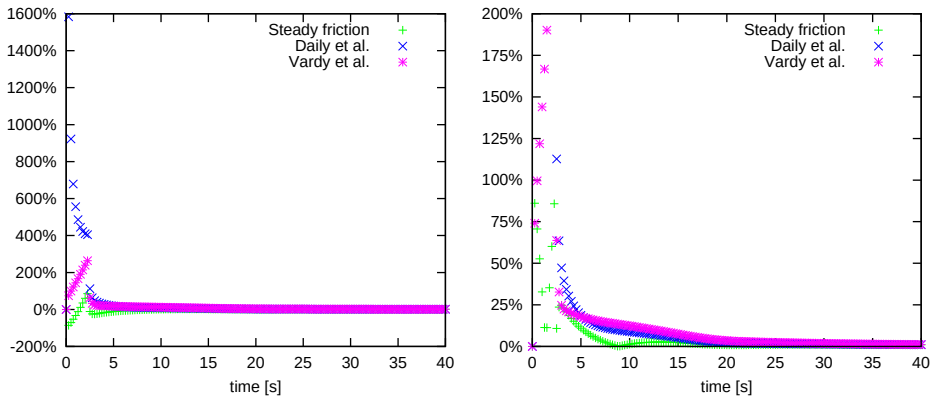

(a) Error in wall shear stress between the 1D models and the 2D model.

(b) Absolute error in wall shear stress between the 1D models and the 2D model.

Figure A.4: Percent error in wall shear stress between the 2D k-ω model and 1D models from Case-2 simulations

A.3 Figures from Transient Case-4

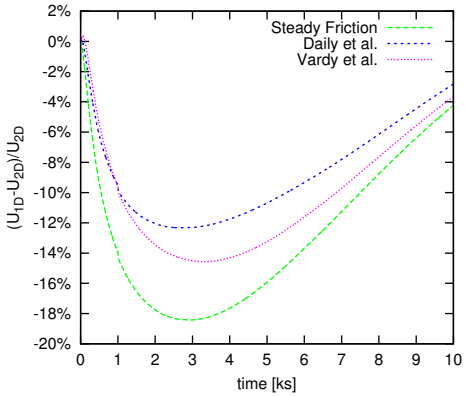

(a) Percent error between 2D and 1D velocities.

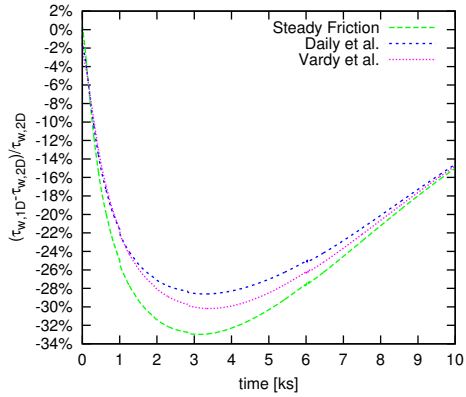

(b) Percent error between 2D and 1D wall shear stress from Case-4 simulations.

Figure A.5: Percent error between the 2D k-ω model and 1D models from Case-4 simulations, left shows the velocity error and the right shows the wall shear stress error.

A.4 Figures from Transient Case-5

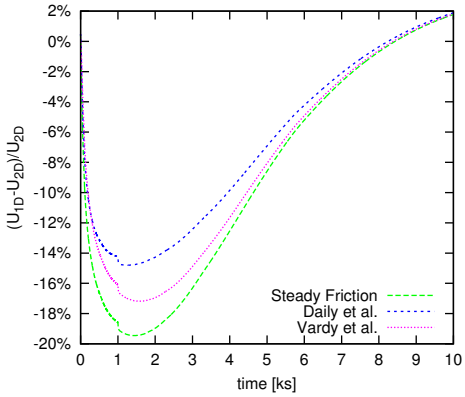

(a) Percent error between 2D and 1D velocities.

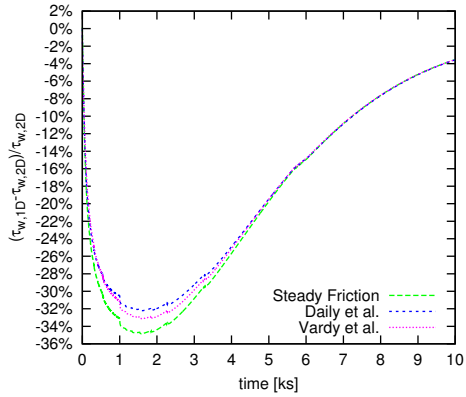

(b) Percent error between 2D and 1D wall shear stress from Case-5 simulations.

Figure A.6: Percent error between the 2D k-ω model and 1D models from Case-5 simulations, left shows the velocity error and the right shows the wall shear stress error.

A.5 Figures from Transient Case-6

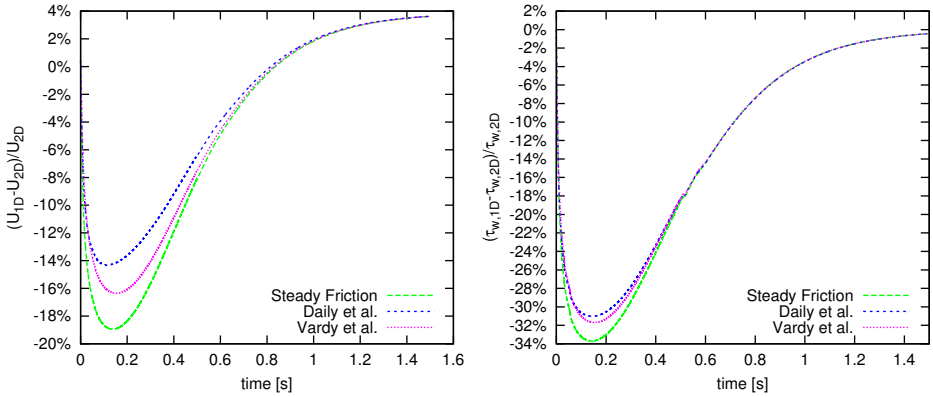

(a) Percent error between 2D and 1D velocities.

(b) Percent error between 2D and 1D wall shear stress from Case-6 simulations.

Figure A.7: Percent error between the 2D k-ω model and 1D models from Case-6 simulations, left shows the velocity error and the right shows the wall shear stress error.

Appendix B

One-Dimensional Model Codes

All the 1D models are included in the code herein.

```
1  !-----------------------------------------------------------------------!
2  !---Program containing 1D turbulent and laminar model for a --!
3  !---cross section of a pipe. Both quasi-steady and unsteady---!
4  !---friction modelling is implemented.-------------------------!
5  !-----------------------------------------------------------------------!
6  !--------------------Sigmund A Birkeland-------------------------!
7  !-----------------------------------------------------------------------!
8  MODULE DECLARATIONS
9  !-----------------------------------------------------------------!
10 !---Variables accesable to all modules that uses statement---!
11 !---"use declarations".-----------------------------------------!
12 !-----------------------------------------------------------------!
13   IMPLICIT NONE
14   PRIVATE
15   DOUBLE PRECISION, PUBLIC, ALLOCATABLE, DIMENSION(:) :: Ut,UT2, Ret, ft, tvector,tau,
         TAUU,TAUS,W,Fu,FS
16   DOUBLE PRECISION, PUBLIC :: eps, D, rho, mu, alpha, tol, frict, beta, Re_start,
         Re_end,MAXF,MINF
17 END MODULE DECLARATIONS
18
19 MODULE SUB
20 CONTAINS
21 SUBROUTINE FRICTION(U)
22 !-----------------------------------------------------------------!
23 !---Input is double precision and velocity, outputs friction---!
24 !---factor-------------------------------------------------------!
25 !-----------------------------------------------------------------!
26   USE DECLARATIONS
27   IMPLICIT NONE
28   DOUBLE PRECISION, INTENT(IN) :: U
29   DOUBLE PRECISION :: Re, epsD, X, XOLD
30   Re = rho*U*D/mu
31   epsD = eps/D
32   X = 1.0
33   XOLD = X+1
34   DO WHILE ( ABS(X-XOLD) > tol)
35     XOLD = X
36     X = -2 * LOG10(epsD/3.71 + 2.51 * X / RE)
37     END DO
38   Frict = 1.0/(X*X)
39   RETURN
40 END SUBROUTINE FRICTION
41 !-----------------------------------------------------------------------!
42 SUBROUTINE SIMPSON(S,matrix,TVECTOR,row)
43 !-----------------------------------------------------------------!
44 !---Subroutine that calculates the area under a function with the---!
45 !---Simpsons method. Input is two vectors and the range of those,---!
46 !---it return s, which is the area.-------------------------------!
47 !-----------------------------------------------------------------!
48   IMPLICIT NONE
49   INTEGER, INTENT(IN) :: row
50   INTEGER :: I,N
51   DOUBLE PRECISION :: H,A,B
52   DOUBLE PRECISION, INTENT(INOUT) :: S
53   DOUBLE PRECISION, INTENT(IN), DIMENSION(ROW) :: matrix,TVECTOR
54   !USE SIMPSONS ON COLUMN 1 AND K
```

```
55    N = ROW-1
56    A = TVECTOR(1)
57    B = TVECTOR(ROW)
58    H = (TVECTOR(ROW)-TVECTOR(1))/N
59    S = (MATRIX(1) + MATRIX(ROW))
60    DO I=2,N,2
61       S = S +4*MATRIX(INT(I))
62    END DO
63    DO I=3,N-1,2
64       S = S +2*MATRIX(INT(I))
65    END DO
66    S = S*H/3
67    RETURN
68
69  END SUBROUTINE SIMPSON
70  !-------------------------------------------------------------------------!
71  SUBROUTINE TWODFRICTION(FILE1,K)
72  !-------------------------------------------------------------------------!
73  !---Subroutine that has the 2D velocity as input and calculates the-!
74  !---2D unsteady components by subtracting the 1D steady component---!
75  !-------------------------------------------------------------------------!
76    USE DECLARATIONS
77    IMPLICIT NONE
78    DOUBLE PRECISION, ALLOCATABLE, DIMENSION(:,:) :: MATRIX
79    INTEGER :: M,N,I
80    INTEGER, INTENT(IN) :: K
81    DOUBLE COMPLEX :: C
82    CHARACTER(LEN=K) :: FILE1
83    M=2
84    N=2966
85    ALLOCATE(MATRIX(N,M),UT(N),RET(N),TVECTOR(N),FT(N),FS(N),FU(N),TAU(N),TAUU(N))
86    CALL read_matrix(MATRIX,N,2,FILE1,K)
87    CALL FRICTION(Re_end*mu/(rho*D))
88    ALPHA = -fricT*Re_end**2*mu**2/(2*rho*D**3)
89    WRITE (*,*) 'Pressure gradient: ',ALPHA
90    alpha = -ALPHA/rho
91    UT(1) = MATRIX(1,2)
92    CALL FRICTION(UT(1))
93    FT(1)=FRICT
94    FS(1) = FRICT
95    FU(1) = 0
96    TAU(1) = FT(1)*UT(1)**2*RHO/8
97    TAUU(1) = 0
98    DO I=2,N
99       TVECTOR(I)=MATRIX(I,1)
100      UT(I)=MATRIX(I,2)
101      RET(I)=MATRIX(I,2)*RHO*D/MU
102      CALL FRICTION(UT(I))
103      FS(I) = FRICT
104      TAU(I) = FS(I)*UT(I)**2*RHO/8
105   END DO
106   CALL WRITEVECTOR(N,tau,TVECTOR,'2DCase9Taus.dat',15)
107   DEALLOCATE(MATRIX,UT,RET,TVECTOR,FT,FS,FU,TAU,TAUU)
108 END SUBROUTINE TWODFRICTION
109 !---------------------------------------!
110 SUBROUTINE writeVector(N, Vi, Vt,filename,O)
111 !---------------------------------------!
112 !---Subroutine to print out vectors---!
113 !---------------------------------------!
114   integer, intent(in) :: N,O
115   CHARACTER (LEN=O), intent(in) :: filename
116   double precision, dimension(N+1), intent(inout) :: Vt,Vi
117   open(unit=20, file=filename, status='unknown', action='write')
118   DO i=1, N
119      write(20,*) Vt(i), Vi(i)
120   END DO
121   close(20)
122   write (*,*) filename
123   RETURN
124 END SUBROUTINE writeVector
125 !---------------------------------------!
126 SUBROUTINE read_matrix(matrix,ROW,COL,FILE1,N)
127 !---------------------------------------------!
128 !---Subroutine to read files into matrix---!
129 !---------------------------------------------!
130   IMPLICIT NONE
131   INTEGER :: i,j,n,o
132   INTEGER, INTENT(IN) :: ROW,COL
133   CHARACTER(LEN=N),INTENT(IN) :: FILE1
134   double precision,DIMENSION(ROW,COL),intent(inout) :: MATRIX
135   open(unit=10, file=file1, status='old', action='read')
136   DO i=1, ROW
137      read(10,*) (matrix(i,j), j=1,col)
138   END DO
139   close(10)
140   RETURN
141 END SUBROUTINE read_matrix
142 !-----------------------------------------------------!
143 SUBROUTINE ACCELERATION(REMATRIX,SROW,EROW,COL)
144 !-----------------------------------------------------!
```

```
145 !---Subroutine to calculate acceleration from---!
146 !---the velocity and time vector-----------------!
147 !-------------------------------------------------!
148   IMPLICIT NONE
149   INTEGER,INTENT(IN) :: SROW,EROW,COL
150   INTEGER :: I
151   DOUBLE PRECISION,INTENT(INOUT),DIMENSION(2601,COL) :: REMATRIX
152   DOUBLE PRECISION,DIMENSION(EROW-SROW+1,COL) :: ACCEL
153   DOUBLE PRECISION :: DT
154   DT = REMATRIX(SROW+1,1)-REMATRIX(SROW,1)
155   ACCEL(1,1) = REMATRIX(SROW,1)
156   ACCEL(1,2) = (0.001003/998.2)*(REMATRIX(SROW+1,2)-REMATRIX(SROW,2))/(DT)
157   WRITE(*,*) 1,SROW,ACCEL(1,1),ACCEL(1,2)
158   DO I=2,EROW-SROW
159     ACCEL(I,1) = REMATRIX(I+SROW-1,1)
160     ACCEL(I,2) = (0.001003/998.2)*(REMATRIX(I+SROW,2)-REMATRIX(I+SROW-2,2))/(2*DT)
161     WRITE(*,*) I,I+SROW-1,ACCEL(I,1),ACCEL(I,2)
162   END DO
163   ACCEL(EROW-SROW+1,1) = REMATRIX(EROW,1)
164   ACCEL(EROW-SROW+1,2) = (0.001003/998.2)*(REMATRIX(EROW,2)-REMATRIX(EROW-1,2))/(DT)
165   WRITE(*,*) EROW-SROW+1,EROW,ACCEL(EROW-SROW+1,1),ACCEL(EROW-SROW+1,2)
166   CALL WRITEVECTOR(EROW-SROW+1,ACCEL,1,ACCEL,2,'Acceleratin.txt')
167 END SUBROUTINE ACCELERATION
168 !-------------------------------------------------------------------------!
169 SUBROUTINE INTERPOLATE(INVECTOR,LENGTH,ROW,filename,L,writefilename,M)
170 !-------------------------------------------------------------------------!
171 !---SUBROUTINE TO LINEARLY INTERPOLATE TO GET VALUES AT SAME--------------!
172 !---TIMESTEP AS IN FLUENT INVECTOR IS VECTOR TO BE LINEARIZED,------------!
173 !---LENGTH IS LENGTH OF INVECTOR,LINRES IS THE LINEARIZED VECTOR,---------!
174 !---writefilename is the filename that is written out.-------------------!
175 !-------------------------------------------------------------------------!
176   USE DECLARATIONS
177   IMPLICIT NONE
178   INTEGER, INTENT(IN) :: ROW,LENGTH
179   INTEGER :: I,J,K,L,M
180   DOUBLE PRECISION, DIMENSION(LENGTH+1),INTENT(IN) :: INVECTOR
181   DOUBLE PRECISION, DIMENSION(ROW) :: LINTVECTOR,LINRES
182   DOUBLE PRECISION, DIMENSION(ROW,2) ::TEMP
183   CHARACTER (LEN=L), intent(in) :: filename
184   CHARACTER (LEN=M), intent(in) :: writefilename
185   CALL READ_MATRIX(TEMP,ROW,2,filename,L)
186   !Creating time Vector
187   DO I=1,ROW
188     LINTVECTOR(I)=TEMP(I,1)
189   END DO
190   J=1
191   LINRES(1) = INVECTOR(1)
192   DO I=2,ROW
193     DO WHILE(LINTVECTOR(I) > TVECTOR(J))
194       IF (LINTVECTOR(I) < TVECTOR(J+1)) THEN
195         EXIT
196       END IF
197       J=J+1
198       IF (J>LENGTH)THEN
199         WRITE(*,*) 'END OF FILE!',I,INVECTOR(LENGTH)
200         DO K=I,row
201           LINRES(K) = INVECTOR(LENGTH)
202         END DO
203         CALL WRITEVECTOR(row,LINRES,LINTVECTOR,writefilename,M)
204         RETURN
205       END IF
206     END DO
207     LINRES(i) = INVECTOR(J)+(INVECTOR(J+1)-INVECTOR(J))*((LINTVECTOR(I)-TVECTOR(J))/(
          TVECTOR(J+1)-TVECTOR(J)))
208   END DO
209   CALL WRITEVECTOR(ROW,LINRES,LINTVECTOR,writefilename,M)
210   RETURN
211 END SUBROUTINE INTERPOLATE
212 !-------------------------------------------------------------------------!
213 SUBROUTINE WEIGHTINGFUNCTION(TIME,WSUM,DT,NSTEPS)
214 !-------------------------------------------------------------------------!
215 !---Subroutine to calculate the weighting integral in ---!
216 !---the Vardy et al. friction model.----------------------!
217 !-------------------------------------------------------------------------!
218   USE DECLARATIONS
219   IMPLICIT NONE
220   DOUBLE PRECISION :: CSTAR,ASTAR,DT,WEIGHT,WSUM,TEST,PSI
221   INTEGER :: TIME,THETA,T,NSTEPS
222   WSUM=0
223   ALLOCATE(W(TIME+1))
224   IF (EPS > 1)THEN  !SIMPLIFIED WEIGHTING FUNCTION WITH WALL ROUGHNESS
225     DO T=1,TIME-1
226       THETA = TIME-T+1
227       PSI = 4*MU*TVECTOR(THETA)/(RHO*D**2)
228       ASTAR =0.0103*SQRT(UT(THETA)*D*RHO/MU)*(EPS/D)**0.39
229       CSTAR = 0.352*(UT(THETA)*D*RHO/MU)*(EPS/D)**0.41
230       CSTAR = 1/CSTAR
231       WEIGHT=ASTAR*EXP(-PSI/CSTAR)/(SQRT(PSI))
232       IF (T==1)THEN
233         W(T)=WEIGHT*(UT(T+1)-UT(T))/(DT)
```

```
234           WSUM = W(T)*DT  !FIRST RECTANGULAR
235         ELSE IF(T==NSTEPS)THEN
236           W(T)=WEIGHT*(UT(T)-UT(T-1))/(DT)
237           WSUM = WSUM + (ABS(W(T)-W(T-1))/2+MIN(W(T),W(T-1)))*DT
238         ELSE
239           W(T)=WEIGHT*(UT(T+1)-UT(T-1))/(2*DT)
240           WSUM = WSUM + (ABS(W(T)-W(T-1))/2+MIN(W(T),W(T-1)))*DT  !Trapeze method
241         END IF
242       END DO
243     ELSE
244       DO T=1,TIME-1
245         THETA = TIME-T+1
246         PSI = 4*MU*TVECTOR(THETA)/(RHO*D**2)
247         CSTAR = 12.86/(UT(THETA)*RHO*D/MU)**(DLOG10(15.29/((UT(THETA)*RHO*D/MU)**0.0567))
                )
248         WEIGHT=EXP(-PSI/CSTAR)/(2*SQRT(DATAN(1D0)*PSI))
249         IF (T==1)THEN
250           W(T)=WEIGHT*(UT(T+1)-UT(T))/(DT)
251           WSUM = W(T)*DT  !FIRST RECTANGULAR
252         ELSE IF(T==NSTEPS)THEN
253           W(T)=WEIGHT*(UT(T)-UT(T-1))/(DT)
254           WSUM = WSUM + (ABS(W(T)-W(T-1))/2+MIN(W(T),W(T-1)))*DT  !Trapeze method
255         ELSE
256           W(T)=WEIGHT*(UT(T+1)-UT(T-1))/(2*DT)
257           WSUM = WSUM + (ABS(W(T)-W(T-1))/2+MIN(W(T),W(T-1)))*DT  !Trapeze method
258         END IF
259       END DO
260     END IF
261     WSUM=4*MU/D*WSUM
262     DEALLOCATE(W)
263     RETURN
264   END SUBROUTINE
265   !-------------------------------------------------------------!
266   SUBROUTINE LAMINARSOLVER(NSTEPS,DT,UNSTEADY,k)
267   !-------------------------------------------------------------!
268   !---Laminar solver, both for quasi-steady friction,---!
269   !---and Daily et al friction model--------------------!
270   !-------------------------------------------------------------!
271     USE DECLARATIONS
272     IMPLICIT NONE
273     DOUBLE PRECISION::DT,k
274     INTEGER::NSTEPS,I
275     LOGICAL::UNSTEADY
276     DEALLOCATE(UT,RET,FT,TAU,TVECTOR,FU,FS,TAUU)
277     ALLOCATE(UT(NSTEPS),RET(NSTEPS),FT(NSTEPS),FS(NSTEPS),FU(NSTEPS),TAUU(NSTEPS),TAU(
          NSTEPS),TVECTOR(NSTEPS))
278     !Calculating pressure gradient:
279     FRICT = 64/RE_END
280     ALPHA = -frict*Re_end**2*mu**2/(2*rho*D**3)
281     WRITE(*,*) 'Pressure gradient: ',ALPHA
282     alpha = -ALPHA/rho
283     BETA = 32*MU/(RHO*D**2)
284     !Creating time Vector
285     DO I=1,NSTEPS
286       tVector(I) = (I-1)*DT
287     END DO
288     UT(1) = RE_START*MU/RHO/D
289     FT(1) = 64/RE_START
290     TAU(1) = FRICT*RHO*UT(1)**2/8
291     RET(1)=RE_START
292     DO I=2,NSTEPS
293       UT(I) = ALPHA/BETA+(UT(1)-ALPHA/BETA)*EXP(-BETA*TVECTOR(I))
294       RET(I)=UT(I)*RHO*D/MU
295       FT(I)=64/RET(I)
296       TAU = FT(I)*RHO*UT(I)**2/8
297       IF(UNSTEADY)THEN
298         FRICT = 64/RET(I)+2*k/UT(I)**2*D*(UT(I)-UT(I-1))/(DT)
299         FT(I) = FRICT
300         ALPHA = 64*Re_end*mu**2/(2*rho*D**3)/RHO-K*(UT(I)-UT(I-1))/(DT)
301         WRITE(*,*) RET(I),frict,K*(UT(I)-UT(I-1))/(DT)
302       END IF
303     END DO
304     RETURN
305   END SUBROUTINE LAMINARSOLVER
306   !-------------------------------------------------------------------!
307   SUBROUTINE QUASI_STEADY_FRICTION_SOLVER(NSTEPS)
308   !-------------------------------------------------------------------!
309   !---SUBROUTINE TO IMPLICITLY SOLVE THE 1D ---------------------!
310   !---MODEL USING QUASI-STEADY FRICTION. THE TIME VECTOR, T,----!
311   !---MUST BE INITIALIZED BEFORE CALLING THIS ROUTINE-----------!
312   !---IN ADDITION, THE VECTORS UT, TAU, RET, AND .--------------!
313   !---FS MUST BE ALLOCATED BEFOREHAND---------------------------!
314   !---THE VECTORS UT,TAU,RET, AND FS ARE UPDATED----------------!
315   !-------------------------------------------------------------------!
316     USE DECLARATIONS
317     IMPLICIT NONE
318     INTEGER :: I,NSTEPS
319     DOUBLE COMPLEX :: C
320     DOUBLE PRECISION :: UOLD
321     DO I=2,NSTEPS
```

```
322     Ut(I) = Ut(I-1)
323     UOLD = Ut(I)+1
324     !Loop that implicitly solves Ut(I)
325     DO WHILE (ABS(Ut(I)-UOLD) > tol)
326       UOLD = Ut(I)
327       !Function that returns the Darcy friction factor
328       CALL FRICTION(Ut(I))
329       FS(I)=FRICT
330       BETA = FS(I)/2/D
331       !Integration constant
332       C = 1/SQRT(alpha*beta)*(ATANH(DCMPLX(Ut(1)*SQRT(beta/alpha),0)))
333       Ut(I) = SQRT(alpha/beta)*ABS(tanh(DCMPLX((sqrt(alpha*beta)*tVector(I)+c*SQRT(alpha*
              beta)))))
334     END DO
335     TAU(I) = (FS(I) * rho *UT(I)**2)/8
336     RET(I) = UT(I)*RHO*D/MU
337   END DO
338   END SUBROUTINE QUASI STEADY FRICTION SOLVER
339   !-------------------------------------------------------------!
340   SUBROUTINE DAILY ET AL(NSTEPS,DT)
341   !-------------------------------------------------------------!
342   !---Finds the unsteady component of the fricion factor---!
343   !---and updates the velocity according to Daily et al.---!
344   !--- model with Brunone unsteady friction coeff----------!
345   !-------------------------------------------------------------!
346     USE DECLARATIONS
347     IMPLICIT NONE
348     INTEGER :: I,L,nsteps,J
349     DOUBLE PRECISION :: UOLD,DT,k,ASTAR,CSTAR,M,TEST
350     DOUBLE COMPLEX :: C
351     DOUBLE PRECISION, DIMENSION(NSTEPS) :: TEMP
352     !SETTING INITIAL VALUES
353     M=1
354     UT2(1)=UT(1)
355     DO J=1,3
356       DO I=2,NSTEPS-1
357         CALL FRICTION(Ut(I))
358         FS(I)=FRICT
359         IF(EPS>1)THEN
360           ASTAR = 0.0103*SQRT(UT(I)*D*RHO/MU)*(EPS/D)**0.39
361           CSTAR = 0.352*UT(I)*D*RHO/MU*(EPS/D)**0.41
362           CSTAR = 1/CSTAR
363           K = 4*ASTAR*DSQRT(DATAN(1D0)*CSTAR)
364         ELSE
365           CSTAR = 12.86/(UT(I)*RHO*D/MU)**(LOG10(15.29/((UT(I)*RHO*D/MU)**0.0567)))
366           k = M*2*SQRT(CSTAR)
367         END IF
368         TAUU(I) = K*RHO*D/4*(Ut(I+1)-Ut(I-1))/(TVECTOR(I+1)-TVECTOR(I-1))
369         Fu(I) = 8*TAUU(I)/(RHO*UT(I)**2)
370         BETA = (FS(I) + FU(I))/2/D
371         IF (BETA<0)THEN
372           WRITE(*,*) 'Negative friction 1'
373           stop
374         END IF
375         C = 1/sqrt(alpha*beta)*(ATANH(DCMPLX(Ut(1)*SQRT(beta/alpha),0)))
376         UT2(I) = sqrt(alpha/beta)*ABS(tanh(DCMPLX((sqrt(alpha*beta)*tVector(I)+c*SQRT(
              alpha*beta)))))
377         FT(I) = FU(I)+FS(I)
378         RET(I)=UT2(I)*RHO*D/MU
379         TAUS(I)=(FS(I)*RHO*UT2(I)**2)/8
380         tau(I) = (FT(I) * rho *UT(I)**2)/8
381       END DO
382       IF(EPS>1)THEN
383         ASTAR = 0.0103*SQRT(UT(NSTEPS)*D*RHO/MU)*(EPS/D)**0.39
384         CSTAR = 0.352*UT(NSTEPS)*D*RHO/MU*(EPS/D)**0.41
385         CSTAR = 1/CSTAR
386         K = 4*ASTAR*DSQRT(DATAN(1D0)*CSTAR)
387       ELSE
388         CSTAR = 12.86/(UT(NSTEPS)*RHO*D/MU)**(LOG10(15.29/((UT(NSTEPS)*RHO*D/MU)**0.0567)
              ))
389         k = M*2*SQRT(CSTAR)
390       END IF
391       CALL FRICTION(Ut(NSTEPS))
392       FS(NSTEPS)=FRICT
393       TAUU(NSTEPS) = (TAUU(NSTEPS-1)-TAUU(NSTEPS-2))*2+TAUU(NSTEPS-2)
394       Fu(NSTEPS) = 8*TAUU(NSTEPS)/(RHO*UT(NSTEPS)**2)
395       BETA = (FS(NSTEPS) + FU(NSTEPS))/2/D
396       IF (BETA<0)THEN
397         WRITE(*,*) 'NEGATIVE FRICTION!',I,UT(NSTEPS)
398         STOP
399       END IF
400       C = 1/sqrt(alpha*beta)*(ATANH(DCMPLX(Ut(1)*SQRT(beta/alpha),0)))
401       UT2(I) = sqrt(alpha/beta)*ABS(tanh(DCMPLX((sqrt(alpha*beta)*tVector(NSTEPS)+c*SQRT(
              alpha*beta)))))
402       FT(NSTEPS)=FS(NSTEPS)+FU(NSTEPS)
403       RET(NSTEPS)=UT2(NSTEPS)*RHO*D/MU
404       TAUS(I)=(FS(NSTEPS)*RHO*UT2(NSTEPS)**2)/8
405       tau(I) = (FT(NSTEPS) * rho *UT2(NSTEPS)**2)/8
406       TEMP = ABS(UT-UT2)
407       L= (MAXLOC(TEMP,NSTEPS))
```

```
408       WRITE(*,*) 'Iter',J,'Highest diff:',TEMP(L),L,'Avg diff: ',SUM(TEMP)/(NSTEPS)
409       UT=UT2
410     END DO
411     RETURN
412   END SUBROUTINE DAILY_ET_AL
413   !-------------------------------------------------------------!
414   SUBROUTINE VARDY_ET_AL(NSTEPS,DT)
415   !-------------------------------------------------------------!
416   !---Finds the unsteady component of the fricion----------!
417   !---factor and updates the velocity----------------------!
418   !---according to Vardy et al. weighting friction model---!
419   !-------------------------------------------------------------!
420     USE DECLARATIONS
421     IMPLICIT NONE
422     INTEGER :: I,L,nsteps,J
423     DOUBLE PRECISION :: UOLD,DT,CSTAR,WSUM,M
424     DOUBLE COMPLEX :: C
425     DOUBLE PRECISION, DIMENSION(NSTEPS):: TEMP
426     !SETTING INITIAL VALUES
427     UT2(1)=UT(1)
428     M=1
429     TEMP=1
430     DO WHILE(SUM(TEMP)/NSTEPS>TOL*10000)
431       DO I=2,NSTEPS-1
432         CALL FRICTION(Ut(I))
433         FS(I)=FRICT
434         CALL WEIGHTINGFUNCTION(I,WSUM,TVECTOR(I)-TVECTOR(I-1),NSTEPS)
435         WSUM=WSUM*M
436         TAUU(I)=WSUM
437         FU(I)=WSUM*8/RHO/UT(I)**2
438         BETA = (FS(I) + FU(I))/2/D
439         IF (BETA<0)THEN
440           WRITE(*,*) 'NEGATIVE FRICTION!'
441           STOP
442         END IF
443         C = 1/sqrt(alpha*beta)*(ATANH(DCMPLX(Ut(1)*DSQRT(beta/alpha),0)))
444         UT2(I) = sqrt(alpha/beta)*ABS(tanh(DCMPLX((dsqrt(alpha*beta)*tVector(I)+c*SQRT(
                alpha*beta)))))
445         IF(mod(I,(1000))==0)THEN
446           write(*,*) I,FU(I),FS(i),UT2(I)-UT(I)
447         END IF
448         Ft(I) = FS(I)+FU(I)
449         Ret(I) = rho*Ut2(I)*D/mu
450         tau(I) = (FT(I) * rho *UT2(I)**2)/8
451       END DO
452       CALL FRICTION(Ut(NSTEPS))
453       FS(NSTEPS)=FRICT
454       CALL WEIGHTINGFUNCTION(NSTEPS,WSUM,TVECTOR(NSTEPS)-TVECTOR(NSTEPS-1),NSTEPS)
455       WSUM = M*WSUM
456       TAUU(NSTEPS)=WSUM
457       FU(NSTEPS)=WSUM*8/RHO/UT(NSTEPS)**2
458       BETA = (FS(NSTEPS)+FU(NSTEPS))/2/D
459       C = 1/sqrt(alpha*beta)*(ATANH(DCMPLX(Ut(1)*SQRT(beta/alpha),0)))
460       UT2(NSTEPS) = sqrt(alpha/beta)*ABS(tanh(DCMPLX((sqrt(alpha*beta)*tVector(NSTEPS)+c*
              SQRT(alpha*beta)))))
461       WRITE(*,*) NSTEPS,UT(NSTEPS),FU(NSTEPS)
462       Ft(NSTEPS) = FS(NSTEPS)+FU(NSTEPS)
463       Ret(NSTEPS) = rho*Ut2(NSTEPS)*D/mu
464       tau(NSTEPS) = (FT(NSTEPS) * rho *UT2(NSTEPS)**2)/8
465       TEMP = ABS(UT-UT2)
466       L= (MAXLOC(TEMP,NSTEPS))
467       WRITE(*,*) 'Max diff at',L,'with',TEMP(L),'average',SUM(TEMP)/(NSTEPS)
468       UT=UT2
469     END DO
470     RETURN
471   END SUBROUTINE VARDY_ET_AL
472   !-------------------------------------------------!
473   SUBROUTINE QUASI_STEADY_1D_TURB_MODEL(FILE1_NAME,LENGTH_OF_NAME,LENGTH,NSTEPS,DT)
474   !-------------------------------------------------!
475   !---Solves the 1D turbulent model with the---!
476   !---quasi-steady friction, implicitly--------!
477   !-------------------------------------------------!
478
479     USE DECLARATIONS
480     IMPLICIT NONE
481
482     INTEGER :: I
483     INTEGER, INTENT(IN) :: NSTEPS,LENGTH,LENGTH_OF_NAME
484     DOUBLE COMPLEX :: C
485     DOUBLE PRECISION :: DT
486     CHARACTER(LEN=LENGTH_OF_NAME) :: FILE1_NAME
487     ALLOCATE(UT(NSTEPS),RET(NSTEPS),TVECTOR(NSTEPS),FS(NSTEPS),TAU(NSTEPS))
488     !CREATING TIME VECTOR
489     DO I=1,NSTEPS
490       TVECTOR(I)=(I-1)*DT
491     END DO
492     !INITIALIZING VECTORS
493     CALL FRICTION(Re_end*mu/(rho*D))
494     ALPHA = -fricT*Re_end**2*mu**2/(2*rho*D**3)
495     alpha = -ALPHA/rho
```

```
496     UT(1) = RE_START*MU/D/RHO
497     RET(1)=RE_START
498     CALL FRICTION(UT(1))
499     FS(1) = FRICT
500     TAU(1) = FS(1)*UT(1)**2*RHO/8
501     !CALLING SOLVER
502     CALL QUASI_STEADY_FRICTION_SOLVER(NSTEPS)
503     !WRITING VECTORS TO FILE
504     CALL INTERPOLATE(UT,NSTEPS,LENGTH,FILE1_NAME,LENGTH_OF_NAME,'1DCaseXQSVel.txt',16)
505     CALL INTERPOLATE(RET,NSTEPS,LENGTH,FILE1_NAME,LENGTH_OF_NAME,'1DCaseXQSRey.txt',16)
506     CALL INTERPOLATE(FS,NSTEPS,LENGTH,FILE1_NAME,LENGTH_OF_NAME,'1DCaseXQS_Ft.txt',16)
507     CALL INTERPOLATE(TAU,NSTEPS,LENGTH,FILE1_NAME,LENGTH_OF_NAME,'1DCaseXQSTau.txt',16)
508     !DEALLOCATING ALLOCATED VECTORS
509     DEALLOCATE(UT,REt,FS,TAU,TVECTOR)
510   END SUBROUTINE QUASI_STEADY_1D_TURB_MODEL
511   !-----------------------------------------------!
512   SUBROUTINE DAILY_ET_AL_1D_TURB_MODEL(FILE1_NAME,LENGTH_OF_NAME,LENGTH,NSTEPS,DT)
513   !-----------------------------------------------!
514   !---Solves the 1D turbulent model with the---!
515   !---Daily et al. friction, implicitly--------!
516   !-----------------------------------------------!
517     USE DECLARATIONS
518     IMPLICIT NONE
519     INTEGER :: I
520     INTEGER, INTENT(IN) :: NSTEPS,LENGTH,LENGTH_OF_NAME
521     DOUBLE PRECISION :: DT
522     CHARACTER(LEN=LENGTH_OF_NAME) :: FILE1_NAME
523
524     ALLOCATE(Ut(NSTEPS),Ret(NSTEPS),ft(NSTEPS),tau(NSTEPS),tVector(NSTEPS),Fu(NSTEPS))
525     ALLOCATE(FS(NSTEPS),TAUU(NSTEPS),TAUS(NSTEPS),UT2(NSTEPS))
526     !CREATING TIME VECTOR
527     DO I=1,NSTEPS
528       TVECTOR(I)=(I-1)*DT
529     END DO
530     !INITIALIZING VECTORS
531     CALL FRICTION(Re_end*mu/(rho*D))
532     ALPHA = -fricT*Re_end**2*mu**2/(2*rho*D**3)
533     alpha = -ALPHA/rho
534     UT(1) = RE_START*MU/D/RHO
535     RET(1)=RE_START
536     CALL FRICTION(UT(1))
537     FS(1) = FRICT
538     FU(1)=0
539     FT(1)=FS(1)
540     TAU(1) = FS(1)*UT(1)**2*RHO/8
541     TAUS(1)=TAU(1)
542     TAUU(1)=0
543     !CALLING QUASI-STEADY SOLVER
544     CALL QUASI_STEADY_FRICTION_SOLVER(NSTEPS)
545     !CALLING DAILY ET AL. FRICTION MODEL
546     CALL DAILY_ET_AL(NSTEPS,DT)
547     !WRITING OUT VECTORS TO TEXT FILES. DATA IS INTERPOLATED TO FIT 2D TIMEVECTOR
548     CALL INTERPOLATE(UT,NSTEPS,LENGTH,FILE1_NAME,LENGTH_OF_NAME,'1DCaseXUK_Ut.txt',16)
549     CALL INTERPOLATE(RET,NSTEPS,LENGTH,FILE1_NAME,LENGTH_OF_NAME,'1DCaseXUK_Re.txt',16)
550     CALL INTERPOLATE(FT,NSTEPS,LENGTH,FILE1_NAME,LENGTH_OF_NAME,'1DCaseXUK_Ft.txt',16)
551     CALL INTERPOLATE(TAU,NSTEPS,LENGTH,FILE1_NAME,LENGTH_OF_NAME,'1DCaseXUK_Tau.txt',17)
552     CALL INTERPOLATE(TAUU,NSTEPS,LENGTH,FILE1_NAME,LENGTH_OF_NAME,'1DCaseXUK_TauU.txt'
            ,18)
553     CALL INTERPOLATE(FU,NSTEPS,LENGTH,FILE1_NAME,LENGTH_OF_NAME,'1DCaseXUK_Fu.txt',16)
554     CALL INTERPOLATE(FS,NSTEPS,LENGTH,FILE1_NAME,LENGTH_OF_NAME,'1DCaseXUK_Fs.txt',16)
555     DEALLOCATE(UT,RET,FT,TAU,TVECTOR,FU,FS,TAUU,TAUS,UT2)
556
557   END SUBROUTINE DAILY_ET_AL_1D_TURB_MODEL
558   !-----------------------------------------------------------!
559   SUBROUTINE VARDY_ET_AL_1D_TURB_MODEL(FILE1_NAME,LENGTH_OF_NAME,LENGTH,NSTEPS,DT)
560   !-----------------------------------------------------------!
561   !---Solves the 1D turbulent model with the Vardy et al.---!
562   !---friction, implicitly---------------------------------!
563   !-----------------------------------------------------------!
564     USE DECLARATIONS
565     IMPLICIT NONE
566     INTEGER :: I
567     INTEGER, INTENT(IN) :: NSTEPS,LENGTH,LENGTH_OF_NAME
568     DOUBLE PRECISION :: DT
569     CHARACTER(LEN=LENGTH_OF_NAME) :: FILE1_NAME
570
571     ALLOCATE(Ut(NSTEPS),Ret(NSTEPS),ft(NSTEPS),tau(NSTEPS),tVector(NSTEPS),Fu(NSTEPS))
572     ALLOCATE(FS(NSTEPS),TAUU(NSTEPS),TAUS(NSTEPS),UT2(NSTEPS))
573     !CREATING TIME VECTOR
574     DO I=1,NSTEPS
575       TVECTOR(I)=(I-1)*DT
576     END DO
577     !INITIALIZING VECTORS
578     CALL FRICTION(Re_end*mu/(rho*D))
579     ALPHA = -fricT*Re_end**2*mu**2/(2*rho*D**3)
580     alpha = -ALPHA/rho
581     UT(1) = RE_START*MU/D/RHO
582     RET(1)=RE_START
583     CALL FRICTION(UT(1))
584     FS(1) = FRICT
```

```
585     FU(1)=0
586     FT(1)=FS(1)
587     TAU(1) = FS(1)*UT(1)**2*RHO/8
588     TAUS(1)=TAU(1)
589     TAUU(1)=0
590     !CALLING QUASI-STEADY SOLVER
591     CALL QUASI_STEADY_FRICTION_SOLVER(NSTEPS)
592     !CALLING DAILY ET AL. FRICTION MODEL
593     CALL VARDY_ET_AL(NSTEPS,DT)
594     CALL INTERPOLATE(UT,NSTEPS,LENGTH,FILE1_NAME,LENGTH_OF_NAME,'1DCaseXUW_Ut.txt',16)
595     CALL INTERPOLATE(RET,NSTEPS,LENGTH,FILE1_NAME,LENGTH_OF_NAME,'1DCaseXUW_Re.txt',16)
596     CALL INTERPOLATE(FT,NSTEPS,LENGTH,FILE1_NAME,LENGTH_OF_NAME,'1DCaseXUW_Ft.txt',16)
597     CALL INTERPOLATE(TAU,NSTEPS,LENGTH,FILE1_NAME,LENGTH_OF_NAME,'1DCaseXUW_Tau.txt',17)
598     CALL INTERPOLATE(TAUU,NSTEPS,LENGTH,FILE1_NAME,LENGTH_OF_NAME,'1DCaseXUW_TauU.txt'
            ,18)
599     CALL INTERPOLATE(FU,NSTEPS,LENGTH,FILE1_NAME,LENGTH_OF_NAME,'1DCaseXUW_Fu.txt',16)
600     CALL INTERPOLATE(FS,NSTEPS,LENGTH,FILE1_NAME,LENGTH_OF_NAME,'1DCaseXUW_Fs.txt',16)
601     DEALLOCATE(UT,RET,FT,TAU,TVECTOR,FU,FS,TAUU,TAUS,UT2)
602
603 END SUBROUTINE VARDY_ET_AL_1D_TURB_MODEL
604 !-----------------------------------------------------------------------!
605 END MODULE SUB
606 !-----------------------------------------------------------------------!
607 PROGRAM ONEDIMTURBFLOW
608 !-----------------------------------------------------------------------!
609 !---Input description of the transient case, the name of --------!
610 !---the 2D velocity file, and the length of said file.----------!
611 !-----------------------------------------------------------------------!
612     USE DECLARATIONS
613     USE SUB
614     IMPLICIT NONE
615     INTEGER :: NSTEPS,LENGTH,LENNAME
616     DOUBLE PRECISION :: DT,K
617     CHARACTER(LEN=30) :: FNAME
618     Re_start = 1e7
619     Re_end = 2e4
620     !geometry of pipe and fluid properties
621     D = 1.0D0
622     eps = 1*2e-6
623     rho = 998.2D0
624     mu = 0.001003D0
625     !friction calculation tolerance
626     tol = 1.0E-10
627     K=0
628     FNAME='VelocityCaseX.dat' !NAME OF FLUENT DAT FILE TO EXTRACT TIME VECTOR FROM
629     LENGTH = 10001 !LENGTH OF FLUENT DAT FILE
630     LENNAME = LEN_TRIM(FNAME)
631     !Finding the unsteady component of wall shear stress in the 2D simulation
632     CALL TWODFRICTION(FNAME,LENNAME)
633     IF ((RE_START >= 2300).AND.(RE_END >= 2300)) THEN
634        NSTEPS = 44001
635        DT = 0.5
636        CALL QUASI_STEADY_1D_TURB_MODEL(FNAME,LENNAME,LENGTH,NSTEPS,DT)
637        CALL DAILY_ET_AL_1D_TURB_MODEL(FNAME,LENNAME,LENGTH,NSTEPS,DT)
638        NSTEPS = 11001
639        DT= 2E0
640        CALL VARDY_ET_AL_1D_TURB_MODEL(FNAME,LENNAME,LENGTH,NSTEPS,DT)
641     ELSE IF ((RE_START < 2300).AND.(RE_END<2300)) THEN
642        NSTEPS = 5000
643        DT = 0.000001
644        unsteady = .TRUE.
645        CALL LAMINARSOLVER(NSTEPS,DT,UNSTEADY,K)
646        CALL WRITEVECTOR(NSTEPS,UT,TVECTOR,'1DLAM1000VeU.txt',16)
647        CALL WRITEVECTOR(NSTEPS,RET,TVECTOR,'1DLAM1000ReU.txt',16)
648        CALL WRITEVECTOR(NSTEPS,FT,TVECTOR,'1DLAM1000DaU.txt',16)
649        CALL WRITEVECTOR(NSTEPS,TAU,TVECTOR,'1DLAM1000Tau.txt',16)
650     ELSE
651        WRITE(*,*) 'Warning, both start and end Reynolds number must be within same regime,
               either laminar or turbulent!'
652     END IF
653 END PROGRAM ONEDIMTURBFLOW
```